UNIVERSITY OF CAPE TOWN
IYUNIVESITHI YASEKAPA • UNIVERSITEIT VAN KAAPSTAD

Micromechanical modelling of advanced hierarchical composites

by

Author:
Emma Griffiths

Supervisor:
Prof. B.D. Reddy

Co-Supervisor:
Prof. Swantje Bargmann

Thesis presented for the Degree of
Doctor of Philosophy in Mechanical Engineering
University of Cape Town

June 2020

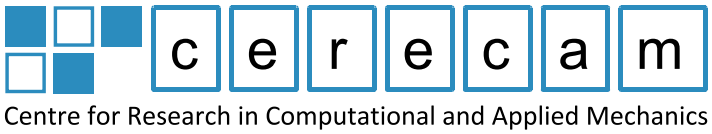

Declaration

I, **Emma Griffiths**, hereby declare that the work on which this thesis is based is my original work (except where acknowledgements indicate otherwise) and that neither the whole work nor any part of it has been, is being, or is to be submitted for another degree in this or any other university. I authorise the University to reproduce for the purpose of research either the whole or any portion of the contents in any manner whatsoever.

Signature: Signed by candidate Date: 13 December 2019

Abstract

Nanoporous metals are uniquely interesting materials. Their high ductility and impressive strength in compression make them a favourable candidate for use in structural applications. However, these materials under-perform when tested in tension. This issue may be addressed by impregnating the nanoporous metal with a polymer. In this work the behaviour of a polymer impregnated nanoporous gold (NPG) composite is explored using the finite element method in three different scenarios: linear elasticity, fracture and electrically stimulated actuation. Using representative volume elements (RVEs), previously unexplored relationships between the macroscopic material response and its microstructure as well as interesting mechanisms and deformation strategies are explored.

Firstly the homogenization and micromechanical response under compression of a gold/epoxy nanocomposite is investigated. Investigation into the stress-strain response within the material reveals a complex interaction between the constituents resulting in both compressive and tensile strains. With specific focus on the loading modes of the individual ligaments, significant axial and bending loading as well as an unexpectedly large amount of shear stress is seen.

Following this the improved ductility and resistance to fracture of a gold/polymer nanocomposite compared to the pure NPG material is revealed using computational compact-tension tests. It is observed that the polymer stabilizes the gold thus preventing ductile fracture. Several toughening mechanisms are also revealed. Previously unexplored effects of increasing the volume fraction on the ductility and strength of the composite are also explored.

The functionality of the gold/polymer nanocomposite as an actuator material is then investigated. A coupled chemo-electro-mechanical material model is adopted to model the electrically stimulated deformation. This is carried out in Abaqus using a novel staggered explicit-implicit solution scheme. Simulation of several RVEs with different gold volume fractions show that while the gold provides strength and support, increasing its volume fraction hinders both the ion transport speed and the total deformation of the nanocomposite. A complex interaction between the stress response and the gold volume fraction is also observed.

Acknowledgements

This thesis was most certainly not done in isolation and could not have been completed without the guidance and assistance from several people to whom I would like to extend my thanks:

- My supervisor, Prof Daya Reddy for his guidance and support throughout this post-graduate journey.
- My co-supervisor Prof Swantje Bargmann at the University of Wuppertal for providing a significant amount of support and encouragement and always pushing me to be better.
- Jana Wilmers and Celal Soyarslan at the University of Wuppertal for taking time out to help and assist me in my research.
- The CERECAM members with specific reference to Nkosilathi Vundla, Ritesh Rama, Daniel van Huyssteen and Heidi Burger for their friendship and making my time in CERECAM one of my best experiences to date.
- Natalie Bent for her exceptional administration help and friendship.
- My family for their unwavering belief in my abilities and endless supply of support.
- The National Research Fund for making this degree financially possible.
- The German Research Foundation for funding my research trips to Germany.

To everyone else that has stood by me during this time, loving and supporting me in so many ways I am eternally grateful. All glory be to God for giving me all I needed to achieve this.
Soli Deo Gloria.

Contents

List of Figures

List of Tables

1

Introduction

1.1 Hierarchical materials

Hierarchical materials are those that have recognizable and unique topological features on more than one length scale [1]. Such materials can be both synthetic and naturally occurring. Naturally occurring hierarchical materials include muscle, wood and bone (Figure 1.1).

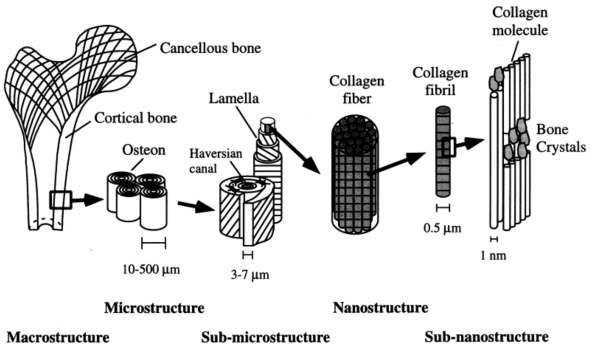

Fig. 1.1: An example of the hierarchical structure of bone [2] [1].

Hierarchical materials show a dependence of their macroscopic material properties (for example strength, stiffness, density) on their features at smaller length scales (microscale), thus creating a structure-property relationship across length scales. Within naturally occurring hierarchical composites such as bone these relationships are exploited through functional adaptation and the microstructure is altered in order to produce the best possible macroscale properties. In bone, for example, in order to accommodate large stresses the structure of the mineral particles (at the nanoscale) or arrangement of the collagen fibres (at the microscale) can change in order to alter the bone density and hence strength (a macroscale property) [3].

[1] Reprinted from Medical Engineering & Physics , 20 /2, J.-Y. Rho, L. Kuhn-Spearing, P. Zioupos, Mechanical properties and the hierarchical structure of bone, Copyright (1998), with permission from Elsevier.

In the design of engineering structures using classical engineering materials, the materials are either selected and a design altered to accommodate for its properties, or a design is created and a suitable material selected based on a handful of available materials with pre-defined properties. Synthetic hierarchical materials, however, offer the possibility of creating materials to suit specific designs or applications. That is, once a design has been developed a material could be tailored on the microscale to produce the required macroscale properties. In order to achieve this, an understanding of the relationships between the different scales and the resultant macroscopic properties is needed. It is thus important to investigate how the microstructure affects the macroscopic behaviour of a hierarchical material.

A common category of man-made hierarchical materials are composites. Composite materials are considered to be hierarchical materials with an order of hierarchy of at least two, where the order of hierarchy is defined by the number of length scales that exists within a material [1]. Composite materials combine two or more materials, the goal being to create a new material with a combination of their properties or possibly even superior properties [4]. In most composites there is a matrix phase and a reinforcement phase. The matrix is generally more compliant with the reinforcement providing strength and stiffness. The volume fraction, distribution, morphology and topology of each phase will influence the properties of the resulting composite. In this work we look at these relationships for a composite comprising a nanoporous metal and an impregnated polymer as the reinforcement and matrix material respectively. A review of the work done on nanoporous metals and their response to compressive and tensile loading conditions is given. A review of the work done on a polymer-impregnated nanoporous gold nanocomposite, that will be the focus of this work, is then given.

1.2 Nanoporous metals

Nanoporous metals are a relatively new and promising type of hierarchical material highlighted in Figure 1.2. These are porous foams that comprise a three-dimensional network of ligaments with diameters on the nanoscale.

The ligaments are highly interconnected and form a completely continuous network with over 10^{15} ligaments per mm^3. Nanoporous metals are created from a dealloying process in which the less noble constituent of an alloy is removed by selective corrosion [7]. This removal then leads to the spontaneous formation of a three-dimensional

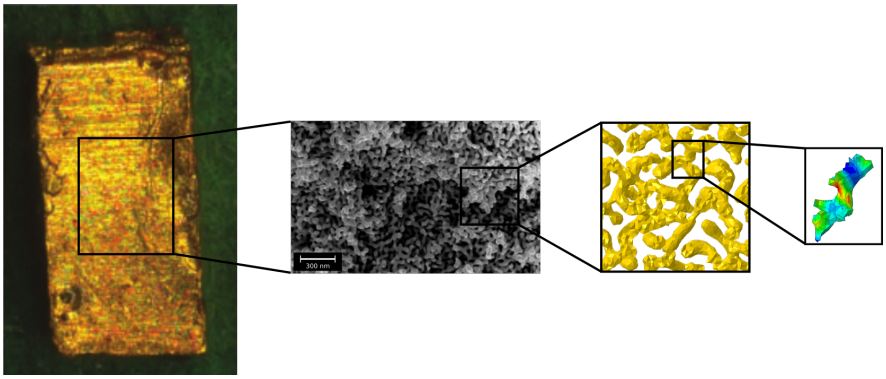

Fig. 1.2: Hierarchical structure of nanoporous metals. Figure adapted from [5][2]and [6] [3]

bicontinuous material. The volume fraction of metal is approximately equal to the metal fraction within the original metal alloy. Nanoporous metals can have metal volume fractions between 20 and 50%. The ligament diameters can be tailored from 3 nm to several microns by applying a thermal coarsening treatment during this process.

The presence of these ligaments (and other nano-objects such as nanoparticles, wires, pillars) have been shown to improve the macroscopic strength of a material well beyond that predicted by the classical rule of mixtures [8]. This has resulted in properties of these materials often being very different, and possibly more appealing, to those of their bulk counterparts [9]. The large surface area-to-volume ratio that develops in nanoporous metals motivates its use as a catalyst or electrode in batteries or capacitors [10, 11]. Its mechanical properties have also suggested its use in structural and actuation applications [12,13]. Nanoporous metals have been created from various metals such as silver [14], platinum [15], copper [16], nickel [17,18], palladium [19,20], titanium [21], aluminium [22] and gold [23].

1.2.1 Nanoporous gold

Much of the research focus has been specifically on nanoporous gold (NPG) as its manufacturing process can be easily controlled and high quality samples can be produced. This work will focus exclusively on nanoporous gold.

Nanoporous gold in compression

Nanoporous gold has two unique material properties that have motivated the attention given it in experimental and numerical research. Firstly, it shows an exceptionally high

[3] Reproduced with permission from John Wiley & Sons, Inc
[3] Image courtesy of Nadiia Mameka at Helmholtz-Zentrum Geesthacht

compressibility, up to a 200% strain without undergoing any macroscopic fracture [24]. Two mechanisms have been suggested to facilitate this: densification, which allows for a large amount of work hardening, and the ductility within the microstructure (that is, the ligaments) [24,25]. Secondly, nanoporous gold has a very high strength-to-porosity ratio [26]. It has been manufactured to have yield strengths and hardness values even greater than that of bulk gold with yield strengths of up to 240 MPa (bulk gold has a yield strength of 200 MPa).

Nanoporous gold in tension

The exceptional properties of nanoporous gold are, however, limited to its compressive response. There exists an extreme tension/compression asymmetry in nanoporous gold as under tension it exhibits an extremely brittle response. Experimental uniaxial tensile tests produce small fracture strains of 0.22-0.7% and small maximum loading stresses of between 9-25 MPa at ligament diameters above 20 nm [27–31]. Upon inspection of the fracture surfaces, significant elongation of the individual ligaments has been noted [23, 32–35]. Three-point bending tests have similarly shown very low fracture stresses of 5-12 MPa [36, 37]. At the lower end of the range of ligament diameters in nanoporous gold (below 20 nm), the strength and elongation show a substantial increase. Xia et al. [38] recorded much larger stresses and strains of up to 97.9 MPa and 7.3% respectively for uniaxial tensile tests on samples with ligament diameters between 10 and 11 nm. Although ultimate strengths of up to 562 MPa and fracture strains up to 6% have been recorded for NPG samples using molecular dynamic simulations on 5 nm ligament sized samples [39–41], these significantly larger values have not been confirmed experimentally.

Structure-property relations within nanoporous gold

Strength and hardness

There exists a relationship of increasing strength of the material with an increase in volume fraction of metal [39–41]. However, a unique relationship exists within nanoporous metals, in that an increase in strength and hardness also occurs with a decrease in ligament diameter (Figure 1.3) [7,25,26,41–51]. This ‘smaller is stronger’ relationship arises as the material experiences dislocation starvation since large dislocation sources cannot be accommodated by the small ligaments. Thus, large stresses need to be applied in order to activate dislocation sources and cause yielding [7,26,42]. This also results in high hardness values in these material. At sufficiently small ligament diameters, nanoporous

metals have shown yield strengths greater than that of its corresponding bulk material. The change in ligament connectivity at different volume fractions and its influence on the load bearing nature of ligaments has also been suggested as a contributory factor to this relationship [46, 47].

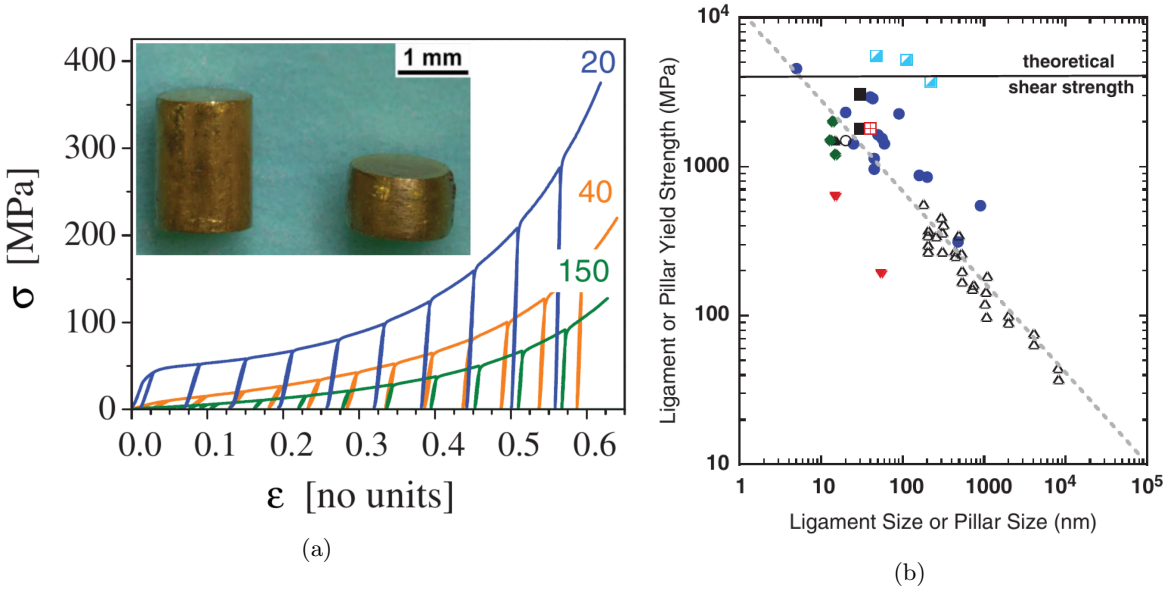

(a) (b)

Fig. 1.3: Results from compression tests of nanoporous gold showing the (a) increase in strength and (b) increase in yield strength with a decrease in ligament size. Reproduced from [46] and [24][4]respectively.

Young's modulus

The Young's modulus of nanoporous gold has been shown to vary greatly with the metal volume fraction and the average ligament size [47, 52, 53]. At larger metal volume fractions the material is more stiff. An increase in Young's modulus with a decrease in ligament diameters has also been noted, although this is less consistently seen in the literature [46, 53–55]. Various mechanisms have been suggested to account for the dependence of Young's modulus on these material properties. Mathur and Erlebacher [54] found a strong dependence of the Young's modulus on the ligament diameters when performing compression tests on specimens with ligament sizes of 3, 6, 12, 20 and 40 nm at a constant volume fraction. The Young's modulus at 3 nm was 6 times stiffer than that at 40 nm. They suggested as an explanation that, at constant volume fractions, characteristically smaller ligament-sized materials have more ligaments compared to a material with thicker ligament size requirements. The former would thus have a larger

[4] Reproduced with permission.

moment of inertia which would give the material a higher bending stiffness, and which thus would result in a stiffer macroscopic material response. Mameka et al. [46] investigated the influence of the network connectivity on the elastic modulus. This property is affected by both the volume fraction and the ligament size of the material. At high volume fractions (close to 50%) the connectivity shows a very weak relationship to the ligament size but as the volume fraction decreases this relationship strengthens and a decreasing ligament size results in a decrease in connectivity. As the connectivity decreases the number of unconnected ligaments increases and hence the load bearing path within the material becomes smaller, thus offering less resistance and hence resulting in a more compliant material. This explains why a dependence of the Young's modulus on ligament diameters is noted at lower volume fractions, but is less notable at larger volume fractions. This was also noted by Liu et al. [47] and Liu and Jin [53].

Hu et al. [49] questioned why structures which have the same connectivity density as nanoporous gold but are topologically different are far more compliant, and found that when the volume fraction of NPG was considered to be only that of ligaments that were truly load bearing (by removing 'dangling' ligaments) the increased compliance was recovered. This further emphasises the effects of connectivity on the stiffness of NPG. Using finite element simulations, Huber et al. [56] investigated how the amount of disorder within the ligament network affects the effective elastic response of NPG. This was further expanded by Lührs et al. [48] and Roschning and Huber [57]. They suggest that a more compliant material is the result of a change in the deformation modes of the ligaments from the majority axial compression within ligaments of ordered structures to now include more bending modes due to ligaments being misaligned to the loading axis.

Jiao et al. [55], further found that only if the ligament junctions are significantly larger than the ligament diameters does an increase in disorder affect the Young's modulus. Structures with thick ligaments only show a weak relationship between disorder and Young's modulus. They also found that the ratio of the ligament length to the diameter of the ligaments influenced the Young's modulus. Mangipudi et al. [58] agreed with this in part and concluded that the Young's modulus is far less sensitive to the morphological characteristics of the ligaments such as the ligament length, curvature and aspect ratio compared to the material's topological characteristics such as genus and nodal connectivity. This was confirmed by comparing finite element simulations of real NPG with gyroid structures. They showed that at different values of scaled genus (a measure of the overall connectivity per unit characteristic foam volume) the Young's modulus varies linearly. Finally, Soyarslan et al. [59] found that the dependence of

Young's modulus is, in part, due to a change in the surface-area-to-volume ratio and concluded surface elasticity to be an important factor in NPG.

Ligament deformation mode

The exceptional compressibility of nanoporous gold is suggested to be a result of the deformation mode of the ligaments. Using experimental methods, Pia et al. [60] noted that the large size of the nodal junctions results in the rigidity during deformation, whereas along the length of the ligaments significant deformation would occur, thus dictating the deformation behaviour of the material. In their investigation of cellular solids which are comparable to metal foams, Gibson and Ashby [61] found that the deformation mechanism greatly influences the stiffness of cellular solids. As open foam cellular solids share some similarities with nanoporous metals such as interconnectivity, these findings may shed light on the deformation mechanisms that give nanoporous metals some of their unique properties. They found that with a largely bending mode of deformation the material stiffness scales quadratically as the density increases compared to a linear relationship noted for materials with tension/compression dominated deformation modes. Thus, materials that display mostly bending dominated deformation present a far more compliant macroscopic material response. Deshpande et al. found agreement with this in their analysis of cellular solids using pin-jointed strut structures [62].

Using finite element simulations to inspect the complex microstructure of nanoporous gold one is able to investigate its deformation mechanism. Huber et al. [56] found bending to be the dominant loading case in nanoporous gold while Jiao [55] showed a mixed mode in the deformation of ligaments whereby both bending and torsion are prevalent. This multi-component deformation mode within the ligaments was similarly found from simulations carried out by Pia et al [63]. Choi [64] discussed how the type of bending that occurs in nanoporous metals may be that of cantilever bending and not only three-point bending as was suggested by Gibson and Ashby [61]. Cantilever bending is more compliant and could thus produce a more compliant macroscopic response.

1.2.2 Nanoporous gold/polymer composite

Nanoporous metals have been proposed for use in chemical, electrical and structural applications due to their favourable properties in compression above other conventional materials [10]. However, their poor performance in tension presents an obstacle to their utility. A material that exhibits less tension/compression asymmetry in strength and ductility could be used in a much wider variety of structural applications as the type of

loading it could experience would not have to be taken into account as carefully during the design process. Additionally, a significantly more ductile material could be shaped using conventional metal forming processes such as drawing and rolling. This would be highly advantageous over the complex moulding processes involved in manufacturing, for example, fibre-reinforced composites.

In an attempt to improve the ductility of NPG, Weissmüller [5] created a nanocomposite by impregnating nanoporous gold with a polymer. This new nanocomposite has several appealing properties. The first, and most obvious improvement, is its enhanced ductility. Wang and Weissmüller [5] showed qualitatively the improved tensile ductility using a three-point bending test the results of which can be seen in Figure 1.4(a).

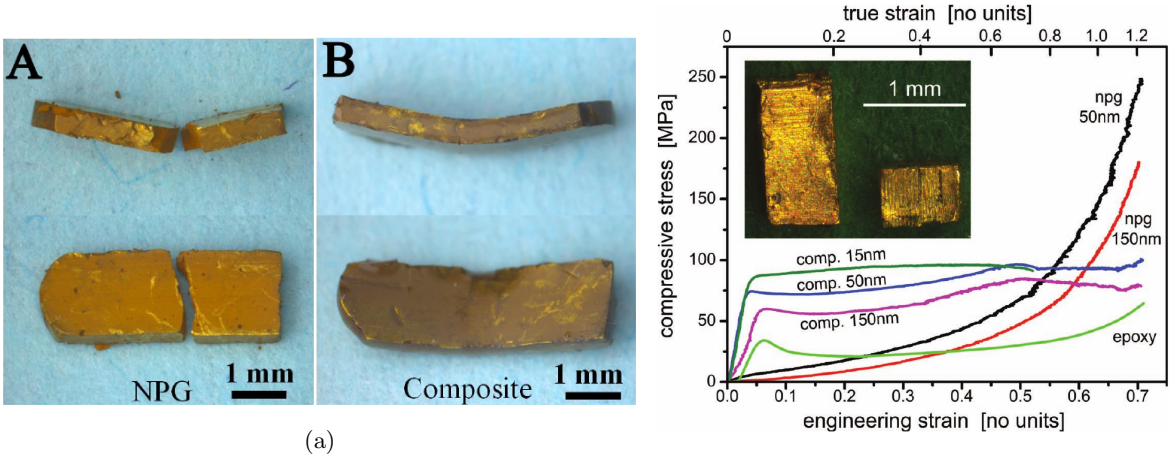

(a) (b)

Fig. 1.4: Three point bending and compression testing of NPG versus the gold/polymer nanocomposite (a) Comparative tensile ductility under a three point bending test and (b) improved strength and hardness under compression, taken from [45] [5].

Here, one can compare NPG to the nanocomposite with the former having fractured with no visible plastic deformation, while the latter has undergone significant deformation without any apparent macroscopic fracture. A maximum tensile strain of ≈10% was recorded for this sample. Wang et al. [44] further investigated the tensile behaviour of this nanocomposite under uniaxial tensile and four-point bending tests. Although the nanocomposite still showed a weaker response in tension compared to compression, samples undergoing uniaxial tensile tests showed strains of between 1 and 10% (depending on the polymer used and the characteristic ligament size of the native NPG). As expected, these tensile tests showed not only an increase in strength over their pure

[5] See footnote 3

polymer counterparts, but also a significant increase in fracture strength over pure nanoporous gold samples tested in tension. The samples showed an increasing strength with decreasing ligament size as is consistent with the 'smaller is stronger' relationship. A decreasing strain at failure with decreasing ligament size was also noted, which is consistent with the classical trend of a decrease in ductility with an increase in strength. The four-point bending test again revealed no apparent fracture of the nanocomposite at a strain of 2%. A significantly stronger response compared to the uniaxial tensile test was seen. Microbeam bending experiments were conducted by Hu [65] to further study the fracture properties of the nanocomposite. The microbeam was able to withstand longitudinal strains between 2 and -2% up to a maximum load of 0.41 mN.

Wang et al. [44] also found, upon inspection of the fracture surface, significant deformation of the metal ligaments in the form of necking before fracture. Hu [65] found cracks at the gold/polymer interfaces and within each constituent in his microbeam experiments. Crack growth within the epoxy was often hindered by the presence of gold ligaments along the crack path. Again, necking was also seen in the gold ligaments at the fracture surface of these beams.

In addition to the enhanced ductility, gold/polymer nanocomposites showed other favourable properties compared to pure NPG. Micro-compression and nano-indentation testing revealed hardness values and yield strengths greater than either of the constituents at a variety of ligament diameters (Figure 1.4(b)) [5, 44, 45, 65]. This is contradictory to a rule-of-mixtures type of behaviour where the properties would be a weighted average of the two constituents. The trend of an increase in mechanical property with decreasing ligament diameter was also still prevalent (Figure 1.5).

The origin of the unexpected exceptional strength above either constituent individually is not fully understood. Wang and Weissmüller [5] suggested a possible change in deformation mode from bending to normal loading to be the explanation. This would be consistent with the principles underlying the Gibson-Ashby strength relations for open-celled foams. Possible interfacial phenomena were also suggested as strengthening mechanisms.

The addition of a second material to nanoporous metals has also created the opportunity for new or improved functionality. For example, a nanoporous gold/metal-oxide hybrid structure created by Lang et al. [66] showed significantly increased conductivity and capacitance for storing electrical charge, thus promoting it as a material to be used as an electrode in super capacitors. A polypyrrole decorated NPG film cre-

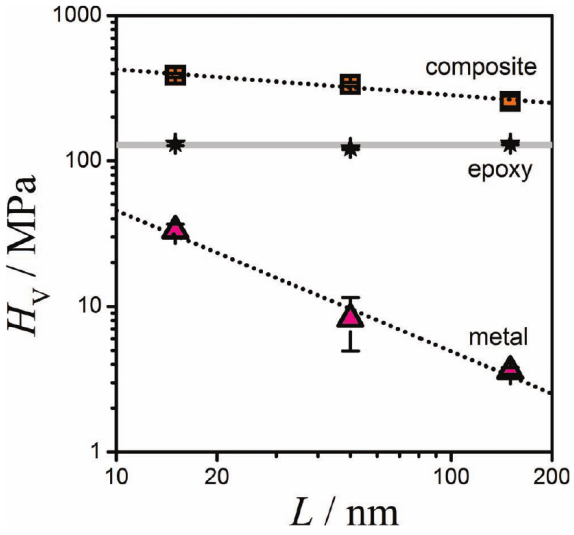

Fig. 1.5: Hardness values of the nanocomposite and nanoporous gold at three different ligament diameters. Hardness values of the polymer constituent (epoxy) are also shown. Taken from [5][6].

ated by Meng and Ding [67] also showed favourable properties such as high power and energy densities, which make it a promising candidate as an energy storage material in applications such as wearable electronic devices. The impregnation of an aqueous electrolyte into the pores of a nanoporous gold provide an environment in which piezoelectric behaviour may occur due to a charge displacement at the interface [68]. This material could thus be used in strain sensing or electro-mechanical actuation applications. Detsi et al. [69] showed that under electrochemical actuation, an electrochromic polymer coated nanoporous gold could be used in artificial muscle applications due to the reversible dimensional and colour changes observed.

Numerical investigations on this nanocomposite material are fairly limited. Bargmann et al. [50] developed a continuum based framework to model the polymer and gold material and applied it to a simple honeycomb structure to investigate deformation mechanisms. They concluded that ligament connectivity is a very important strengthening and stiffening mechanism. The simplicity of this model however limits the conclusions that can be drawn from it. Soyarslan et al. [70] further investigated the Young's modulus and Poisson's ratio with respect to a change in metal volume fraction using a more realistic material model. Scaling laws to describe the relationships for these properties were also suggested. Li et al. [71] investigated the mechanical behaviour of gold/polymer nanocomposites and found the axial yielding of the ligaments to be a significant influence on the yielding of this material under compression. They found no

[6] See footnote 3

relationship between the Young's modulus and the ligament size.

A finite element investigation into the effects of merely coating nanoporous gold with a polymer (polypyrrole) and the effect of the thickness of the coating on Young's modulus, was carried out by Gnegel et al. [72]. They found a significant increase in the stiffness of the composite even when only a thin coating was applied. The increase in stiffness was even greater than that which would be expected if thicker ligaments of the gold (a significantly stiffer material) were used instead. The creation of new connections between neighbouring ligaments, thereby increasing the connectivity of the network, was suggested as one of the main reasons for this increase. Gnegel et al. [72] also investigated numerically the elastoplastic response of this material using a von Mises plasticity material model for the gold material. As an alternative to the finite element method, a finite cell method was used to find the elastoplastic parameters for the polypyrrole constituent by comparing the experimental and numerical stress-strain responses of coated nanoporous gold. These parameters were in good agreement with that of bulk polypyrrole, thereby offering an alternative numerical method for simulating nanoporous gold and its nanocomposites.

1.3 Computational micromechanics

A better understanding of the mechanisms and properties underlying the behaviour of hierarchical materials such as nanoporous gold and its composite would be important if one wished to tailor the use of these materials to an application, and in the development of new materials which contain these enhancing features. To do this, however, the response of micro and nanoscale features under various loading conditions need to be investigated. Experimentally, this often requires advanced and expensive laboratory equipment as well as the creation of many test specimens. The responses of these specimens are also likely to be affected by defects or imperfections, leading to erroneous conclusions. Analytical methods offer a way to calculate and predict certain macroscopic properties but are often only applicable to regular and relatively simple material geometries. Moreover, an understanding of the micromechanical mechanisms is often not addressed by these methods. On the other hand, computational methods such as those using the finite element method offer a powerful tool to understanding how micromechanical behaviour influences macroscopic properties [73]. Computational methods can not only capture the complex response of nanoscale features and their stress and strain microfields, but hundreds, if not thousands, of 'virtual' experiments can be conducted to investigate relationships that exist and these can be used to char-

acterise the macroscopic behaviour of materials.

A 'virtual' experiment requires the creation of a computational model that represents a sample of the material. A popular approach to do this is using a representative volume element (RVE). This is a small sample of the material that is large enough to capture the characteristic geometric features of a material, including its internal structural arrangement, while being small enough to be computationally feasible [74]. It is important for the condition of the separation of scales to be maintained, with $L^{\mu} << L^{RVE} << L^{M}$ where L^{μ}, L^{RVE} and L^{M} are the characteristic lengths of the microstructure, RVE and macroscopic body respectively (Figure 1.6).

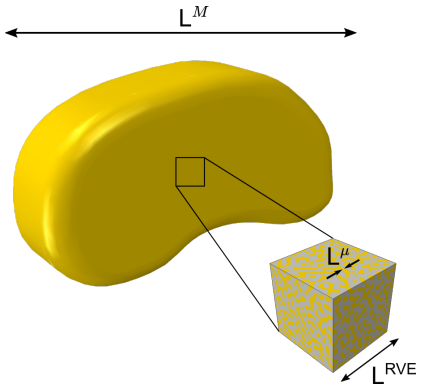

Fig. 1.6: Schematic of the different length scales within a gold/polymer nanocomposite. The condition of the separation of scales requires a RVE to be representative but also computationally feasible.

The size of a RVE depends on the characteristics of the material such as the number and types of constituents as well as their morphological and topological features.

There are several methods by which realistic RVEs can be created [75]. These include reconstructions from experimental data, physics-based methods or geometrical methods. Various methods have been used in the creation of a nanoporous gold RVE and its corresponding nanocomposite. Cubic [41], tetrakaidecahedron [76], diamond [41] and gyroid [41, 58, 63] structures created from mathematically described surfaces have previously been used as simplifications of NPG. These structures are, however, obviously different in both morphology and topology from realistic nanoporous metals and so conclusions drawn from them are limited. The ordered nature of these mathematically described structures further supports the notion that they can not fully capture the micromechanical response of nanoporous metals [56, 57, 77].

Realistic NPG RVEs are, clearly, the most appropriate models to use but their complex and stochastic structure has presented a problem in their correct and timely creation. Three methods have been used to construct realistic models: reconstructions based on X-ray nanotomography [49, 78, 79]; phase-field modelling whereby the dealloying process is simulated [39–41, 58, 71, 80–82]; and the use of level cuts on a generated Gaussian random field [83]. Reconstructions based on X-ray nanotomography involve sequential sectioning and imaging of the material and thereafter layering the images to re-create the three-dimensional features. This is an extremely laborious and time consuming method. Phase-field methods involve simulation of the dealloying process using molecular dynamic or Monte Carlo simulations of spinodal decomposition. This process simulates the kinetics involved in the phase separation occurring during dealloying. This is an extremely computationally expensive method and RVE construction can take several weeks. The last method [83] allows for three-dimensional RVEs that both morphologically and topologically representative of realistic nanoporous metals can be created within a few minutes. The RVEs used in this thesis are constructed from both the phase-field modelling process (Chapter 2) and the level cut method (Chapters 3 and 4).

1.4 Objective

The objective of this work is to understand the mechanical, fracture/damage and chemo-electro-mechanical behaviour of a gold/polymer nanocomposite material. The effects of different volume fractions of gold are also investigated and the micromechanical response and changes with a change in volume fraction are examined. Where possible, comparisons between nanoporous gold and its composite counterpart are explored. The benefits of the unique topological and morphological characteristics of nanoporous metals as a reinforcement phase compared to conventional composites is also probed. It is only by understanding the micromechanical response on a nanoscale that the possibility of optimizing material properties through micromechanical tailoring can be achieved. This works aims to add to this body of knowledge.

In this thesis, three loading cases are considered with the intent to observe the micromechanical response of nanoporous gold and/or gold/polymer nanocomposites using computational methods:

- The elastic response of a gold/polymer nanocomposite sample under compression;

- The fracture response of nanoporous gold and its corresponding nanocomposite under a compact-tension test; and
- The chemo-electro-mechanical response of a gold/polymer nanocomposite under an electrical stimulus.

1.5 Structure of thesis

The structure of this work is as follows:
Chapter 2 will look at the numerical homogenization of a gold/polymer nanocomposite. Three different boundary conditions will be utilized to calculate the effective elasticity tensor. The micromechanical response of this composite under compression will also be inspected where the stress and strain response along the centroid of the RVE and the loading case on several gold ligaments is probed.
Chapter 3 involves the simulation of 'virtual' compact-tension tests to inspect the crack initiation and propagation within gold/polymer nanocomposite samples. Samples with a range of volume fractions are simulated to investigate the relationship between the volume fraction and several mechanical properties such as the ultimate strength and fracture displacement. Samples of pure NPG are also simulated and highlight the ductility achieved by its impregnation with a polymer. Mechanisms facilitating this enhancement are noted.
In Chapter 4 a coupled chemo-electro-mechanical problem is modelled within the polymer phase of several nanocomposite RVEs with different volume fractions. A novel staggered explicit-implicit solution scheme is employed to solve the coupled multi-physics problem using a combination of Abaqus/Standard, Abaqus/Explicit and Python scripts. The effects of the volume fraction on the electrostatic field, concentration field and deformation within each constituent are explored with respect to its suitability as an actuator material.
Finally a summary of the insights gathered from the three loading cases and conclusions on how the micromechanical structures and material properties influence its macroscopic response are given in Chapter 5. Recommendations on future work that could be done to yield further insights on the properties of gold/polymer nanocomposite are also given.
The results of Chapter 2 and Chapter 3 have already been published in *Extreme Mechanics Letters* (doi:10.1016/j.eml.2017.09.006 and 10.1016/j.eml.2020.100815) respectively. Those of Chapter 4 have been published in the *Journal of the Mechanics and Physics of Solids* (doi:10.1016/j.jmps.2019.103848).

2

Elastic response of the nanocomposite

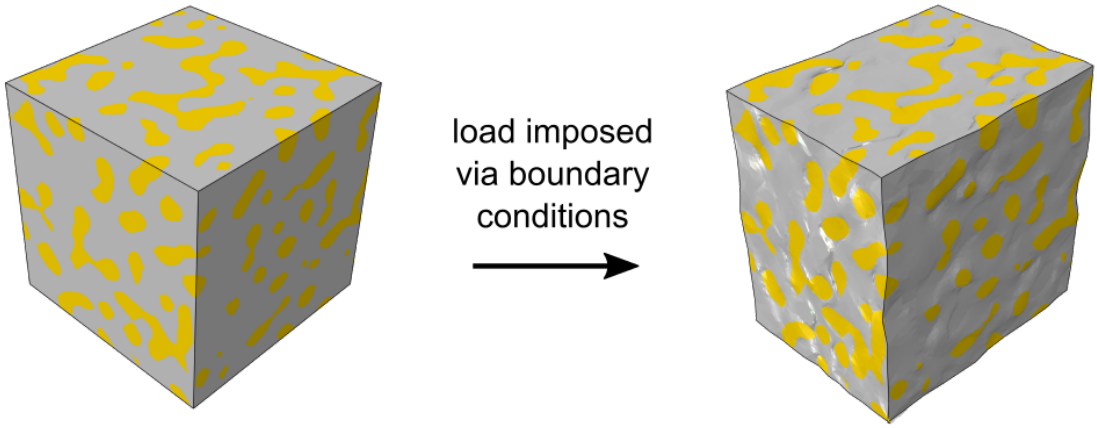

This chapter deals with the elastic response of a nanocomposite of nanoporous gold impregnated with epoxy. The investigation comprises two parts:

1. Use of computational homogenization strategies to determine the effective elastic properties of a representative volume element of the nanocomposite.
2. Investigation of the elastic response of the nanocomposite on a microscopic scale to probe the material response and ligament loading modes.

2.1 Introduction

A constitutive model describing the macroscopic behaviour of a material based on its microstructure is necessary in order to develop a more complete understanding of how the macroscopic response is affected by the deformation and response of the microstructure. Using representative samples of a material and the finite element method, a greater understanding of these relationships can be achieved. Additionally, if this material is to be used in large scale structural analyses, effective properties that capture the macroscopic material response without having to model the fully resolved microstructure are sought out. Numerical homogenization offers such a tool to determine the effective properties in the present case of a gold/polymer nanocomposite.

2.2 Homogenization

Upon loading, composites exhibit a complex stress strain response on a microscopic scale. The more complex the microstructure, the more complex this response is. It is this complex microstructural interaction, however, that produces unique macroscopic properties. In a large scale finite element analysis, modelling the complex microstructure of nanocomposites would be far too expensive computationally. For example, modelling the ligament network of a nanoporous gold material for any application larger than a few micrometres would require a prohibitively fine mesh discretization in order to capture the fully resolved microstructure. Homogenization, however, provides a means of replacing the complex heterogeneous microstructure with a homogeneous material that has the effective properties developed on the microscale (Figure 2.1).

Effective properties can be determined by either analytical or computational homogenization. Some fundamental analytical models include those of Eshelby [84] in which the effective property for a material comprising a single ellipsoidal inclusion within an infinite matrix under uniform loading is determined. This model has little applicability to real life materials but forms the basis of many other analytical models. For example, Mori and Tanaka [85] extended the Eshelby result by accounting for interaction between inclusions. This could be used for a composite with a moderate number of inclusions. Also based on the Eshelby result, the self-consistent and generalized self-consistent schemes [86, 87] calculate the effective properties of heterogeneous materials by making approximations on how the phases interact.

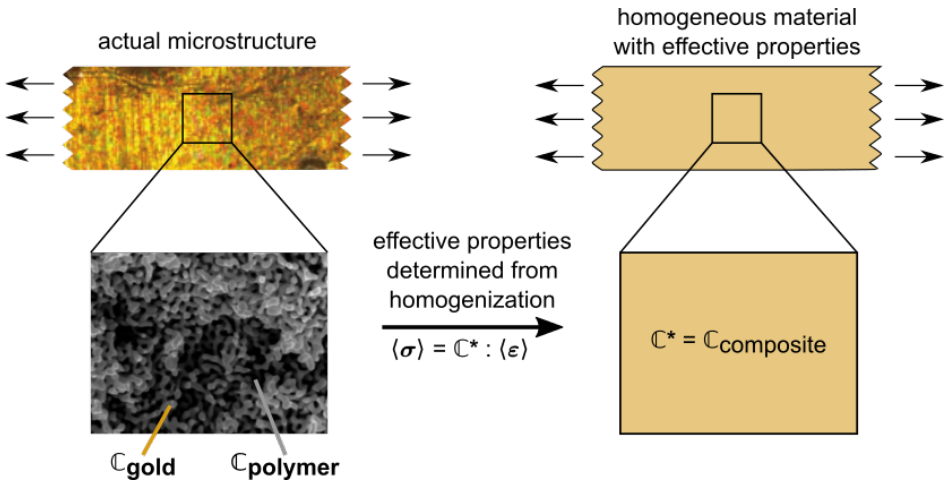

Fig. 2.1: Homogenization can be used to replace a heterogeneous material with a homogeneous one for a large scale structural analysis.

These and other analytical methods are, however, often limited in the types of microstructure to which they are applicable. Computational homogenization provides an avenue through which effective properties can be evaluated for any material that can be realized as an RVE. Computational homogenization involves the following steps (Figure 2.2):

1. A computational model of a small sample of the material is created, that is, a RVE. This sample must capture the features (topological and morphological) in the representative proportions that would be found in the real material;
2. This model is then deformed through the application of specified boundary conditions. The boundary conditions applied have to ensure that an energetic equivalence between the micro and macro scales is maintained;
3. A volume averaging technique is then applied to relate the microscopic quantities (stress and strain at individual points) to the macroscopic properties; and then finally,
4. The constitutive tensor is evaluated using the volume averaged stress and strain responses. This can then be used in subsequent large scale finite element simulations.

Homogenization also provides an opportunity for investigation of the effect of microstructural arrangements and inclusions in the response of a material at the macroscale. It provides a means of evaluating the influence of lower levels of hierarchy on the higher levels. Conducting experiments on several material specimens with all the possible structural arrangements would be prohibitive in both cost and time. Additionally,

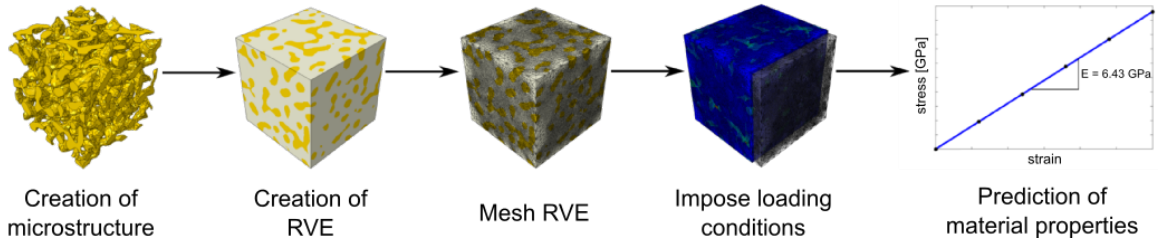

Fig. 2.2: Summary of computational homogenization technique applied to a RVE of a gold/polymer nanocomposite to determine the effective Young's modulus.

it would be difficult to investigate the relationships between certain physical or geometric properties and unique macroscopic properties. At the least, this would require additional equipment and complex analysis techniques. Homogenization enables one to conduct a large number of 'virtual' experiments and extensive investigations into how the microstructure influences the macroscopic properties. Probing field variables of e.g., stress, strain or deformation on the microscale and how they develop and change with different microstructures is also immediately available.

2.3 The homogenization problem

The micro- and macroscales of a material are linked by an effective constitutive tensor $\mathbb{C}^\star$. In the following, the homogenization problem is introduced and the procedure for obtaining $\mathbb{C}^\star$ described.

Consider a linear elastic body that occupies a domain $\bar{\Omega} \in \mathbb{R}^3$. With the assumption that it undergoes small deformations described by the Green small strain tensor

$$\boldsymbol{\varepsilon} = \frac{1}{2}\left[\mathrm{Grad}\boldsymbol{u} + (\mathrm{Grad}\boldsymbol{u})^{\mathrm{T}}\right] \,, \tag{2.1}$$

where $\boldsymbol{u}$ is the displacement vector, the Cauchy stress and Green small strain tensors are related to each other by the elasticity tensor $\mathbb{C}$; that is,

$$\boldsymbol{\sigma} = \mathbb{C} : \boldsymbol{\varepsilon} \,. \tag{2.2}$$

Consider a small sample body representative of the fully resolved microstructure; this is referred to as an RVE, which occupies a domain Ω comprising two materials labelled 1 and 2, with a material 2 volume fraction of ϕ (see Figure 2.3). Each material is homogeneous, linear elastic and non-overlapping so that $\Omega_1 \cap \Omega_2 = \varnothing$. The boundary $\partial\bar{\Omega}$, with a normal vector given by $\boldsymbol{n}$, comprises Dirichlet boundary $\partial\Omega_u$ on which

displacements are prescribed, that is $\boldsymbol{u} = \bar{\boldsymbol{u}}$; and Neumann boundary $\partial\Omega_n$ on which tractions are prescribed, that is $\boldsymbol{t} = \bar{\boldsymbol{t}}$. With an RVE subjected to body forces $\boldsymbol{b}$, the equilibrium problem is as follows:
Find $\boldsymbol{u} \in \vee$ such that $\boldsymbol{u} = \bar{\boldsymbol{u}}$ on $\partial\Omega_u$ and

$$\int_{\Omega} \operatorname{Grad} \boldsymbol{w} : \boldsymbol{\sigma} \, \mathrm{dV} = \int_{\Omega} \boldsymbol{b} \cdot \boldsymbol{w} \, \mathrm{dV} + \int_{\partial\Omega_n} \boldsymbol{t} \cdot \boldsymbol{w} \, \mathrm{dA} \qquad \forall \boldsymbol{w} \in V, \tag{2.3}$$

where $\vee$ is the test space of functions which together with their first derivatives are square-integrable, and which satisfy $\boldsymbol{w} = \boldsymbol{0}$ on $\partial\Omega_u$.

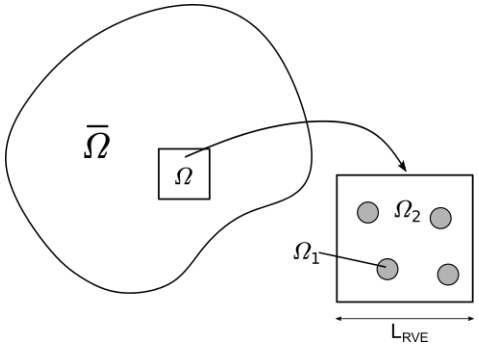

Fig. 2.3: Macroscopic homogenization problem description with magnified heterogeneous microscopic structure.

The effective response is characterized by the relation

$$\langle \boldsymbol{\sigma} \rangle_{\Omega} = \mathbb{C}^{\star} : \langle \boldsymbol{\varepsilon} \rangle_{\Omega} \,, \tag{2.4}$$

where

$$\langle \cdot \rangle_{\Omega} = \frac{1}{\Omega} \int_{\Omega} \cdot \, \mathrm{d}\Omega \tag{2.5}$$

represents an averaged quantity, and $\mathbb{C}^{\star}$ is the effective (homogenized) elasticity tensor. This quantity is the elasticity tensor that would be used in a macroscale analysis.

2.3.1 Hill-Mandel Condition

The boundary value problem applied to the RVE must satisfy the Hill-Mandel criterion [88]

$$\langle \boldsymbol{\sigma} \rangle_{\Omega} : \langle \boldsymbol{\varepsilon} \rangle_{\Omega} = \frac{1}{\Omega} \int_{\Omega} \boldsymbol{\sigma} : \boldsymbol{\varepsilon} \, \mathrm{d}\Omega. \tag{2.6}$$

which states that the average of the work (right-hand side term) must equal the work done by the average quantities (left-hand side term) when the body force is constant

or absent. This condition ensures that the work done at the microscale is equal to the work done at the macroscale.

2.3.2 Averaging theorems

For completeness two averaging theorems are introduced:

The average strain theorem For an RVE under uniform displacement boundary conditions, the volume average of the strain is equal to the strain on the boundary.

$$\langle \boldsymbol{\varepsilon} \rangle_{\Omega} = \mathcal{E} \,. \tag{2.7}$$

The average stress theorem For an RVE under body forces and uniform traction boundary conditions, the volume average of the stress is equal to the stress on the boundary.

$$\langle \boldsymbol{\sigma} \rangle_{\Omega} = \mathcal{L} \,. \tag{2.8}$$

2.3.3 Boundary conditions

Three types of boundary conditions can be applied which satisfy the Hill-Mandel condition: kinematic uniform, static uniform and periodic boundary conditions. These boundary conditions ensure that their application on the smallest RVE size possible does not affect the aggregate response of the material by ensuring only small boundary fluctuations relative to the size of the body are present. These boundary conditions are given by

Pure displacement/ kinematic uniform (KU):

$$\boldsymbol{u}|_{\partial\Omega_u} = \mathcal{E} \cdot \boldsymbol{x} \,; \tag{2.9}$$

Pure traction/ static uniform (SU):

$$\boldsymbol{t}|_{\partial\Omega_n} = \mathcal{L} \cdot \boldsymbol{n} \,; \quad \text{and} \tag{2.10}$$

Periodic displacement:

$$\boldsymbol{u}|_{\partial\Omega_u} = \mathcal{E} \cdot \boldsymbol{x} + \boldsymbol{v}, \tag{2.11}$$

where $\boldsymbol{v}$ is a periodic fluctuation.
The conditions (2.9) and (2.10) are often called homogeneous boundary conditions.

Homogeneous boundary conditions model the surrounding macro structure itself (Figure 2.4(a)) whereas periodic boundary conditions model a macrostructure of repeating periodic elements (Figure 2.4(b)).

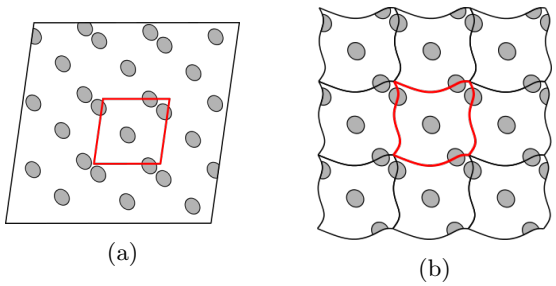

Fig. 2.4: Representation of the RVE (red square) from a 2D material using (a) homogeneous and (b) periodic boundary conditions. Using homogeneous boundary conditions, the macrostructure surrounding the RVE is represented whereas in periodic boundary conditions the macrostructure consists of repeated periodic units

Although for a large enough material sample the effective property calculated is independent of the boundary condition used, for a finite RVE size the correct effective property is bounded from above by the result obtained using displacement boundary conditions and from below by the result obtained using pure traction boundary conditions. Periodic boundary conditions are bounded by these two results. Thus, for a linear elastic material the effective Young's modulus is ordered as follows:

$$E^{\star}_{\mathrm{SUBC}} \leq E^{\star}_{\mathrm{PBC}} \leq E^{\star}_{\mathrm{KUBC}}\,. \tag{2.12}$$

Kinematic uniform boundary conditions provide a relatively stiffer response while static uniform boundary conditions yield a more compliant response. These results are obtained from the principles of minimum potential energy and maximum complementary energy. For a formal proof the reader is referred to [89]. For a variety of elastic materials it has further been shown that periodic boundary conditions produce a more accurate estimate for effective properties compared to displacement or traction boundary conditions at small RVE sizes [90–92]. For this reason, periodic boundary conditions are often favoured when the size of a RVE is limited.

2.3.4 Effective elastic properties

In the most general case, the effective elasticity tensor $\mathbb{C}^{\star}$ has 36 independent components. To determine these, six independent loading cases are applied, with the most

common ones given by

$$\mathcal{E}_{ii} = \beta \quad \text{(no summation over repeated indices)}\,, \tag{2.13}$$

$$\mathcal{E}_{ij} = \beta \quad (i \neq j)\,. \tag{2.14}$$

Here $i, j = 1, 2, 3$ and β is a prescribed constant value. The loading described by (2.13) represents the three normal loading cases and (2.14) represents the three shear loading cases (Figure 2.5).

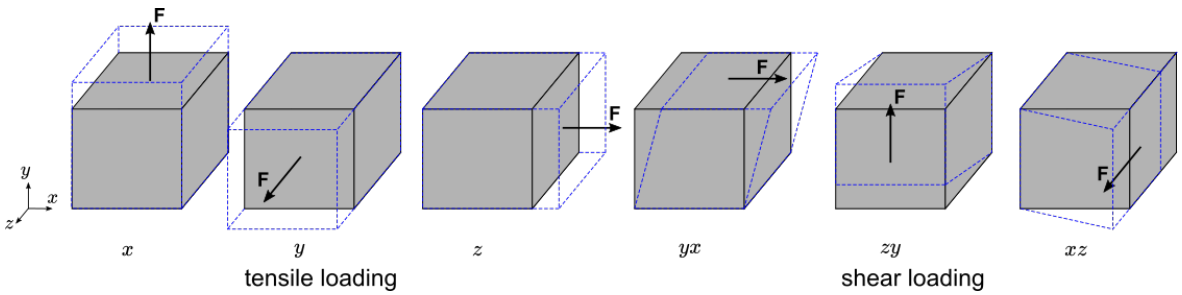

Fig. 2.5: Examples of six independent loading cases: 3 normal loading and 3 shear loading cases are shown from left to right.

The six independent loading conditions are applied through the boundary conditions given in the previous section. Each loading case yields six different volume averaged stress and strain components. Using Voigt notation, the 36 equations (six equations per loading case) are used to determine the 36 unknowns in the tensor $\mathbb{C}^\star$, defined by

$$\begin{pmatrix} \langle\sigma_{11}\rangle_\Omega \\ \langle\sigma_{22}\rangle_\Omega \\ \langle\sigma_{33}\rangle_\Omega \\ \langle\sigma_{12}\rangle_\Omega \\ \langle\sigma_{23}\rangle_\Omega \\ \langle\sigma_{13}\rangle_\Omega \end{pmatrix} = \begin{bmatrix} \mathbb{C}^\star_{1111} & \mathbb{C}^\star_{1122} & \mathbb{C}^\star_{1133} & \mathbb{C}^\star_{1112} & \mathbb{C}^\star_{1123} & \mathbb{C}^\star_{1131} \\ \mathbb{C}^\star_{1122} & \mathbb{C}^\star_{2222} & \mathbb{C}^\star_{2233} & \mathbb{C}^\star_{2212} & \mathbb{C}^\star_{2223} & \mathbb{C}^\star_{2231} \\ \mathbb{C}^\star_{1133} & \mathbb{C}^\star_{2233} & \mathbb{C}^\star_{3333} & \mathbb{C}^\star_{3312} & \mathbb{C}^\star_{3323} & \mathbb{C}^\star_{3331} \\ \mathbb{C}^\star_{1112} & \mathbb{C}^\star_{2212} & \mathbb{C}^\star_{3312} & \mathbb{C}^\star_{1212} & \mathbb{C}^\star_{1223} & \mathbb{C}^\star_{1231} \\ \mathbb{C}^\star_{1123} & \mathbb{C}^\star_{2223} & \mathbb{C}^\star_{3323} & \mathbb{C}^\star_{1223} & \mathbb{C}^\star_{2323} & \mathbb{C}^\star_{2331} \\ \mathbb{C}^\star_{1131} & \mathbb{C}^\star_{2231} & \mathbb{C}^\star_{3331} & \mathbb{C}^\star_{1231} & \mathbb{C}^\star_{2331} & \mathbb{C}^\star_{3131} \end{bmatrix} \begin{pmatrix} \langle\varepsilon_{11}\rangle_\Omega \\ \langle\varepsilon_{22}\rangle_\Omega \\ \langle\varepsilon_{33}\rangle_\Omega \\ 2\langle\varepsilon_{12}\rangle_\Omega \\ 2\langle\varepsilon_{23}\rangle_\Omega \\ 2\langle\varepsilon_{13}\rangle_\Omega \end{pmatrix}. \tag{2.15}$$

Due to the symmetry of the Cauchy stress and Green small strain tensors, $\mathbb{C}^\star$ has only 21 independent components. Thus (2.15) can be written as

$$\begin{pmatrix} \langle\sigma_{11}\rangle_\Omega \\ \langle\sigma_{22}\rangle_\Omega \\ \langle\sigma_{33}\rangle_\Omega \\ \langle\sigma_{12}\rangle_\Omega \\ \langle\sigma_{23}\rangle_\Omega \\ \langle\sigma_{13}\rangle_\Omega \end{pmatrix} = \begin{bmatrix} \mathbb{C}^\star_{11} & \mathbb{C}^\star_{12} & \mathbb{C}^\star_{13} & \mathbb{C}^\star_{14} & \mathbb{C}^\star_{15} & \mathbb{C}^\star_{16} \\ & \mathbb{C}^\star_{22} & \mathbb{C}^\star_{23} & \mathbb{C}^\star_{24} & \mathbb{C}^\star_{25} & \mathbb{C}^\star_{26} \\ & & \mathbb{C}^\star_{33} & \mathbb{C}^\star_{34} & \mathbb{C}^\star_{35} & \mathbb{C}^\star_{36} \\ & & & \mathbb{C}^\star_{44} & \mathbb{C}^\star_{45} & \mathbb{C}^\star_{46} \\ & \text{sym} & & & \mathbb{C}^\star_{55} & \mathbb{C}^\star_{56} \\ & & & & & \mathbb{C}^\star_{66} \end{bmatrix} \begin{pmatrix} \langle\varepsilon_{11}\rangle_\Omega \\ \langle\varepsilon_{22}\rangle_\Omega \\ \langle\varepsilon_{33}\rangle_\Omega \\ 2\langle\varepsilon_{12}\rangle_\Omega \\ 2\langle\varepsilon_{23}\rangle_\Omega \\ 2\langle\varepsilon_{13}\rangle_\Omega \end{pmatrix}, \tag{2.16}$$

where $\mathbb{C}^\star_{11} = \mathbb{C}^\star_{1111}$ and similarly for the other entries in (2.16), by comparing them with those in (2.15).

If one considers certain symmetries that exist within the microstructure of materials further simplifications to (2.16) can be made. For example, for a cubic crystal, which has three mutually orthogonal planes of reflection symmetry, (2.16) simplifies to

$$\begin{pmatrix} \langle\sigma_{11}\rangle_\Omega \\ \langle\sigma_{22}\rangle_\Omega \\ \langle\sigma_{33}\rangle_\Omega \\ \langle\sigma_{12}\rangle_\Omega \\ \langle\sigma_{23}\rangle_\Omega \\ \langle\sigma_{13}\rangle_\Omega \end{pmatrix} = \begin{bmatrix} \mathbb{C}^\star_{11} & \mathbb{C}^\star_{12} & \mathbb{C}^\star_{13} & 0 & 0 & 0 \\ & \mathbb{C}^\star_{22} & \mathbb{C}^\star_{23} & 0 & 0 & 0 \\ & & \mathbb{C}^\star_{33} & 0 & 0 & 0 \\ & & & \mathbb{C}^\star_{44} & 0 & 0 \\ & \text{sym} & & & \mathbb{C}^\star_{55} & 0 \\ & & & & & \mathbb{C}^\star_{66} \end{bmatrix} \begin{pmatrix} \langle\varepsilon_{11}\rangle_\Omega \\ \langle\varepsilon_{22}\rangle_\Omega \\ \langle\varepsilon_{33}\rangle_\Omega \\ 2\langle\varepsilon_{12}\rangle_\Omega \\ 2\langle\varepsilon_{23}\rangle_\Omega \\ 2\langle\varepsilon_{13}\rangle_\Omega \end{pmatrix}. \tag{2.17}$$

For an isotropic linear elastic material there are only two independent constants, and (2.16) becomes

$$\begin{pmatrix} \langle\sigma_{11}\rangle_\Omega \\ \langle\sigma_{22}\rangle_\Omega \\ \langle\sigma_{33}\rangle_\Omega \\ \langle\sigma_{12}\rangle_\Omega \\ \langle\sigma_{23}\rangle_\Omega \\ \langle\sigma_{13}\rangle_\Omega \end{pmatrix} = \frac{1}{3}\begin{bmatrix} [3\kappa^\star + 4\mu^\star] & [3\kappa^\star - 2\mu^\star] & [3\kappa^\star - 2\mu^\star] & 0 & 0 & 0 \\ & [3\kappa^\star + 4\mu^\star] & [3\kappa^\star - 2\mu^\star] & 0 & 0 & 0 \\ & & [3\kappa^\star + 4\mu^\star] & 0 & 0 & 0 \\ & & & 3\mu^\star & 0 & 0 \\ & \text{sym} & & & 3\mu^\star & 0 \\ & & & & & 3\mu^\star \end{bmatrix} \begin{pmatrix} \langle\varepsilon_{11}\rangle_\Omega \\ \langle\varepsilon_{22}\rangle_\Omega \\ \langle\varepsilon_{33}\rangle_\Omega \\ 2\langle\varepsilon_{12}\rangle_\Omega \\ 2\langle\varepsilon_{23}\rangle_\Omega \\ 2\langle\varepsilon_{13}\rangle_\Omega \end{pmatrix}, \tag{2.18}$$

where $\kappa^\star$ and $\mu^\star$ are the effective bulk and shear moduli respectively. From (2.18) these parameters can be computed from

$$3\kappa^\star = \frac{\left\langle \dfrac{\operatorname{tr}\boldsymbol{\sigma}}{3} \right\rangle_\Omega}{\left\langle \dfrac{\operatorname{tr}\boldsymbol{\varepsilon}}{3} \right\rangle_\Omega} \quad \text{and} \quad 2\mu^\star = \sqrt{\frac{\langle\boldsymbol{\sigma}'\rangle_\Omega : \langle\boldsymbol{\sigma}'\rangle_\Omega}{\langle\boldsymbol{\varepsilon}'\rangle_\Omega : \langle\boldsymbol{\varepsilon}'\rangle_\Omega}}. \tag{2.19}$$

Here $\operatorname{tr}(\cdot)$ denotes the trace of $(\cdot)$ while $(\cdot)' \overset{\text{def}}{=} (\cdot) - \frac{\operatorname{tr}(\cdot)}{3}\boldsymbol{I}$ is the deviator of $(\cdot)$. The effective shear and bulk modulus are related to the effective Young's modulus and

Poisson's ratio by

$$E^\star = \frac{9\kappa^\star\mu^\star}{3\kappa^\star + \mu^\star} \quad \text{and} \quad \nu^\star = \frac{3\kappa^\star - 2\mu^\star}{6\kappa^\star + 2\mu^\star}\,, \tag{2.20}$$

respectively.

2.3.5 Theoretical bounds

Classical analytical homogenization approximations include those of Voigt and Reuss bounds, and Hashin-Shtrikman bounds.

Reuss-Voigt bounds

By splitting the strain field into a volume averaged part and a fluctuating part, that is $\boldsymbol{\varepsilon} = \langle\boldsymbol{\varepsilon}\rangle_\Omega + \tilde{\boldsymbol{\varepsilon}}$, and using the positive-definiteness of $\mathbb{C}$ the following relation is obtained:

$$0 \leq \int_\Omega \tilde{\boldsymbol{\varepsilon}} : \mathbb{C}\tilde{\boldsymbol{\varepsilon}}\,\mathrm{dV}\,. \tag{2.21}$$

Expansion of (2.21) and application of (2.6) and (2.5) gives

$$0 \leq (\langle\boldsymbol{\varepsilon}\rangle_\Omega : (\langle\mathbb{C}\rangle_\Omega - \mathbb{C}^\star) : \langle\boldsymbol{\varepsilon}\rangle_\Omega)|\Omega| \tag{2.22}$$

Similarly, splitting the stress field into $\boldsymbol{\sigma} = \langle\boldsymbol{\sigma}\rangle_\Omega + \tilde{\boldsymbol{\sigma}}$ gives

$$0 \leq \left(\langle\boldsymbol{\sigma}\rangle_\Omega : \left(\langle\mathbb{C}^{-1}\rangle_\Omega - (\mathbb{C}^\star)^{-1}\right) : \langle\boldsymbol{\sigma}\rangle_\Omega\right)|\Omega| \tag{2.23}$$

The effective property can thus be bounded as follows:

$$\langle\mathbb{C}^{-1}\rangle_\Omega^{-1} \leq \mathbb{C}^\star \leq \langle\mathbb{C}\rangle_\Omega\,. \tag{2.24}$$

These bounds provide upper and lower limits for the effective property on the assumption of uniform strain (Voigt) and stress (Reuss) fields respectively in heterogeneous materials [74]. As neither a constant stress nor strain field represent the true state within a complex material, these bounds provide upper and lower limits to the true effective property value.

With an assumption of a uniform constant strain field, $\boldsymbol{\varepsilon} = \boldsymbol{\varepsilon}^0$ and $\langle\boldsymbol{\sigma}\rangle_\Omega = \langle\,\mathbb{C} : \boldsymbol{\varepsilon}\,\rangle_\Omega = \langle\mathbb{C}\rangle_\Omega : \boldsymbol{\varepsilon}^0$, which gives the Voigt bound $\mathbb{C}^\star = \langle\mathbb{C}\rangle_\Omega$. With the assumption of a uniform constant stress field, $\boldsymbol{\sigma} = \boldsymbol{\sigma}^0$ and $\langle\boldsymbol{\varepsilon}\rangle_\Omega = \langle\mathbb{C}^{-1} : \boldsymbol{\sigma}\rangle_\Omega = \langle\mathbb{C}^{-1}\rangle_\Omega : \boldsymbol{\sigma}^0$ which gives the

Reuss bound $\mathbb{C}^\star = \langle \mathbb{C}^{-1} \rangle_\Omega^{-1}$.

Based on a composite comprising a matrix and uni-directional fibres, the Reuss and Voigt bounds on the effective Young's modulus of a heterogeneous composite are given by

$$\frac{1}{E_{\text{Reuss}}} = \frac{1}{\Omega}\left[\int_{\Omega_1} \frac{1}{E_1} \mathrm{d}\Omega + \int_{\Omega_2} \frac{1}{E_2} \mathrm{d}\Omega\right] \quad \text{and} \quad E_{\text{Voigt}} = \frac{1}{\Omega}\left[\int_{\Omega_1} E_1 \mathrm{d}\Omega + \int_{\Omega_2} E_2 \mathrm{d}\Omega\right], \tag{2.25}$$

where E_1 and E_2 are the Young's modulus of materials 1 and 2 respectively that make up a composite of volume Ω. With a constant elastic modulus for materials 1 and 2 over the entire domain these can be expressed as

$$\frac{1}{E_{\text{Reuss}}} = \frac{1-\phi}{E_1} + \frac{\phi}{E_2} \quad \text{and} \quad E_{\text{Voigt}} = (1-\phi)E_1 + \phi E_2 \,. \tag{2.26}$$

Hashin-Shtrikman

The bounds developed by Hashin and Shtrikman were determined using the concepts of polarization and the principle of minimum potential energy [74]. As these bounds are sensitive to specimen size they are only valid for sample sizes significantly larger than the characteristic microstructure length. These provide the tightest bounds for a generalized isotropic heterogeneous material where no restrictions on the geometrical arrangement of the microstructure are made. The Hashin-Shtrikman bounds on the bulk and shear modulus are given by

$$\begin{aligned} \kappa_1 + \frac{\phi}{\frac{1}{\kappa_2-\kappa_1} + \frac{3[1-\phi]}{3\kappa_1+4\mu_1}} \leq \kappa^\star \leq \kappa_2 + \frac{1-\phi}{\frac{1}{\kappa_1-\kappa_2} + \frac{3\phi}{3\kappa_2+4\mu_2}} \quad \text{and} \\ \mu_1 + \frac{\phi}{\frac{1}{\mu_2-\mu_1} + \frac{6[1-\phi][\kappa_1+2\mu_1]}{5\mu_1[3\kappa_1+4\mu_1]}} \leq \mu^\star \leq \mu_2 + \frac{1-\phi}{\frac{1}{\mu_1-\mu_2} + \frac{6\phi[\kappa_2+2\mu_2]}{5\mu_2[3\kappa_2+4\mu_2]}}, \end{aligned} \tag{2.27}$$

where κ_1, μ_1 and κ_2, μ_2 are the shear and bulk moduli for material 1 and material 2, respectively. With these upper and lower values for shear and bulk moduli and using the expressions at (2.20) the Hashin-Shtrikman bounds on the Young's modulus and Poisson's ratio can be calculated.

These theoretical results bound the effective Young's modulus as follows:

$$E_{\text{Reuss}} \leq E_{\text{HS}\,\text{lower}} \leq E^\star \leq E_{\text{HS}\,\text{upper}} \leq E_{\text{Voigt}} \,. \tag{2.28}$$

2.3.6 Application of boundary conditions

In this work, two classes of boundary conditions are applied to the RVE: homogeneous and periodic.

Homogeneous boundary conditions

Two forms of homogeneous boundary conditions are considered in this work:

- Kinematic uniform boundary conditions, as given by (2.9), prescribe the displacement at all boundaries of an RVE, and

- Static uniform boundary conditions, as given by (2.10), prescribe the traction on all faces of an RVE.

Kinematic uniform boundary conditions

Application of kinematic uniform boundary conditions for the case of the three normal loads requires that three orthogonal faces are fixed in the direction normal to the face. Loads are then applied to one of the remaining three faces for each loading case as given by

Fixed boundaries	**Loading cases**
$u_y^{x_0} = 0$	$x-$direction: $u_x^{x_1} - u^{\text{load}} = 0$
$u_x^{y_0} = 0$	$y-$direction: $u_y^{y_1} - u^{\text{load}} = 0$
$u_y^{z_0} = 0$	$z-$direction: $u_z^{z_1} - u^{\text{load}} = 0.$

where u^{load} is a constant prescribed displacement.

For the case of the three shear loads, the loads are applied in in-plane directions with the corresponding opposite face constrained in the same in-plane direction as follows:

Fixed boundaries	**Loading cases**
$u_x^{y_0} = 0$	$yx-$direction: $u_x^{y_1} - u^{\text{load}} = 0$
$u_y^{z_0} = 0$	$zy-$direction: $u_y^{z_1} - u^{\text{load}} = 0$
$u_z^{x_0} = 0$	$xz-$direction: $u_z^{x_1} - u^{\text{load}} = 0.$

Rigid body motion is restricted in all six cases by fixing all degrees of freedom of the node at the origin.

Static uniform boundary conditions

Static uniform boundary conditions are applied by prescribing the traction at surfaces in order to simulate uniaxial and simple shear tests for the normal and shear loading cases respectively. All non-specified surfaces are prescribed with zero traction boundary conditions. These boundary conditions alone, however, lead to a non-unique solution due to rigid body motion. Various solutions have been proposed, including the use of the Lagrange multiplier method, mass-type diagonal perturbation [93], and the construction of free-flexibility matrix [94]. Here we address the singularity through the addition of semi-Dirichlet boundary conditions as developed by Javili et al. [95,96]. These prescribed-displacement boundary conditions prevent rigid body motion without invalidating the necessary assumption of a uniform stress distribution over the entire boundary, and are applied as follows:

- Translational motion is prevented by fixing a random point (point A in Figure 2.6) on the boundary in the $x-$, $y-$ and $z-$directions.
- Rotational motion is then prevented by further restricting the $x-$, $y-$ and $z-$directions separately at the three other nodes connected to point A (e.g., point B, C and D respectively in Figure 2.6) such that $X_x^B \neq X_x^A$, $X_y^C \neq X_y^A$ and $X_z^D \neq X_z^A$ where $X_{(\cdot)}^*$ is the $(\cdot)$ positional co-ordinate of point $*$. It should be noted that the locations of points B through D and their respective restricted degrees of freedom should also be selected so as to prevent spurious tractions as this would violate the foundational assumptions of SU boundary conditions.
- A traction force is then applied to the RVE.

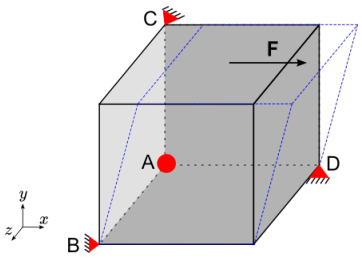

Fig. 2.6: Application of SU boundary conditions with semi-Dirichlet boundary conditions implemented to prevent rigid translation and rotational body motion.

Periodic boundary conditions

The application of periodic boundary conditions has been shown to be the best performing boundary condition for a finite RVE size. They produce the fastest convergence

to the effective property investigated with increasing RVE size for both periodic and non-periodic microstructures [90–92]. Classically periodic boundary conditions are applied by connecting two nodes that have the same co-ordinates but lie on opposite faces, and then prescribing a displacement difference. As such (2.11) becomes

$$\boldsymbol{u}^{\mathrm{k}+} - \boldsymbol{u}^{\mathrm{k}-} = \mathcal{E} \cdot [\boldsymbol{x}^{\mathrm{k}+} - \boldsymbol{x}^{\mathrm{k}-}], \tag{2.29}$$

where k+ and k− represent the k^{th} pair of opposite parallel faces. Since both $\mathcal{E}$ and $\boldsymbol{x}^{\mathrm{k}+} - \boldsymbol{x}^{\mathrm{k}-}$ are known a priori, the right hand side of (2.29) becomes a constant. This is easily implemented in commercial software via constraint equations and consequently solved using a constraint elimination method. As periodic boundary conditions are used to simulate a macro-structure consisting of periodic elements, continuity of both the displacements and tractions across the boundaries are required. The continuity of the displacements is explicitly satisfied by (2.29) while the traction continuity is implicitly ensured.

In order to have matching node pairs on parallel opposite faces a periodic mesh is required on the boundaries of the RVE. In the investigation of complex microstructures such as gold/polymer nanocomposites, however, this requirement would lead to an extremely fine mesh discretization which would be prohibitively computationally expensive. To circumvent this, various methods have been proposed to apply periodic boundary conditions to non-periodic meshes. Xia et al. [97] satisfied the requirements for periodic boundary conditions using unified boundary conditions on parallelepiped-shaped periodic RVEs. As this method is only applicable to parallelepiped-shaped RVEs with one type of microstructure, its limitations are obvious. Larsson et al. [91] included a weak micro-periodicity assumption of the displacement fluctuation field to enforce periodic boundary conditions. This method requires complex programming and is difficult to implement within commercial finite element software such as Abaqus.

Nguyen et al. [98] and Tyrus et al. [99] employed periodic boundary conditions by interpolating the displacements at the boundaries of the RVE using polynomials such as Lagrange polynomials, cubic splines and, in three dimensions, Coons patches. By doing so, the displacement at any point within an element on the negative face can be calculated by interpolating between the nodal values and thus a matching node no longer needs to exist. The interpolated value can then substituted for the $\boldsymbol{u}^{\mathrm{k}-}$ term in (2.29). Although this method is fairly simple it requires additional coding, which makes it unsuitable for use in commercial software.

As the microstructure is extremely complex for gold/polymer nanocomposites and, even without creating a periodic mesh, an RVE can easily contain several hundreds of thousands of elements, implementation in commercial software is necessary. Thus the master/slave approach, developed by Yuan and Fish [100] and utilized by Schneider et al. [101] and Kassem [102], which has been tailored for use in ABAQUS, will be used here. To accommodate the non-periodic mesh the use of tie constraints is adopted (the *TIE keyword within ABAQUS). This involves two opposite but parallel surfaces: one termed the slave surface, the other the master surface. The displacement of the nodes on the slave surface are constrained to the movement of the closest node/s by projection onto the master surface and utilizing the element shape functions (see Figure 2.7).

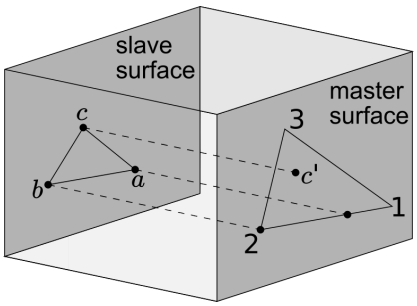

Fig. 2.7: Depiction of *TIE constraint in ABAQUSwhere node a is constrained by nodes 1 and 2, node b is constrained by node 2 and node c is constrained by nodes $1-3$ using element shape functions [100].

Due to limitations within ABAQUS further steps need to be taken to allow for (2.29) to be implemented. The full master/slave approach for one pair of sides of an RVE is summarised as follows (see Figure 2.8) :

- A replica of the master surface is created and placed at a small distance away from the slave surface;
- Tie constraints between the replicated master face and the slave face are defined;
- Equations linking the displacement of a reference node (nodes created externally form the RVE), nodes on the replicated master face and nodes on the original master face are created and;
- A displacement is prescribed at the reference node.

To ensure the model is not over constrained, the corner and edge nodes need to be treated individually with multipoint constraints and edge-coupling using node based tying (node-to-surface ties in ABAQUS).

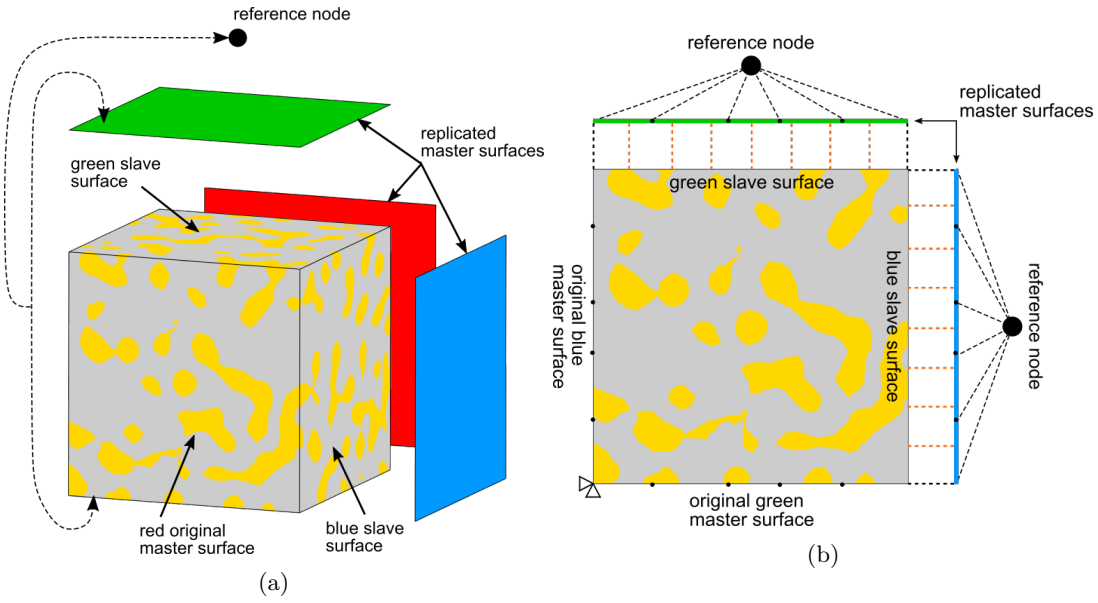

Fig. 2.8: Master/slave set-up for periodic boundary conditions on VE with a non-periodic mesh in (a) 3D and (b) 2D. The two-dimensional example is given as a schematic illustration and is extended to the 3D case in this work. The replicated master surfaces are given by the red, blue and green surfaces. Tie constraints (orange dashed line) are created between each replicated surface and corresponding slave surface parallel to it. Additionally constraint equations (black dashed line) are developed between corresponding reference nodes, replicated master surfaces and the corresponding original master surfaces.

Figure 2.9 shows the resulting deformation of an RVE after imposing kinematic, static uniform and periodic boundary conditions in compression. The kinematic uniform boundary conditions show relatively rigid boundaries which are as expected due to explicit prescription of the displacement along these boundaries. At the boundaries of the RVE with the periodic boundary conditions, a clear periodic deformation is noted.

2.3.7 Quantification of anisotropy

The effective elasticity tensor given in (2.16) is valid for a fully anisotropic material. It is important to be able to quantify the degree of anisotropy of a material for structural applications. A low degree of anisotropy will also result in a simpler elasticity tensor to describe the material.

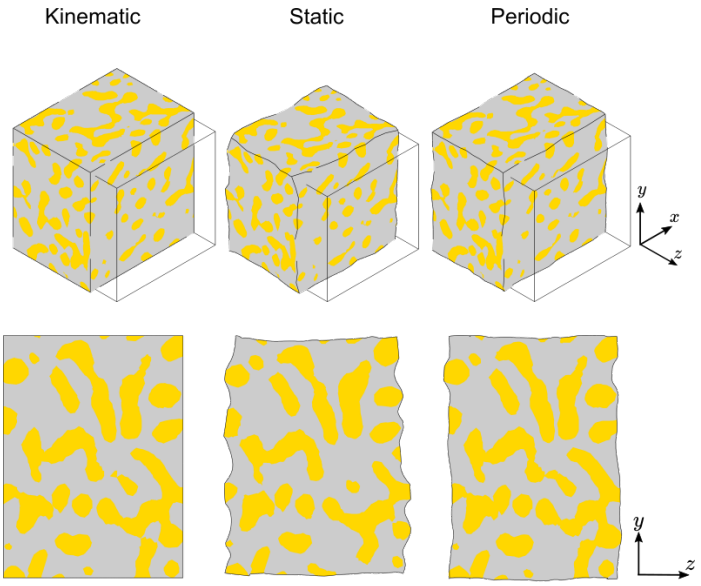

Fig. 2.9: Resulting deformation of a gold/polymer nanocomposite after imposing three different types of boundary conditions.

A measure of anisotropy of cubic crystals, the Zener anisotropy index [103], is defined by

$$A = \frac{2C_{44}}{C_{11} - C_{12}}\,, \tag{2.30}$$

where C_{ij} are the terms within the elasticity tensor $\mathbb{C}$ given in (2.16). $A = 1$ represents a purely isotropic material and a departure from this represents the degree of anisotropy. This measure quantifies anisotropy by comparing the resistance of a material to shearing across two different planes and in two different directions. Kanit et al. [104] used an alternative form of this measure, given by

$$A' = \frac{2Y_{44}}{Y_{11} - Y_{12}}\,, \tag{2.31}$$

where

$$Y_{44} = \frac{C_{44} + C_{55} + C_{66}}{3}\,, \quad Y_{11} = \frac{C_{11} + C_{22} + C_{33}}{3} \quad \text{and} \quad Y_{12} = \frac{C_{12} + C_{23} + C_{31}}{3}\,. \tag{2.32}$$

Chung and Buessem [105] modified the Zener index using empirical methods to produce an anisotropy measure of the form

$$A^C = \frac{\kappa^{\mathrm{V}} - \kappa^{\mathrm{R}}}{\kappa^{\mathrm{V}} + \kappa^{\mathrm{R}}} = \frac{3(A-1)^2}{3(A-1)^2 + 25A}\,, \tag{2.33}$$

where $A^C = 0$ indicates a purely isotropic material and the superscripts (V) and (R) represent the Voigt and Reuss bounds on the shear modulus. For polycrystalline materials these are given by [88]

$$9\kappa^{\mathrm{V}} = (C_{11} + C_{22} + C_{33}) + 2(C_{12} + C_{23} + C_{32}) \quad \text{and} \tag{2.34}$$

$$\frac{1}{\kappa^{\mathrm{R}}} = (S_{11} + S_{22} + S_{33}) + 2(S_{12} + S_{23} + S_{32})\,, \tag{2.35}$$

where S_{ij}, $i, j = 1, 2, 3$ are terms in the the compliance tensor $\mathbb{S} = \mathbb{C}^{-1}$. As a material becomes more anisotropic, the gap between the Reuss and Voigt bounds increases and so $A^C > 0$.

The above anisotropy indices do not, however, take into account the full tensorial nature of the elasticity tensor and are only applicable for cubic crystals where $C_{44} = C_{55} = C_{66}$. A universal anisotropy index A^U was thus introduced by Ranganathan and Ostoja-Starzewski [106] to take into account the possible non-isotropic bulk resistance of a crystal. This is defined by

$$A^U = 5\frac{\kappa^{\mathrm{V}}}{\kappa^{\mathrm{R}}} + \frac{\mu^{\mathrm{V}}}{\mu^{\mathrm{R}}} - 6\,, \tag{2.36}$$

where the Reuss and Voigt bounds for the bulk moduli are given by [88]

$$15\mu^{\mathrm{V}} = (C_{11} + C_{22} + C_{33}) - (C_{12} + C_{23} + C_{31}) + 3(C_{44} + C_{55} + C_{66})\,, \tag{2.37}$$

$$\frac{15}{4\mu^{\mathrm{R}}} = (S_{11} + S_{22} + S_{33}) - (S_{12} + S_{23} + S_{31}) + 3(S_{44} + S_{55} + S_{66})\,. \tag{2.38}$$

As with the Chung and Buessem index, $A^U = 0$ for an isotropic elastic material and departure from this indicates the extent of the crystal anisotropy.

2.4 Results and discussion

The homogenization and micromechanical analysis was carried out using Abaqus/Standard on a volume element (VE) of a gold/polymer nanocomposite (Figure 2.10). The VE was created within Abaqus by cutting and merging a homogeneous block with a pure NPG structure (developed by B.-N. Ngo from Helmholtz-Zentrum Geesthacht, Germany [81, 82]). The VE has a gold volume fraction of 29.7% and relative ligament size of 31.5 nm. Using Meshlab, a mesh of 437 913 linear tetrahedral elements was created. The properties of the gold and polymer constituents are given in Table 2.1.

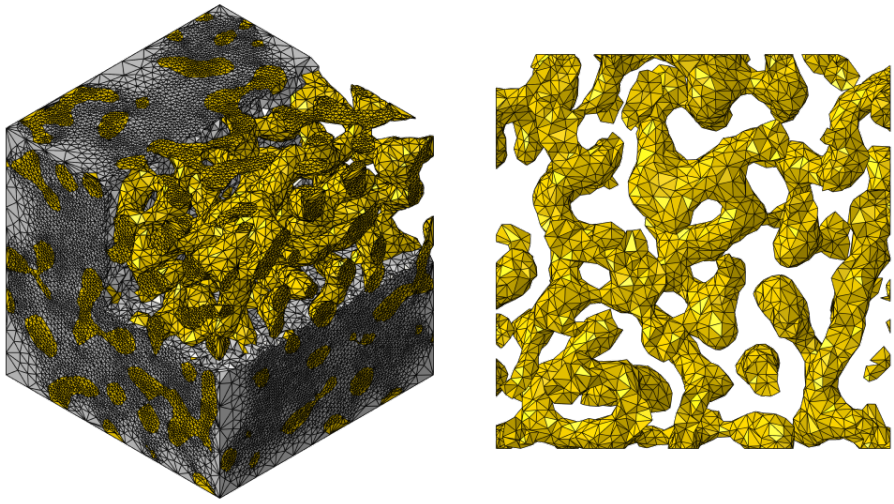

Fig. 2.10: Volume element of gold/polymer nanocomposite (grey=polymer, yellow=gold) with a cut-out showing the interconnected nanoporous gold network of ligaments. A 2D slice of the nanoporous gold is also shown.[1]

Table 2.1: Bulk material properties

Polymer [107]	symbol	value
bulk modulus	κ	1.63 GPa
shear modulus	μ	0.75 GPa
Poisson's ratio	ν	0.3
Gold [27]		
bulk modulus	κ	216.64 GPa
shear modulus	μ	27.08 GPa
Poisson's ratio	ν	0.44

2.4.1 Homogenization

The effective elasticity tensor resulting from each type of boundary condition is given in Table 2.2.

Looking at the entries and, most importantly, the location of the near zeroes in the three matrices, all three reveal an elasticity tensor similar to that of (2.17), that is, a cubic crystal. The extent of the anisotropy is calculated using the measures given in Section 2.3.7 and given in Table 2.3.

From Table 2.3 it is clear that this volume element is not only a cubic crystal but can also be approximated as an isotropic material. As a result, the full material response

[1] Reproduced with permission from Elsevier (https://doi.org/10.1016/j.eml.2017.09.006)

Table 2.2: Effective elasticity tensor results using each type of boundary condition.

$$\mathbb{C}^{\star}_{\text{KUBC}} = \begin{bmatrix} 7.50 & 2.66 & 2.63 & 0.09 & 0.06 & -0.03 \\ & 7.83 & 2.72 & 0.08 & 0.01 & -0.17 \\ & & 8.06 & 0.03 & -0.07 & -0.13 \\ & \text{sym} & & 2.40 & -0.05 & -0.06 \\ & & & & 2.54 & 0.04 \\ & & & & & 2.65 \end{bmatrix} \quad \mathbb{C}^{\star}_{\text{SUBC}} = \begin{bmatrix} 6.30 & 2.26 & 2.25 & 0.05 & 0.02 & -0.01 \\ & 6.73 & 2.31 & 0.04 & -0.01 & -0.10 \\ & & 6.74 & 0.02 & -0.05 & -0.09 \\ & \text{sym} & & 2.05 & -0.04 & -0.02 \\ & & & & 2.06 & 0.03 \\ & & & & & 2.15 \end{bmatrix}$$

$$\mathbb{C}^{\star}_{\text{PBC}} = \begin{bmatrix} 7.56 & 2.69 & 2.72 & 0.09 & 0.04 & -0.02 \\ & 7.85 & 2.73 & 0.09 & 0 & -0.12 \\ & & 8.03 & 0.02 & -0.04 & -0.07 \\ & \text{sym} & & 2.45 & -0.04 & 0 \\ & & & & 2.48 & 0.04 \\ & & & & & 2.54 \end{bmatrix}$$

Table 2.3: Measures of anisotropy of the effective elasticity tensors in Table 2.2. Isotropic materials have values of $A = 1$, $A' = 1$, $A^C = 0$ and $A^U = 0$.

Anisotropy index	symbol	Boundary condition		
		Static	Periodic	Kinematic
Zener	A	1.01	1.01	0.992
'Modified' Zener	A'	0.968	0.976	0.987
Chung and Buessem	A^C	2.6e-05	4.53e-06	8.26e-06
Universal anisotropy index	A^U	0.0610	0.0307	0.076

can be described using two effective material parameters $\kappa^\star$ and $\mu^\star$ as given by (2.19). Only one of the six independent loading cases is necessary to calculate these parameters. These parameters can then be used to calculate the effective Young's modulus $E^\star$ and Poisson's ratio $\nu^\star$ using (2.20).

In this work, three normal loading cases along each of the three major axes were applied to the volume element using each of the three boundary conditions. The average of the effective material parameters of each loading case for each type of boundary condition are given in Table 2.4.

The effective Young's modulus is in agreement with Wang [45] who recorded a value of 4.01 GPa for a gold/polymer nanocomposite with a 27% volume fraction and a ligament size of 35 nm ±10 nm. Samples of pure nanoporous gold with similar material parameters (30% gold volume fraction and $25-30$ nm ligament diameters) recorded by Balk et al. [27] gave a Young's modulus of 2.7 GPa. The nanocomposite is understand-

Table 2.4: Effective elastic properties calculated from numerical homogenization under three different boundary conditions. Theoretical bounds for the Young's modulus are also given.

Effective property		Boundary condition						
		Reuss	HS_{lower}	Static	Periodic	Kinematic	HS_{upper}	Voigt
bulk modulus	$\kappa^\star$ [GPa]			3.717	4.417	4.381		
shear modulus	$\mu^\star$ [GPa]			2.153	2.551	2.558		
Poisson's ratio	$\nu^\star$			0.257	0.258	0.255		
Young's modulus	$E^\star$ [GPa]	2.539	3.170	5.413	6.417	6.423	14.538	22.935

ably stiffer than pure NPG, however, only marginally so considering the large increase in compressive strength (1.5 times increase in stiffness with a 3.5 times increase in compressive strength [45]). Using the proposed scaling law for the Young's modulus of a gold/polymer nanocomposite given by [70]

$$E^\star = [E_{\mathrm{M}} - E_{\mathrm{P}}]\, \phi^{2.45} + E_P\,, \tag{2.39}$$

where E_M is the Young's modulus of the metal (i.e., gold in this case), and E_P is the Young's modulus of the polymer. A Young's modulus of 5.84 GPa is calculated which sits within the range of the imposed boundary conditions. Similarly they record a Poisson's ratio for the nanocomposite of 0.3; the results in Table 2.4 are in agreement with this.

As expected, results from the simulations lie within the theoretical bounds and agreement with the ordering of bounds according to (2.28). Although the upper and lower theoretical bounds span a large range of values in Table 2.4, the Hashin-Shtrikman bounds are noticeable tighter than the Reuss-Voigt bounds especially in the upper bound calculation. However, either of these bounds would clearly not be suitable for use as estimates for the nanocomposite.

The numerical homogenization results show the compliance of the SU boundary conditions and the stiffer response as a result of the KU boundary conditions. The periodic boundary conditions lie between these two as expected.The bulk modulus shows an unexpected result in that the KU boundary condition gives a slightly smaller value than that for the periodic boundary condition. This suggests that there is more resistance to volume change under periodic boundary conditions compared to KU boundary conditions. Under all three boundary conditions, the results are very similar thus confirming the representativeness of the volume element to the real material.

The numerical homogenization results all sit closer to the lower theoretical bounds. The nanocomposite is, thus, considered to be closer to a state of iso-stress than a state of iso-strain. Due to the stochastic arrangement of the gold ligaments it would be expected for the result to lie in the middle of the two theoretical bounds. The lower Reuss bound assumes the matrix (the more compliant phase) carries most of the load while the reinforcement (the stiffer phase) provides nominal strength. Such a situation would produce a low strength material. In the nanocomposite, however, this is not seen as the nanocomposite has a relatively compliant behaviour while maintaining a relatively high strength, two features that are contradictory in classical engineering materials.

2.4.2 Elastic response along centroidal axis

The maximum and minimum principal stresses and strains of the elements located along centroidal axis of the RVE are presented in Figure 2.11. The RVE is under compressive loading along the $x-$axis (also along the same axis as the centroidal elements) by means of displacement boundary conditions. The results from the compression of homogeneous blocks of gold and epoxy are also included.

Looking first at the principal strains, there is significantly more strain in the polymer than in the gold constituent. This is expected as the gold material is significantly more stiff. The difference between the maximum and minimum strain values for the gold (-0.009 to 0.007) is almost negligible compared to the polymer (-0.088 to 0.036). The maximum strains in both constituents are also much smaller and span a smaller range as would be expected under a uni-axial compression test. The tensile strains in the homogeneous block are a result of lateral expansion and, due to their differing Poisson's ratios, have different maximum strain values.

Compared to their homogeneous block counterparts, there is less strain in the gold constituent and more strain in the polymer constituent in the nanocomposite. The lower strain values of gold occur as it is very stiff and highly connected and will thus undergo minimal deformation. The network arrangement also allows for reorientation and realignment of the ligaments without significant strain occurring. To compensate for the lack of gold deformation, however, the polymer, which is more compliant, has to undergo a significant amount of strain to account for the volume change imposed on it. It thus deforms even more than its homogeneous counterpart.

Now focussing on the stress diagrams, as expected, higher stresses develop in the gold

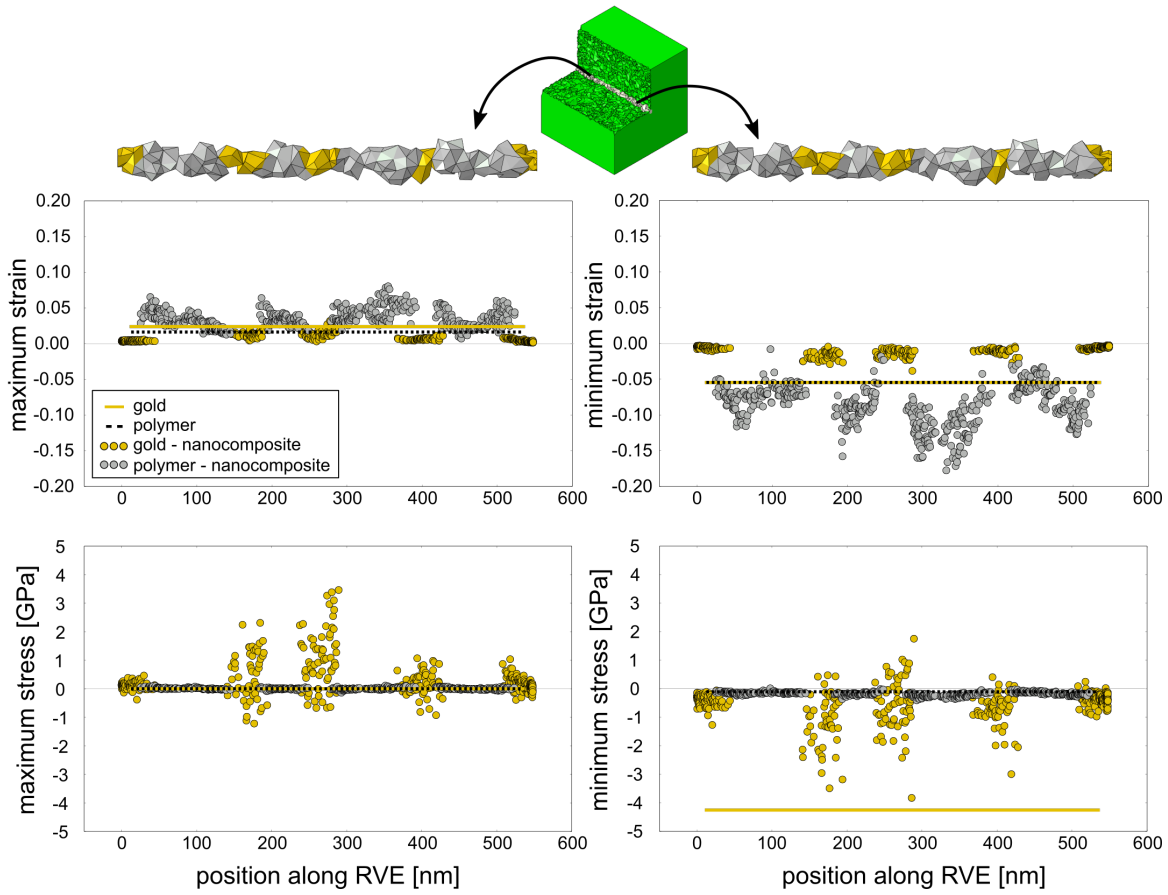

Fig. 2.11: Maximum and minimum principal stresses and strains along the centroid of the RVE: comparison of bulk gold, bulk polymer, polymer phase in the nanocomposite and gold phase in the nanocomposite. Significantly large tensile stresses and strains are generated in the composite despite simulation of a pure compression test. The gold within the composite shows considerable tensile and compressive stresses of equal magnitude. [2]

than in the polymer constituent. The homogeneous blocks show a maximum zero stress as the RVE is undergoing a uniaxial, unconstrained compressive deformation. The gold constituent within the nanocomposite, however, shows large maximum and minimum stresses of similar magnitudes. The large positive stress values result from the polymer deformation around it and a complex network interaction amongst the gold ligaments. A few elements in the centroid even have positive (tensile) minimum principal stresses. Although a relatively large minimum stress is seen in the gold elements, all elements still undergo a smaller stress than those in the pure homogeneous gold. This is, again, a result of the combination of the ability of the gold ligaments to re-orientate and the compliance of the surrounding polymer.

There are marginally larger minimum stress magnitudes in the nanocomposite's poly-

[2] Reproduced with permission from Elsevier (https://doi.org/10.1016/j.eml.2017.09.006)

mer constituent compared to its homogeneous counterpart as a result of the much larger deformation that the polymer has to undergo to compensate for the stiffness of the gold.

These diagrams show how, while the nanocomposite and the homogeneous counterparts are deformed macroscopically by the same amount, the polymer allows for this deformation by undergoing most of the strain while the gold withstands the stresses that develop (albeit less that its homogeneous counterpart in compression).

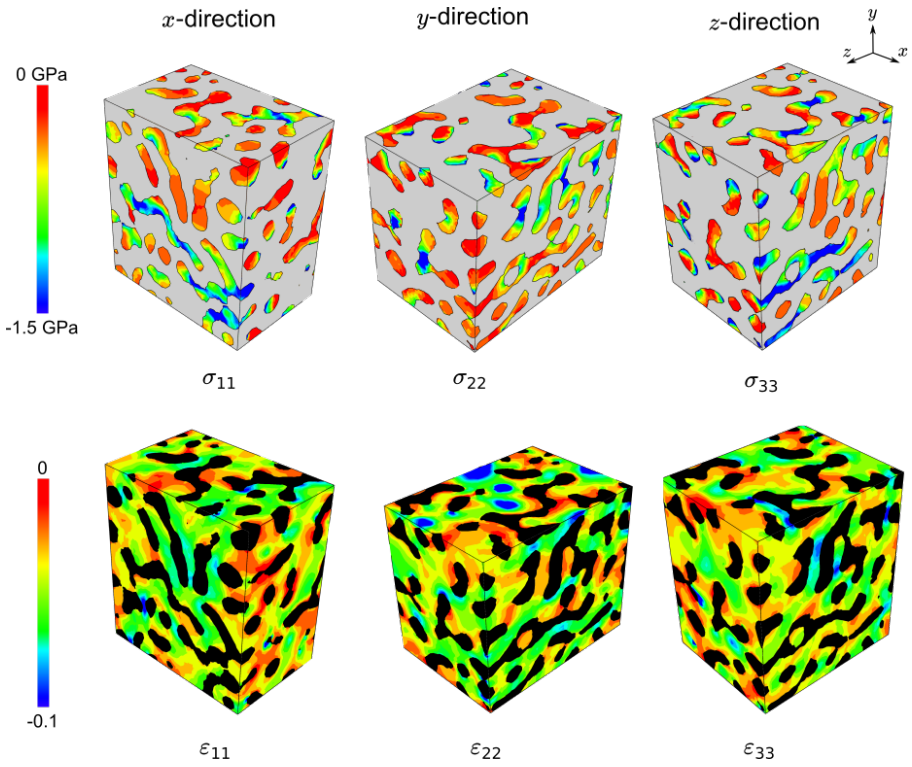

Fig. 2.12: Contour plots of the volume element under three uniaxial compression loadings ($x-$, $y-$ and $z-$direction, left to right respectively). Top row: Stress in gold constituent (polymer in grey). Bottom row: Strain in polymer constituent (metal in black). Red areas indicate tensile or near tensile values while blue areas are locations compression.

Figure 2.12 shows contour plots of the stress in the gold constituent (top row) and the strain in the polymer constituent (bottom row) under the three different compressive loading cases and in the direction of each RVE's respective loading direction. In the top row the polymer is shown in grey and in the bottom row the gold material is shown in black as they do not undergo large stresses or strains respectively. Only the compressive stresses and strains are given, where red areas indicate tensile or near tensile values and blue areas indicate compression values.

As expected, gold ligaments that lie parallel to the axis of compression show areas of high compressive stress. The highest stresses occur along the ligament necks with lower compressive stress at the nodes. The strain in the polymer however, does not show the same trend. There is no obvious correlation between the direction of compression and the locations of high compressive strain. This is due to the high volume of polymer in the nanocomposite which allows for a distribution of the strain throughout the material. The locations of compression of the polymer occur in areas where the gold ligaments are very close and are restricting the polymer. The high stiffness of the gold means it will not deform and so the polymer is forced to deform around and between the gold ligaments.

2.4.3 Loading case of the ligaments

To investigate the dominant loading mode, the magnitude of the loading modes on the cross sections of the gold ligaments within the nanocomposite RVE undergoing compression along the $x-$axis were investigated. Ten ligaments were investigated, two ligaments orientated along each principal direction and four other randomly orientated ligaments. The normal and shear stresses were calculated using the traction vector located at the centroid of the elements on the ligament cross sections. From this the total of the normal and shear forces were calculated as well as the bending moment and the torque acting on the ligament surface. The maximum bending moment and the orientation of its axis was determined by calculating the bending moment at several angles and selecting the angle that produces the largest bending moment. The average values of each loading mode for the ten ligaments are given in Table 2.5.

Table 2.5: Average loading mode magnitude experienced by ten ligaments within the gold/polymer nanocomposite when undergoing compression

Loading mode	Magnitude
Bending moment	4.225 μN.nm
Torque	2.279 μN.nm
Normal force	1.233 μN
Shear force	0.229 μN

From Table 2.5 a complex mixture of loading modes is noted as the deformation of one ligament influences many other differently aligned ligaments within the complex interconnected network. However, it is evident that bending is more prevalent than torque

and normal loading is significantly more prevalent than shear loading. That being said, there is still significantly more shear force than one would expect for a pure compression test. Bending is shown to be the most dominant loading mode in this material.

The loading mode of the ligaments within a foam has previously been shown to affect its strength and stiffness. Deshpande et al. [62] state that stiffer and stronger foams show tension/compression dominated loading. This is in agreement with the work of Gibson and Ashby on open-cell metal foams [61, 108]. As discussed in Section 1.2.1 strength and stiffness scale with density much faster if the deformation mode is tension/compression dominated, compared to one in which bending is the dominant mode. In pure NPG it has been suggested that a shift from a tension/compression loading mode in ordered metal foams to a bending dominated loading mode due to ligament disorder may contribute to the compliance of the material under compression [48, 56, 57]. Under tensile loading NPG has a predominantly tension/compression loading mode which thus enhances its brittleness. As a tension/compression symmetry is noted in the loading modes within the nanocomposite RVE, there would be a large amount of bending when undergoing tensile loading, which supports the suggestion that a change in the loading mode in the nanocomposite towards bending causes the improved ductility of this material [5].

The distributions of the shear and normal stresses on the faces of three exemplar ligaments are shown in Figure 2.13. Only one distribution of each of the principally orientated ligaments is shown as the trend observed in either ligament along one orientation was very similar. As there were no clear trends among the randomly orientated ligaments they are not discussed further. The top row in Figure 2.13 depicts the normal force vectors acting either into (filled in circles) or out of (encircled crosses) the page. The size of these markers show the magnitude of the force vector. The bottom row depicts the shear forces acting on the plane of the ligament's cross sectional area with the length of the arrow indicating the magnitude of the vector. In these diagrams, the ligament cross sectional areas are outlined and the forces are located at the centroids of the faces of the elements on these cross sections.

In Figure 2.13 there are clear areas in all three ligaments of higher normal forces with a decrease in these as one moves across the ligament. In the $y-$orientated ligament, a change in the direction of the normal forces is very clear. The compression aligned ligament ($x-$orientated ligament) has a very large normal force and a significant bending moment. The significant compressive stresses in compression-axis aligned ligaments

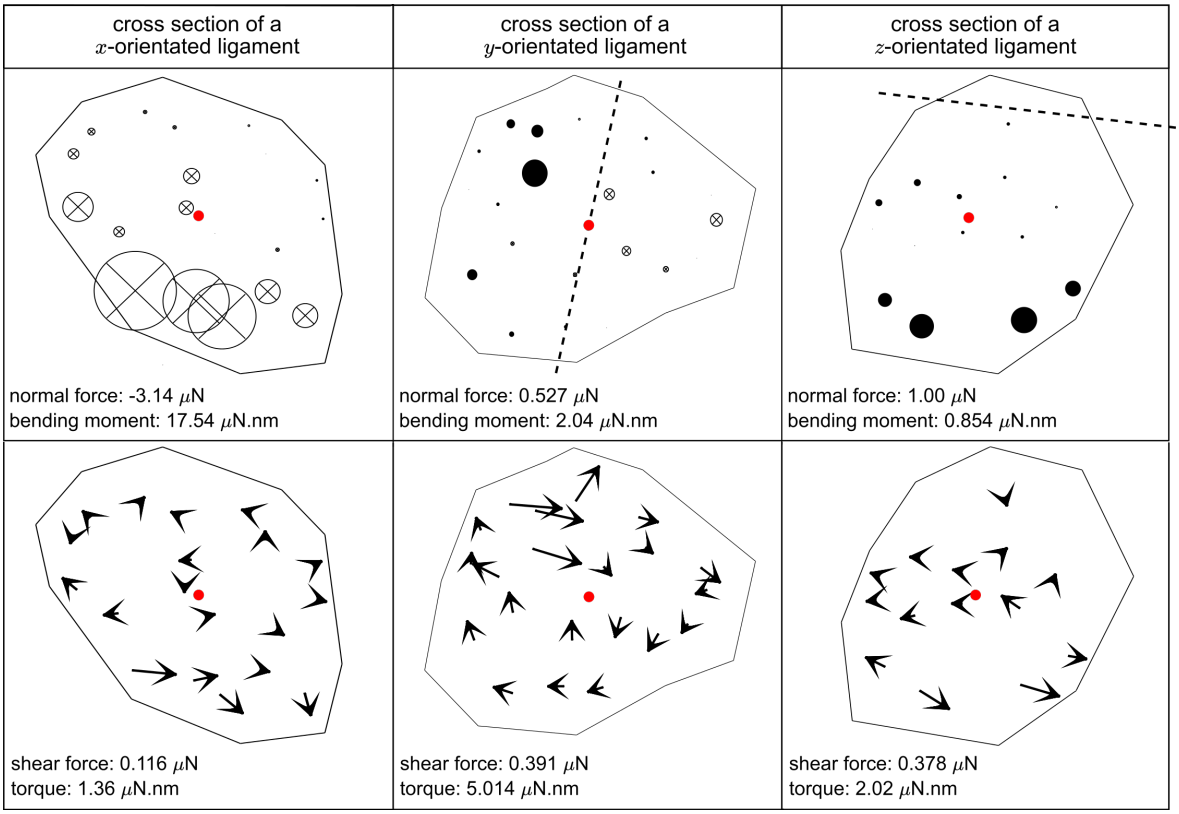

Fig. 2.13: Normal and shear stress distribution on the cross section of three ligaments with in the RVE. --- = approximate bending neutral axis of $y-$ and $z-$orientated ligaments. $\otimes$ = inward pointing normal force, $\bullet$ = outward pointing normal force calculated at each elemental centroid. The diameter of the circle or length of line represents the relative magnitude of the normal or shear force respectively. $\bullet$ = centroid of ligament cross section. [3]

was also seen in Figure 2.12. The non compression-axis aligned ligaments show a combination of forces acting both inwards and outwards with a relatively small resultant tensile normal force. The bending moment in these ligaments is also comparatively small. This suggests that the compression-axis aligned ligaments are highly load bearing. This is analogous to a fibre-reinforced composite where the strength is maximized for loading along the fibre direction and decreases away from the fibre direction. The nanocomposite is superior to this conventional composite, as it not only has ligaments in all directions providing isotropic strengthening but the interconnected nature of the ligament network further enhances its strength. However, if the nanocomposite were to be used in a simple loading scenario (uniaxial loading), by fine-tuning the microstructure to increase the number of aligned ligaments compared to non-aligned ligaments an improvement in strength could be attained.

[3] Reproduced with permission from Elsevier (https://doi.org/10.1016/j.eml.2017.09.006)

The high prevalence of normal loading in the ligaments in the nanocomposite compared to the bending dominated deformation found in nanoporous gold may be one factor that has enhanced strength and stiffness of the nanocomposite (in addition to the load distribution and load-bearing benefits of the polymer constituent).

Turning now to the shear stress distributions, there is less of a clear trend shown in the diagrams. The shear stresses generally show a circular distribution around the centroid. Those not showing this mostly point outwards from the centroid. The circular distribution results in the torque loading mode. The $y-$orientated ligament shows a very clear circular distribution of shear stresses resulting in a relatively large torque value. The effects of torsion should not be disregarded as they were shown to be important in the macroscopic mechanical response in NPG [55]. However, how a torsion loading mode influences the strength and stiffness of the nanocomposite is not well understood. There are also larger shear stresses in the non compression-axis aligned ligaments.At the locations where the largest normal forces were calculated the largest shear forces occur. The higher than expected prevalence of these shear forces (especially at the edges) is indicative of a very complex interaction at the interface between the gold and the polymer. Although the influence of delamination was not considered here it may further affect the loading modes in the nanocomposite especially with such large shear stress prevalent.

3

Fracture of nanoporous gold and its polymer filled counterpart

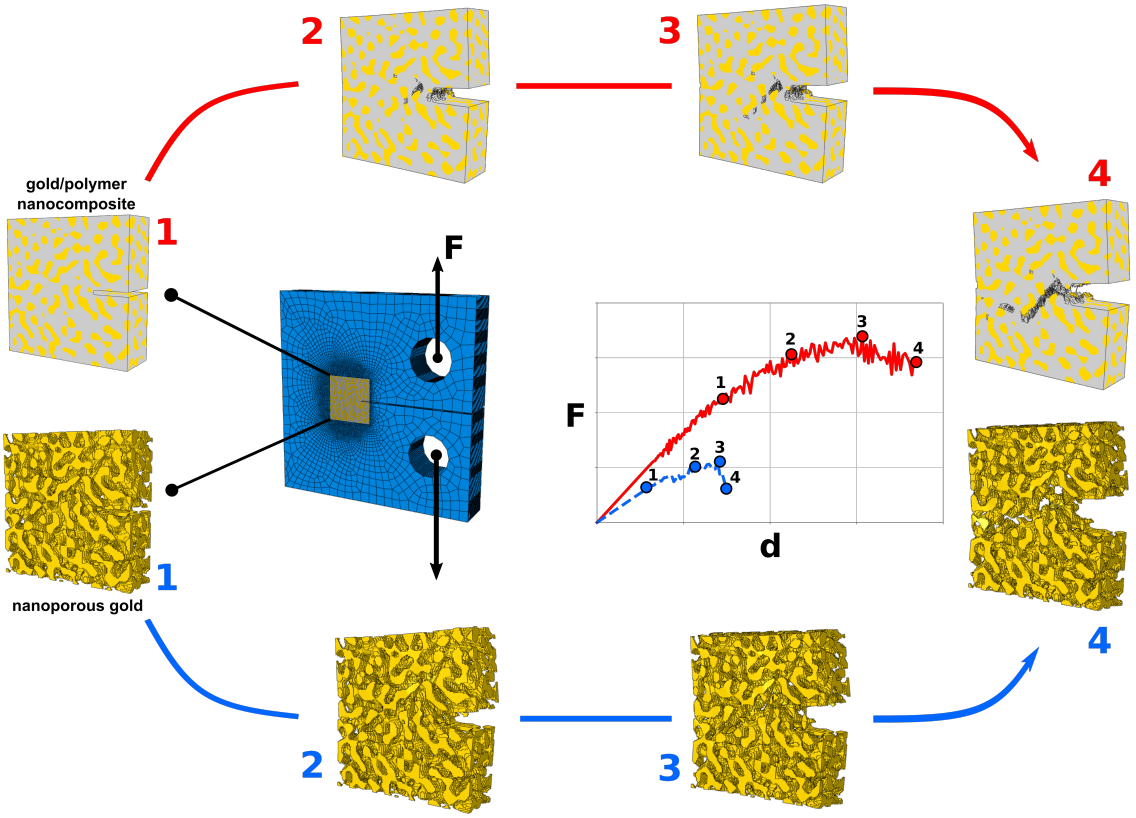

This chapter considers the initiation and propagation of cracks in nanoporous gold and its polymer filled counterpart. This is carried out using computational compact-tension tests with an embedded RVE at the crack tip of the CT specimens. The influence of the gold volume fraction on various fracture properties of these two materials is probed and the improvement in ductility of the nanoporous gold upon polymer impregnation is explored.

3.1 Introduction

Although fracture is commonly observed at the macroscopic level with the formation of large cracks, it often stems from a variety of microscopic failure mechanisms. These mechanisms can be dependent on properties such as the materials involved or their morphology and topology. Within hierarchical materials the distinct structural arrangements of the microstructure would have a significant influence on the macroscopic failure and changes at these levels can significantly alter the fracture behaviour.

Understanding how they fracture is of importance to tailor-made material creation. Investigating this experimentally, however, can be very difficult if even possible. By using computational micromechanics and performing 'virtual' fracture tests it can be done relatively quickly and extensively. Computational fracture tests allow one the ability to model the exact geometry and arrangement of the microstructure and investigate a variety of material properties and their influences on initiation and propagation of cracks. Another advantage of 'virtual' tests is the opportunity to eliminate external experimental influences. The true material behaviour can be probed whereby any external influences such as microstructural defects or the unforeseen creation of stress concentrations during machining and processing, which are often present in experimental tests, are eliminated. It also offers one the ability to observe local microfields of stress and strain.

3.2 Concepts of fracture mechanics

This section will cover some of the basic concepts in the field of fracture mechanics [109, 110] to aid the discussion of results in Section 3.5 .

3.2.1 Modes of fracture

The study of fracture mechanics typically commences by introducing a crack or notch into a specimen thereafter placing it in a state of stress. Crack initiation and propagation are then observed upon application of a load in one of three modes (Figure 3.1): Opening (Mode I), sliding (Mode II) or tearing (Mode III).

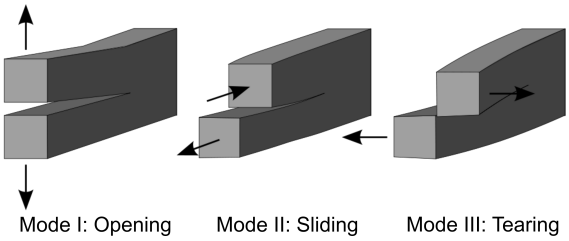

Fig. 3.1: Three loading conditions that enable crack propagation.

3.2.2 Elastic vs elastic-plastic fracture mechanics

There are two major theories within fracture mechanics in the small-strain regime: Linear Elastic Fracture Mechanics (LEFM) and Elastic-Plastic Fracture Mechanics (EPFM).

Linear Elastic Fracture Mechanics (LEFM)

The theory of linear elastic fracture mechanics, developed and extended by Alan A. Griffith [111] and George R Irwin [112] respectively, is applicable to materials that exhibit small scale yielding in the form of a very small region of non-linearity around the crack tip (red circle in Figure 3.2). That is, there is a negligible plastic region around the crack tip. This theory is thus mostly only applicable to brittle materials. Properties such as the stress intensity factor K and the strain energy release rate G are extracted; these two measures are related to each other by simple formulae. The strain energy release rate is a measure of the energy required to create new cracked surfaces upon fracture. If $K > K_{IC}$ or $G > G_{IC}$ a crack will propagate, where K_{IC} is the fracture toughness of the material and G_{IC} is the critical energy release rate.

Elastic-Plastic Fracture Mechanics (EPFM)

The theory of elastic-plastic fracture mechanics is applicable to materials where the plastic zone (created as the yield stress is exceeded in the region near the crack tip) is non-negligible (green circle in Figure 3.2). LEFM is no longer applicable in these scenarios. The common parameters for determining the fracture toughness using EPFM are the crack tip opening displacement and the J-integral. The former aims to provide a measure for the blunting of a crack tip prior to fracture and the latter is a way to calculate the strain energy release rate of material and is equal to G for a linear elastic material.

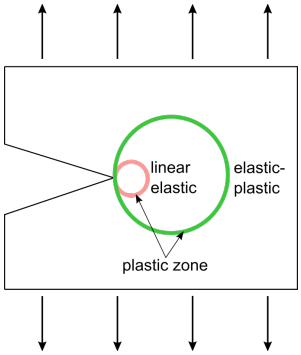

Fig. 3.2: Schematic showing the plastic regions for branches of fracture mechanics (red-LEFM, green-EPFM).

3.2.3 Fracture toughness

Fracture toughness is a measure of a material's ability to resist further fracture when a crack already exists. A ductile material will have a higher fracture toughness compared to a brittle material. A ductile failure mode (and hence high fracture toughness) is almost always more favourable than a brittle one due to the slower progression of the crack, as a ductile fracture can be identified and repaired before the material completely fails. Ductile crack progression is referred to as 'stable' as it only grows if the applied stress is increased. This is in opposition to brittle materials where failure occurs suddenly and catastrophically. Brittle materials undergo 'unstable' crack growth as the crack grows rapidly without any increase in applied stress. The quantification of the fracture toughness allows for comparisons on the extent of a materials' brittleness to be made and allows one to see how toughening mechanisms have altered its fracture toughness.

Work to fracture

An uncommon but useful measure of fracture toughness over and above those mentioned in Section 3.2.2 is that of work to fracture w_f. The work to fracture is a measure of the total external work done on a specimen and captures the components of work associated with elastic strain energy, the energy associated with the creation of new surfaces during fracture (essential work to fracture) and the energy involved in plastic deformation and other dissipative processes (non-essential work to fracture) [113, 114].

Toughening mechanisms

Ductile materials have higher fracture toughness values as the local stresses are dissipated throughout the material, thus resulting in lower stresses at the crack tip which

drive crack initiation and growth. The mechanisms that allow such dissipation, however, often also result in the low strength of these materials. In contrast, brittle materials generally have a high strength but a very low toughness. It is most desirable in applications for materials to have both high toughness and strength. Thus mechanisms to improve the toughness of brittle materials while maintaining their inherent strength are often pursued. There are generally two ways to increase the work to fracture value and hence toughness of a material: i) minimize or eliminate cracks during manufacturing, and ii) maximize the energy cost of propagating a crack, that is increase the amount of energy needed to create new crack surfaces. The former would need to be addressed during the initial processing of the material such as the creation of voids during solidification or crack formation issues during an annealing process. The latter can be addressed by promoting a variety of toughening mechanisms. There are two categories of toughening mechanisms: intrinsic and extrinsic [115]. The former occurs ahead of the crack tip and is aimed at preventing crack initiation while the latter occurs at the crack tip and aims to slow crack growth, thereby facilitating a 'stable' crack propagation.

Intrinsic toughening mechanisms

Intrinsic toughening mechanisms occur in the process zone ahead of the crack tip. These mechanisms aim to reduce the dissipative mechanisms associated with intrinsic damage processes in the materials. This is often strongly related to the plasticity of a material as the aim is to increase the plastic zone ahead of the crack tip. These mechanisms aim to alter the inherent fracture toughness of a material through improving a material's general ductility. Examples of intrinsic toughening mechanisms include the promotion of dislocation activity, sliding mechanisms and micro-cracking. It is generally very difficult to alter a materials intrinsic toughening mechanisms as it involves changing features such as bond strengths or inherent material characteristics.

Extrinsic toughening mechanisms

Extrinsic toughening mechanisms are generally associated with features present behind the advancing crack tip. These mechanisms aim at firstly reducing the local stress field at the crack tip and thereby also the crack driving force, and secondly allowing for energy to be released without advancing the crack significantly. These mechanisms (unlike intrinsic ones) are primarily associated with slowing the growth of a crack and not the initiation of crack growth. They are thus closely associated with the calculated work to fracture of a material. There is a large variety of such mechanisms, but only three common ones (shown in Figure 3.3) will be addressed here:

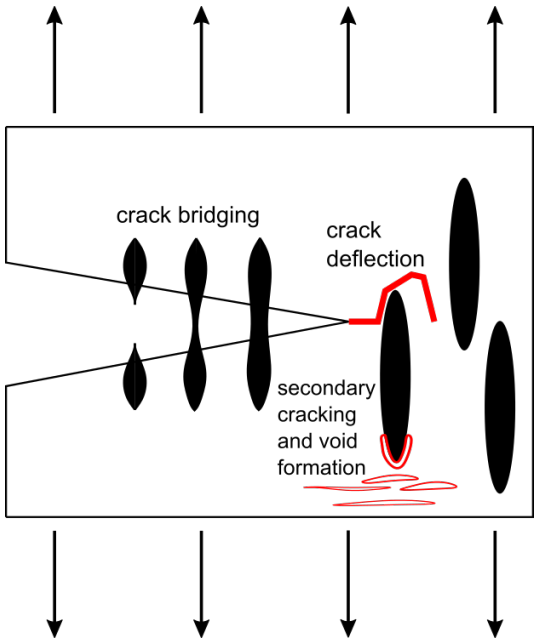

Fig. 3.3: Three common extrinsic toughening mechanisms.

Crack deflection This occurs when the crack propagates in a direction other than perpendicular to the applied load, i.e. in a straight line. This would occur when an obstacle of significantly larger strength or toughness arrests the minimum energy path of a crack, thus deflecting it. Crack deflection can also occur due to a weaker area in a direction not along the conventional crack path attracting the crack. In three dimensions the crack is also able to move laterally. Lateral crack deflection reduces the stress and hence driving force at the crack tip compared to a conventional crack by blunting the tip. Vertical and lateral crack deflection also increases the energy required for catastrophic failure as a larger cracked surface area needs to be created in order to form a crack long enough to cause complete material failure. This mechanism can be achieved through the introduction of either stronger or weaker particles or fibres into a material. It can also be achieved by orientating laminate composites in specific configurations.

Crack bridging Crack bridging occurs when load bearing links extend across the crack faces behind the crack tip. It is mostly seen in composites with a ductile constituent. The bridging element can be created, for example, by fibres perpendicular to the expected crack propagation direction. These bridging elements contribute to both a re-distribution of the stress away from the crack tip and towards the bridging elements, as well as an increase in energy dissipation as a result of de-bonding resulting in the pulling-out of fibres from the matrix or as a result of fibre elongation.

Secondary cracking and void formation Secondary cracking refers to cracking within a material that occurs at locations in the vicinity of but not at the crack tip. The intrinsic toughening mechanism whereby microvoids and cracks are purposefully created during the production of the material aims to improve the fracture toughness of a material by reproducing this effect. This cracking increases the crack area created (essential work to fracture) without advancing the crack tip and hence providing resistance to crack propagation. If the cracking occurs within or very near the fracture process zone, however, this could cause a lower crack resistance of a material. The presence of cracks also dissipates the energy away from the crack tip. This mechanism can be introduced in a variety of ways. For example in very brittle two-phase ceramics, one phase is placed in tension and the other in compression and so under tensile loading the phase already under residual tension will crack more easily and thus release energy and reduce the crack tip stress. The amount of cracking, however, needs to be limited as too much secondary cracking in the material will result in its failure before a crack emanating from the crack tip can form. The distribution of cracks or voids is also a factor that will affect the effectiveness of this mechanism. Randomly distributed cracking is far more effective than clustered cracking and many smaller cracks are preferred to fewer larger cracks.

3.2.4 Plane strain and plane stress fracture

The thickness of specimens undergoing compact-tension testing can affect whether the specimen is dominated by a state of plane stress or plane strain. When thin specimens are tested, a lack of material in the thickness direction prevents a large stress development in this direction. Thus, the specimen undergoes strain in this direction (Poisson contraction). A biaxial stress state occurs at the crack tip on the midplane and this in turn creates a larger plastic zone which results in a more ductile fracture response than may be seen in larger specimen sizes. In this case the specimen is dominated by a state of plane stress. In thicker specimens contraction at the midplane is prevented due to the constraint of the adjacent material. This gives rise to stresses in the thickness direction. The stress is zero at the free surface and reaches a maximum as one approaches the midplane. At the midplane the crack tip is now in a triaxial stress state with a small amount of strain permitted here. At the midplane a state of plane strain is now dominating. This state results in a smaller plastic zone and hence a more brittle fracture response.

Macroscopically brittle and high strength materials are more likely to show plane strain

fracture independent of specimen thickness as the material strength prevents lateral contraction even for small thicknesses. These materials are more likely to be inherently brittle at all thicknesses.

3.2.5 Randomly fused network

The randomly fused network model introduced by Arcangelis et al. [116] was used to model the breaking phenomena that occurs in disordered structures such as foams and porous materials. In this model an electrical analogue is introduced where fuses with variable probability to failure burn out as the voltage increases. This is analogous to ligaments with variable mechanical strength fracturing as the load increases and has been used to understand the brittle fracture of nanoporous gold [27]. Using this model several features of network breakages have been investigated.

Kahng et al. [117] showed that the material fracture begins with the weakest ligament failing first and the crack propagates as adjacent ligaments are then overloaded. Investigation on crack propagation showed that for a brittle network, the material catastrophically failed after a only few cracks formed and began to grow. On the contrary, for a ductile network, crack formation and growth were very gradual. Several interspersed cracks formed and catastrophic failure was due to the coalescence of these cracks. This also resulted in significantly more cracks required for the material to eventually fail.

Duxbury et al. [118] further showed that if the strength of the ligaments are all similar (i.e., the difference between the weakest and strongest ligaments is very small) once the weakest ligament fails all other ligaments are expected to fracture quickly as well thus presenting as a brittle macroscopic fracture. However, if the ligament size and thus strength have a very wide distribution it will require several ligaments to fail for the entire material to weaken so as to be unable to withstand the load. This would be representative of ductile failure mode. The macroscopic failure mode of these network systems would then be independent of the microscopic failure mode.

3.3 Finite element fracture concepts

3.3.1 Numerical crack propagation techniques

There are a variety of techniques that can be used to model fracture and crack propagation computationally. These include but are not limited to: adaptive remeshing, the

extended finite element method (XFEM), cohesive zone modelling (CZM), and element deletion (Figure 3.4).

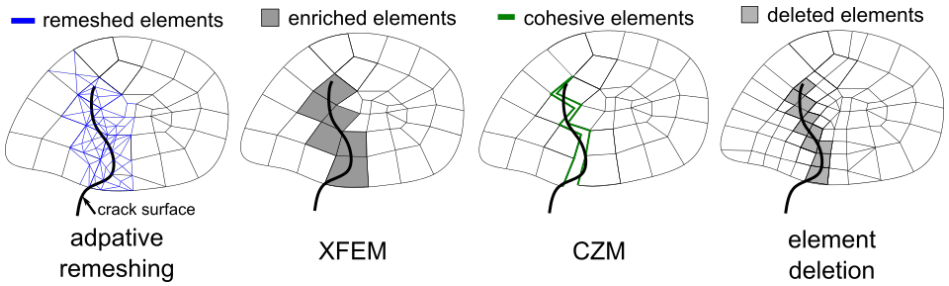

Fig. 3.4: Four common methods of numerically modelling crack propagation.

Adaptive remeshing involves deleting the mesh around a crack tip upon crack growth after which a user defined incremental crack length is applied and a new mesh is placed around the advanced crack tip [119]. XFEM, attributed to the work of Belytschko and Black [120] and Moës et al. [121], extends the classical finite element method to capture discontinuities in the solution variable (such as cracks or holes) or in the derivatives of the solution variable (such as jumps in strain). It enriches elements by including discontinuous functions within its description in order to capture crack propagation. This method requires no remeshing, making it significantly less computationally expensive than the adaptive remeshing technique.

Cohesive zone modelling models fracture by inserting line elements (in 2D models) between elements and the crack is modelled as a separation of elements along their edges. The criterion for separation is determined by a cohesive traction law at the cohesive surfaces [122, 123]. This method either requires knowledge of the crack path to be followed or the insertion of line elements throughout the model, which can result in a highly computationally expensive simulation especially in modelling complex geometries.

Element deletion is a simple technique of modelling crack propagation whereby an element is effectively removed from the simulation by setting the stiffness to zero when some deletion criterion is met at all or some of the integration points. Abaqus/Explicit has a built in method for the deletion of an element whereby an element is removed from the mesh when the critical damage limit is met at any one of the integration points. This technique requires no additional elements and is computationally inexpensive. It is favourable for use when fracture within complex geometries are to be

investigated. This technique will be used in Section 3.4 to model the crack propagation within nanoporous gold and its polymer impregnated composite.

3.3.2 Modelling the fracture of metal foams

Although the use of the FE method to investigate the fracture of nanoporous metals has not previously been done, the use of this method in modelling metal foams has been investigated. Specifically, the use of FE beam networks have often been used to model the cell walls of metallic foams. The significant reduction in computational costs motivates the use of beam elements over continuum elements. Schmidt and Fleck [124], using beam element models in conjunction with an element deletion approach, numerically investigated crack propagation within honeycomb structures. Onck et al. [125] constructed a three-dimensional model of a single ligament as found in metal foams to model their elastic, plastic and fracture behaviour. This model, consisting of beam elements, takes into account the tapered geometry and cross sectional area of the ligaments. They then used this model to investigate the sensitivity of the behaviour of metal foams to a variety of ligament parameters (geometric or otherwise).

A two-dimensional version of this single strut model was used to represent the cell walls of a metallic foam material by Mangipudi and Onck [126]. Here the sensitivity of relative density, strain hardening characteristics, cell shape and structural randomness on the damage and fracture of this material was investigated. Using the same model, Mangipudi and Onck also investigated notch sensitivity [127]. Similarly, using beam elements to model cell walls, Tankasala [128] was able to investigate four 2D lattice configurations and the effects of the relative density, extent of strain hardening and failure criterion on their ductility and ultimate tensile strength. Modelling a three-dimensional aluminium foam, Zhang et al. [129] used shell elements to model the cell walls whose thickness could easily be increased in order to assess the sensitivity of cell wall thickness and relative density on the brittle fracture behaviour.

3.4 Finite element model

To model the fracture within nanoporous gold and the polymer filled counterparts a finite element model using the element deletion technique was used. Mode I crack propagation was investigated by means of a ‘virtual’ compact-tension (CT) test which is commonly used to evaluate the fracture toughness of materials. It was selected due to

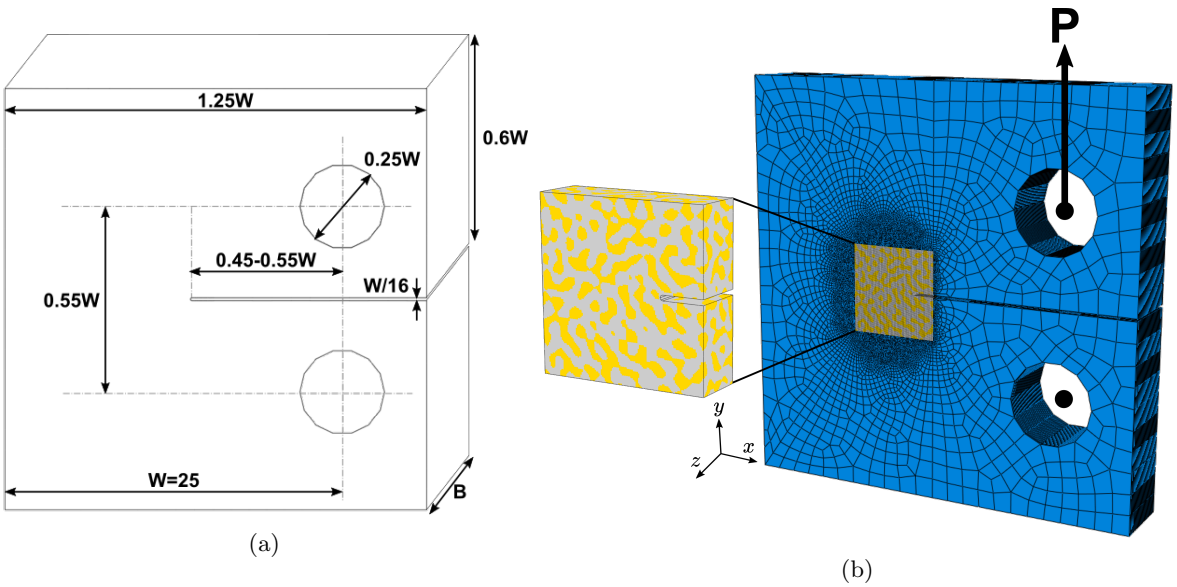

(a) (b)

Fig. 3.5: (a) Dimensions of compact-tension test specimen. (b) Compact-tension specimen making use of an embedded VE at the crack tip which models the full microstructure of nanoporous gold and the impregnated polymer. The blue region beyond the VE is modelled as an isotropic homogeneous material using effective linear elastic homogenized properties. [1]

its simple geometry and suitability to model Mode I fracture in metallic materials. The dimensions of the CT-specimen used are shown in Figure 3.5(a).

To capture the micromechanical features of crack propagation within NPG an embedded volume element (VE) located at the crack tip is used as shown in Figure 3.5(b). The VE models the fully resolved microstructure of the nanocomposite at the crack tip and within the immediate fracture region. This technique has been previously utilized by González and LLorca [130] and Canal et al. [131] to investigate the fracture of a fibre-reinforced composite material during a three-point bending test. Using this embedded VE an exact crack path can be captured within the VE region while simultaneously extracting the macroscopic load-displacement curve from the 'virtual' test. The region beyond the VE is modelled as an isotropic linear elastic homogeneous solid using homogenized effective properties.

Embedded volume element

To investigate the changes in the fracture behaviour of the composite at different gold volume fractions and thicknesses, VEs of five gold volume fractions: $\phi_M = 20, 30, 40, 50, 60\%$ (Figure 3.6(a)) and five thicknesses: $W/B = 48, 24, 16, 12$ (Figure 3.6(b)) were used. At each volume fraction and thickness three realizations were cre-

[1] Reproduced with permission from Elsevier (https://doi.org/10.1016/j.eml.2020.100815)

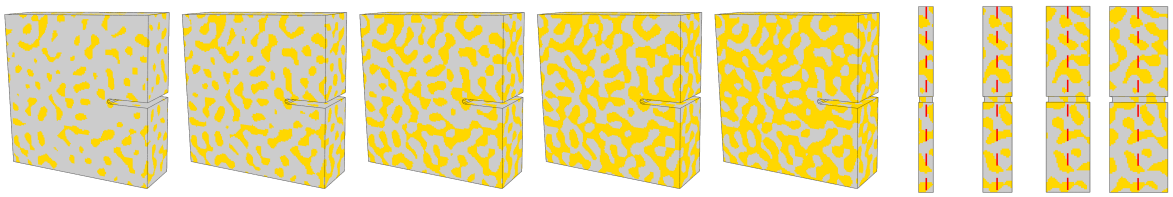

Fig. 3.6: (a) A VE section of the gold/polymer nanocomposite at each volume fraction: $20, 30, 40, 50, 60\%$ (left to right). (b) Four thicknesses of one of the realized VEs: $W/B = 48, 24, 16, 12$ (left to right). Red dashed line indicates the equivalent midplane among all VEs.

ated, representing a different stochastic network of ligaments. With the aim of keeping the topology as consistent as possible, each realization was initially created at the lowest volume fractions, after which the volume fraction of gold was increased by increasing the ligament size. The VEs generated have elastomechanically representative lengths and widths [83] whereas the thickness is varied to investigate plane strain-plane stress effects.

Each VE is modelled using a voxel mesh with equal sized voxels, so that the different thickness can also be characterized by their voxel thickness. Each VE at each thickness was created starting at the same midplane (red dashed line in Figure 3.6(b)) and selecting an equal number of voxel on either side necessary to create the required thicknesses. To compare the behaviour of the pure NPG with the nanocomposite, NPG VEs were created from the nanocomposite by removing the polymer material. This ensures consistent topology of the metal phase between the nanocomposite and the nanoporous gold VEs. NPG VEs were created at four volume fractions ($\phi_M = 30, 40, 50, 60\%$) and only one thickness ($W/B = 12$).

3.4.1 Boundary conditions

The boundary conditions are applied to simulate a macroscopic CT test. Two reference nodes (depicted as black circles in Figure 3.5(b)) are created and kinematically constrained to nodes located on the surface of the surrounding circle. Kinematically constrained nodes simulate the rigid body motion of these nodes, thereby simulating a rigid pin inserted into these circles. Both reference nodes are free to rotate about the $z-$axis and the upper node is allowed to translate vertically in the $y-$direction. All other degrees of freedom are constrained at the reference nodes. Zero traction boundary conditions are applied to all other boundaries of the model.

3.4.2 Material behaviour

Fundamental kinematics

In this chapter we use a multiplicative decomposition [2] of the deformation gradient into an elastic $\boldsymbol{F}^{\mathrm{e}}$ and plastic part $\boldsymbol{F}^{\mathrm{p}}$ such that

$$\boldsymbol{F} = \boldsymbol{F}^{\mathrm{e}}\boldsymbol{F}^{\mathrm{p}} \,. \tag{3.1}$$

This leads to a definition of the elastic right Cauchy-Green deformation tensor and elastic Green-Lagrange strain tensor given by

$$\boldsymbol{C}^{\mathrm{e}} = \left[\boldsymbol{F}^{\mathrm{e}}\right]^{\mathrm{T}} \boldsymbol{F}^{\mathrm{e}} \quad \text{and} \quad \boldsymbol{E}^{\mathrm{e}} = \frac{1}{2}\left[\boldsymbol{C}^{\mathrm{e}} - \boldsymbol{I}\right] \,, \tag{3.2}$$

respectively.
The elastic left Cauchy-Green deformation tensor is given as

$$\boldsymbol{B}^{\mathrm{e}} = \boldsymbol{F}^{\mathrm{e}}\left[\boldsymbol{F}^{\mathrm{e}}\right]^{\mathrm{T}} \,. \tag{3.3}$$

Using this, the effective plastic distortional stretch λ^{p} is given as

$$\lambda^{\mathrm{p}} = \sqrt{\frac{\mathrm{tr}\boldsymbol{B}^{\mathrm{p}}}{3}} \,, \tag{3.4}$$

where $\boldsymbol{B}^{\mathrm{p}} = \boldsymbol{F}^{\mathrm{p}}\left[\boldsymbol{F}^{\mathrm{p}}\right]^{\mathrm{T}}$ is the plastic left Cauchy-green deformation tensor.
With the material time derivative of the deformation gradient given as

$$\dot{\boldsymbol{F}} = \boldsymbol{L}\boldsymbol{F} \,, \tag{3.5}$$

where $\boldsymbol{L} = \dfrac{\partial \boldsymbol{v}}{\partial \boldsymbol{x}}$ is the spatial velocity gradient, the plastic rate of deformation tensor is of the form

$$\boldsymbol{D}^{\mathrm{p}} = \frac{1}{2}\left[\dot{\boldsymbol{F}}^{\mathrm{p}}\left[\dot{\boldsymbol{F}}^{\mathrm{p}}\right]^{-1}\right] \tag{3.6}$$

Assuming both the polymer and gold material undergo isochoric plastic deformation, the condition $\mathrm{tr}\,\boldsymbol{D}^{\mathrm{p}} = 0$ is imposed.

The material behaviour of each constituent within the gold/polymer nanocomposite located within the embedded VE is described through the following constitutive relations.

[2] This was first introduced in the context of finite plasticity in the work of Bilby et al. [132] although it is often termed the Kröner and Lee decomposition [133–135]

Polymer

The polymer used here is an epoxy resin. Epoxy is classified as an amorphous glassy polymer which is both temperature- and time-dependent. Compared to other polymers, epoxies have excellent mechanical strength (in both tension and compression) and are commonly used in the aerospace industry. It is also a commonly used matrix material within composites. The stress-strain response of this ductile polymer is highly non-linear, as can be seen in Figure 3.7.

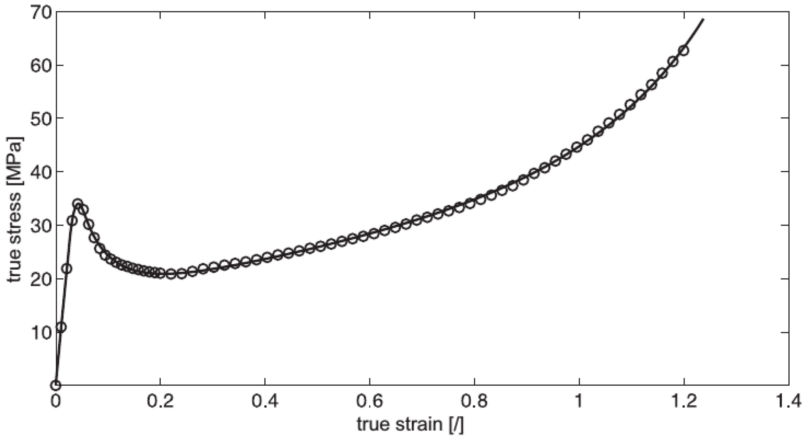

Fig. 3.7: Stress strain response of an epoxy resin during a compression test displaying an elastic-viscoplastic response. Taken from [50].

The behaviour is characterized as elastic-viscoplastic, which exhibits an initial isotropic elastic region up to a yield point. After a period of post-yield strain softening a network hardening mechanism occurs, resulting in strain hardening. The constitutive theory used here is a macroscopic theory for the deformation of an epoxy resin under isothermal conditions above the glass transition temperature (these polymers show a brittle response below this temperature). The theory was developed by [136, 137] and later used by Bargmann et al. [50] in their work on modelling gold-polymer nanocomposites. The details of the constitutive relations for this model are given below.

In order to fully define the behaviour of this material expressions for the elastic and plastic stress need to be formulated. In addition to this a flow rule and evolution equations for internal state variables need to be described. The elastic and plastic stress expressions are formulated from a Helmholtz free energy function Ψ. Here, it is additively decomposed into elastic Ψ^{e} and plastic parts Ψ^{p}

$$\Psi = \Psi^{\mathrm{e}}(\boldsymbol{E}^{\mathrm{e}}) + \Psi^{\mathrm{p}}(\lambda^{\mathrm{p}}). \tag{3.7}$$

The elastic part is defined as

$$\Psi^{\mathrm{e}} = \frac{1}{2}\kappa \mathrm{tr}(\boldsymbol{E}^{\mathrm{e}})^2 + \mu \mathrm{dev}(\boldsymbol{E}^{\mathrm{e}}) : \mathrm{dev}(\boldsymbol{E}^{\mathrm{e}}) \,, \tag{3.8}$$

where κ and μ are the bulk modulus and shear modulus respectively and $\mathrm{dev}(\cdot)$ refers to the deviatoric tensor of $(\cdot)$. From this the rotated Cauchy stress $\boldsymbol{\sigma}^{\mathrm{e}}$, where $\boldsymbol{\sigma}^{\mathrm{e}} = [\boldsymbol{R}^{\mathrm{e}}]^{\mathrm{T}} \boldsymbol{\sigma} \boldsymbol{R}^{\mathrm{e}}$, is given by

$$\boldsymbol{\sigma}^{\mathrm{e}} = \frac{\partial \Psi^{\mathrm{e}}}{\partial \boldsymbol{E}^{\mathrm{e}}} = \kappa \, \mathrm{tr}(\boldsymbol{E}^{\mathrm{e}}) \mathbf{1} + 2\mu \, \mathrm{dev} \, \boldsymbol{E}^{\mathrm{e}} \,. \tag{3.9}$$

The plastic part Ψ^{p} is formulated in terms of the effective distortional plastic stretch introduced in (3.4). The plastic part is of the form

$$\Psi^{\mathrm{p}} = \mu_R \lambda_L^2 \left[\frac{\lambda^p}{\lambda_L} x + \log\left(\frac{x}{\sinh x}\right) - \frac{1}{\lambda_L} y - \log\left(\frac{y}{\sinh y}\right) \right], \tag{3.10}$$

with

$$x = \Gamma^{-1}\left(\frac{\lambda^{\mathrm{p}}}{\lambda_{\mathrm{L}}}\right) \quad \text{and} \quad y = \Gamma^{-1}\left(\frac{1}{\lambda_{\mathrm{L}}}\right) . \tag{3.11}$$

Here, μ_{R} and λ_{L} are material parameters called the rubbery modulus and network locking stretch, respectively. Γ^{-1} is the inverse of the Langevin function $\Gamma(z) = \coth(z) - 1/z$.

As seen in Figure 3.7 there is a Bauschinger-type reverse-yielding upon unloading. This results from the development of back stress. A back stress $\boldsymbol{S}^{\mathrm{back}}$ that accounts for this after large plastic deformations and also the rapid strain-hardening response after the softening region is given by

$$\boldsymbol{S}^{\mathrm{back}} = 2\mathrm{dev}\left(\mathrm{sym}\left(\frac{\partial \Psi^{\mathrm{p}}}{\partial \boldsymbol{B}^{\mathrm{p}}} \cdot \boldsymbol{B}^{\mathrm{p}}\right)\right) = \mu^{\mathrm{back}} \mathrm{dev} \boldsymbol{B}^{\mathrm{p}} \,, \tag{3.12}$$

where μ^{back}, the back stress modulus, is given by

$$\mu^{\mathrm{back}} = \frac{1}{3\lambda^{\mathrm{p}}} \frac{\partial \Psi^{\mathrm{p}}}{\partial \lambda^{\mathrm{p}}} = \mu_{\mathrm{R}} \frac{\lambda_{\mathrm{L}}}{3\lambda^{\mathrm{p}}} \Gamma^{-1}\left(\frac{\lambda^{\mathrm{p}}}{\lambda_{\mathrm{L}}}\right) . \tag{3.13}$$

It is noted that since $\Gamma^{-1}(z) \to \infty$ as $z \to 1$, $\mu^{\mathrm{back}} \to \infty$ as $\lambda^{\mathrm{p}} \to \lambda_{\mathrm{L}}$.

An associative flow rule for large deformation plasticity using the plastic rate of deformation tensor is adopted, for which case

$$\boldsymbol{D}^{\mathrm{p}} = \nu^{\mathrm{p}} \left[\frac{\operatorname{dev} \boldsymbol{\sigma}^{\mathrm{e}} - \boldsymbol{S}^{\mathrm{back}}}{2\bar{\tau}} \right] . \tag{3.14}$$

Here the equivalent plastic shear strain rate ν^{p} is given by

$$\nu^{\mathrm{p}} = \nu_0 \left[\frac{\bar{\tau}}{s - \alpha/3 \operatorname{tr} \boldsymbol{\sigma}^{\mathrm{e}}} \right]^{1/n} \quad , \quad 0 < n \leq 1 \quad \text{and} \quad s - \frac{\alpha}{3} \mathrm{tr}(\boldsymbol{\sigma}^{\mathrm{e}}) > 0 \, ; \tag{3.15}$$

ν_0 is the the reference plastic shear strain rate and α and n are pressure and strain rate sensitivity material parameters. The case $n \to 0$ corresponds to the rate-independent formulation while $n \to 1$ corresponds to linear viscosity. The equivalent shear stress $\bar{\tau}$ is defined by

$$\bar{\tau} = \sqrt{\frac{1}{2} [\operatorname{dev} \boldsymbol{\sigma}^{\mathrm{e}} - \boldsymbol{S}^{\mathrm{back}}] : [\operatorname{dev} \boldsymbol{\sigma}^{\mathrm{e}} - \boldsymbol{S}^{\mathrm{back}}]}. \tag{3.16}$$

The internal state variable s in (3.15) describes the isotropic resistance to plastic flow which increases from some initial value s_0 to a peak saturation value $\tilde{s}$ and then decreases to some equilibrium value s^{cv}. The saturation value of s is defined by

$$\tilde{s} = s^{\mathrm{cv}} \left[1 + b[\eta^{\mathrm{cv}} - \eta] \right] . \tag{3.17}$$

Here, a second internal state variable η which describes the local free volume is introduced. The local free volume is commonly believed to cause the non-linear stress-strain behaviour before the yield-peak and the softening that follows in Figure 3.7. The free volume increases with loading from 0 to some equilibrium value η^{cv}.

The evolution of the two internal state variables is given by

$$\dot{s} = \nu^{\mathrm{p}} h_0 \left[1 - \frac{s}{\tilde{s}\,(\eta)} \right] \quad \text{and} \quad \dot{\eta} = \nu^{\mathrm{p}} g_0 \left[\frac{s}{s^{\mathrm{cv}}} - 1 \right] , \tag{3.18}$$

This ensures that $\dot{s}$ is positive below saturation and negative when s is above the saturation value.

The above equations give rise to 11 material parameters: $\{\mu_R, \lambda_L, \nu_0, \alpha, n, s_0, s^{\mathrm{cv}}, \eta^{\mathrm{cv}}, b, h_0, g_0\}$. The values identified by Bargmann et al. [50] were used and are given in Table 3.1. Moreover, values of Young's modulus of $E = 1.038$ GPa and Poisson's ratio of $\nu = 0.35$ were selected [5]. Failure within the epoxy material is assumed to occur when the effective plastic stretch at a material point reaches a critical value $\lambda^{\mathrm{p,cri}} = 1.192$ [137,138].

Table 3.1: Elastic-viscoplastic material parameters identified in [50] for the epoxy resin constituent.

Parameter	Symbol	Value	Dimension
Rubbery modulus	μ_{R}	5.2384	[MPa]
Network locking stretch	λ_{L}	1.67	[−]
Reference plastic shear-strain rate	ν_0	0.0017	[s^{-1}]
Pressure sensitivity parameter	α	0.204	[−]
Rate sensitivity parameter	n	0.043	[−]
Initial resistance to plastic flow	s_0	18.033	[MPa]
Equilibrium value for s	s^{cv}	8.621	[MPa]
Equilibrium value for η	η^{cv}	0.000773	[−]
Parameter for $\tilde{s}$	b	1750.2	[−]
Rate controlling parameter for s	h_0	2147.8	[MPa]
Rate controlling parameter for η	g_0	0.004519	[−]
Critical effective plastic stretch	$\lambda^{\mathrm{p,cri}}$	1.192	[−]

Gold

The gold material is modelled as elastic-plastic-damage: in particular linear isotropic elastic, isotropic J_2 plasticity and a coupled isotropic Lemaitre damage model. A brief overview of these material models is given here.

In a specimen undergoing a uniaxial tensile test, cracks and voids appear within the material. At these locations the material no longer provides strength against the load imposed on it. If these defects are removed, a fictional effective area contributing to the development of an effective stress within the material can be considered [139]. Lemaitre damage, a commonly used damage material model, introduces the concept of a damage variable D to represent the ratio of the area damaged by these cracks or voids to the total original area. If $D = 0$ there is no damage present, if $D = 1$ the material has fully ruptured (the total original area is damaged by crack or voids). Between these two values D gives a quantification of the damaged state of the material. In practice, the material will weaken and fail before the entire area is damaged, thus a material parameter D^{cri} is introduced as the critical threshold at which the material fails [140,141].

The effective stress measure $\tilde{\boldsymbol{\sigma}}^{\mathrm{e}}$ is scaled by the damage variable such that

$$\tilde{\boldsymbol{\sigma}}^{\mathrm{e}} = \frac{\boldsymbol{\sigma}^{\mathrm{e}}}{1 - D}\,, \tag{3.19}$$

The effects of damage on the strain field are considered to be modified due to the inclusion of damage in defining the effective stress. Within the elastic region of deformation,

linear isotropic elasticity relates the scaled stress and strain such that

$$\boldsymbol{\sigma}^{\mathrm{e}} = \kappa \mathrm{tr}(\boldsymbol{E}) + 2\mu \mathrm{dev}(\boldsymbol{E}) \,, \tag{3.20}$$

where κ is the bulk modulus and μ is the shear modulus.

Plastic behaviour is governed by J_2 plasticity with an isotropic hardening rule. Plastic flow is initiated when the von Mises stress,

$$\tilde{\tau^e} = \sqrt{\frac{3}{2}\left(\tilde{\boldsymbol{\sigma}}^{\mathrm{e}} : \tilde{\boldsymbol{\sigma}}^{\mathrm{e}} - \frac{1}{3}(\mathrm{tr}\tilde{\boldsymbol{\sigma}}^{\mathrm{e}})^2\right)} \,, \tag{3.21}$$

equals the yield stress τ_y. Thereafter, hardening occurs within the material and the yield surface, defined by $f(\tilde{\boldsymbol{\sigma}}, \alpha^{\mathrm{p}}) = \tilde{\tau}^e - \tau_y \leq 0$, develops such that

$$\tau_y = \tau_0 + q(\alpha^{\mathrm{p}}) \tag{3.22}$$

where τ_0 is the initial yield stress. $q(\alpha^{\mathrm{p}})$ defines the hardening in terms of the equivalent plastic strain α^{p}. The hardening rule used is a combination of linear and saturation type hardening and is given by

$$q = [\tau_\infty - \tau_0]\left[1 - e^{-\delta\alpha^{\mathrm{p}}}\right] . \tag{3.23}$$

Here τ_∞ and δ are material parameters.

The associative flow rule for this material is given by

$$\boldsymbol{D}^{\mathrm{p}} = \dot{\alpha}^{\mathrm{p}} \frac{\partial f}{\partial \tilde{\boldsymbol{\sigma}}^{\mathrm{e}}}, \tag{3.24}$$

where $\dfrac{\partial f}{\partial \tilde{\boldsymbol{\sigma}}^{\mathrm{e}}} = \dfrac{3}{2}\dfrac{\tilde{\boldsymbol{\sigma}}^{\mathrm{e}} - \frac{1}{3}\mathrm{tr}\tilde{\boldsymbol{\sigma}}^{\mathrm{e}}}{\tilde{\tau}^e}$.

Finally, the inclusion of the damage variable requires the introduction of the damage evolution law as follows

$$\dot{D} = \dot{\alpha}^{\mathrm{p}} \frac{Y}{S}, \tag{3.25}$$

Here S is a material parameter and Y is the thermodynamically formal damage conjugate variable given by [142]

$$
\begin{aligned}
Y = \frac{1}{4\mu}\left[\left[\langle\tilde{\sigma}_1^{\mathrm{e}}\rangle^2 + \langle\tilde{\sigma}_2^{\mathrm{e}}\rangle^2 + \langle\tilde{\sigma}_3^{\mathrm{e}}\rangle^2\right] + \left[\frac{2\mu}{\kappa} - 3\right]\langle \mathrm{tr}\,\tilde{\boldsymbol{\sigma}}^{\mathrm{e}}/3\rangle^2\right] \\
+ \frac{h}{4\mu}\left[\left[\langle -\tilde{\sigma}_1^{\mathrm{e}}\rangle^2 + \langle -\tilde{\sigma}_2^{\mathrm{e}}\rangle^2 + \langle -\tilde{\sigma}_3^{\mathrm{e}}\rangle^2\right] + \left[\frac{2\mu}{\kappa} - 3\right]\langle -\mathrm{tr}\,\tilde{\boldsymbol{\sigma}}^{\mathrm{e}}/3\rangle^2\right] .
\end{aligned}
\tag{3.26}
$$

Here $\langle\cdot\rangle$ denotes the Macauley bracket such that $\langle x\rangle := \frac{1}{2}(x+|x|)$ and $\tilde{\sigma}_{\mathrm{A}}^{\mathrm{e}},\ A = (1,2,3)$ are the principle stresses of $\boldsymbol{\sigma}^{\mathrm{e}}$. A quasi-unilateral damage evolution parameter $h \in [0,1]$ acts as a weighting factor. This factor scales the energetic contribution of the compressive principal stresses and the hydrostatic stress [140, 143, 144].

At the nanoscale, continuum models are known to have limited use as they do not take into account dislocation activity. It would be most suitable to use a crystal plasticity based constitutive for the gold which models the generation and interactions of dislocations. These dislocations contribute to the "smaller is stronger" yield stress relationship exhibited by the gold material. Although the gold constitutive model here does not take these mechanisms into account, the use of this kind of phenomenological continuum model has previously provided insights into the deformation of the material while greatly reducing the computational expense [71, 78]. This reduced computational complexity allows one to use the more complex and realistic material geometry. Additionally, as the ligament sizes are relatively the same across all specimens, comparative conclusions can still be drawn when using these continuum material models. Furthermore, size effects due to surface elasticity have been shown to emerge only at diameters below 10 nm [59, 145].

The above constitutive model gives rise to 6 material parameters: $\{\tau_0, \tau_\infty, \delta, S, h, D^{cri}\}$. The experimental results of uniaxial tensile tests of Emery and Povick on 250 nm thick fine-grained gold films were used to determine $\tau_0, \tau_\infty, \delta, S$ and h. These values are given in Table 3.2. The Young's modulus $E = 79$ GPa and Poisson's ratio $\nu = 0.44$ were taken from those of bulk gold [25, 27, 146].

Table 3.2: Damage and material parameters identified for the gold constituent.

Parameter	Symbol	Value	Dimension
Initial yield stress	τ_0	155	[MPa]
Isotropic hardening saturation stress	τ_∞	405	[MPa]
Isotropic hardening exponent	δ	625	[−]
Damage rate scaling parameter	S	1	[MPa]
Quasi-unilateral damage evolution parameter	h	0	[−]
Critical damage	D^{cri}	0.011	[−]

To determine D^{cri}, a RVE of nanoporous gold with elastoplastic representative dimensions [83] and a volume fraction of 30% was simulated under three tensile tests, along each orthogonal direction. The tensile test was simulated using kinematic uniform (prescribed displacement) boundary conditions as discussed in Chapter 2. The fracture strain was taken at the point of ultimate fracture stress due to the known brittleness of nanoporous gold. The stress strain plots for each simulated tensile test are shown in Figure 3.8 with inserts showing the displacement field in the direction of the test applied. The sudden brittle nature of nanoporous gold fracture is evident here.

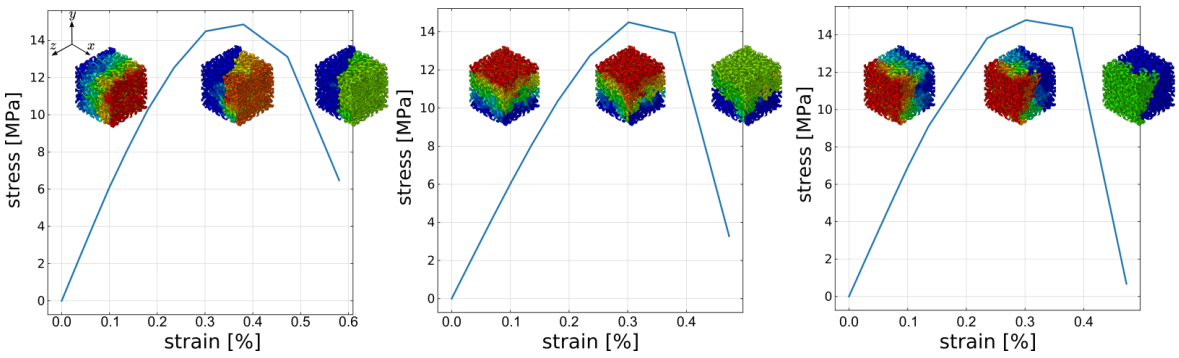

Fig. 3.8: Stress-strain plots of a RVE of nanoporous gold under uniaxial tensile testing in three orthogonal directions. Inserts show the displacement field in the direction of the tensile test at various points where blue indicates no displacement and red indicates the maximum displacement.

Using $D^{cri} = 0.011$ the ultimate stress and fracture strains given by each tensile test given in Table 3.3 were determined. There is a wide range of ultimate stresses ($9 - 98$ MPa) and fracture strains ($0.22 - 7.3\%$) in the experimental literature on nanoporous gold under tensile loading using a similar gold volume fraction. The larger ultimate stresses of $87 - 98$ MPa and strains of $6.2 - 7.3\%$ were recorded by Xia et al. [38] using nanoporous gold samples with very small ligament diameters ($10 - 11$ nm). Molecular

Table 3.3: Ultimate stress and fracture strains of a 30% gold volume fraction nanoporous gold RVE under uniaxial tensile loading.

Tensile direction	Ultimate tensile strength [MPa]	Fracture strain [%]
x	14.85	0.38
y	14.50	0.38
z	14.79	0.38
Average	14.71	0.38

dynamic simulations using samples with ligament diameters of similar sizes also produced significantly larger stress and strain values and so these results as well as those of [38] are not considered here. As mentioned in Section 1.2.1, these numerical results have also not been validated by experiments. The results of Balk et al. [27], Briot et al. [28], Sun et al. [29] and Badwe et al. [30] with samples of ligament diameters greater than 20 nm and up to 700 nm are all somewhat in agreement with an ultimate stress range of $10 - 25$ MPa and fracture strain range of $0.35 - 0.7\%$. This narrower range was used to select the appropriate critical damage threshold.

The material behaviour of the interfaces between constituents is often also modelled in order to capture delamination between the two. Modelling this interface would be prohibitively computationally expensive when combined with the complex topographical and morphological features and thus is not accounted for here.

Homogeneous region

The homogeneous region of the CT specimen (blue region in Figure 3.5(b)) is modelled as an isotropic linear elastic material. Thus the material response can be fully defined using two effective elastic constants, Young's modulus $E^\star$ and Poisson's ratio $\nu^\star$.

The effective Young's modulus of nanoporous gold at volume fractions less than 50% is calculated from the relation given in [83]:

$$\frac{E^\star}{E_M} = 2.03 \left[\frac{\phi_M - \phi_M^p}{1 - \phi_M^p} \right]^{2.56}, \tag{3.27}$$

where E_M is the Young's modulus of the metal (i.e., gold in this case). $\phi_M^p = 0.159$ [83] is the percolation threshold and defined as the minimum volume fraction that can be achieved while still maintaining a continuous ligament network. Soyarslan et al. [83] recognized that above a volume fraction of 50%, this relation no longer holds and so the classical Gibson-Ashby scaling law for open cell porous metal foams is adopted [61,147]:

$$\frac{E^\star}{E_M} = \phi_M^2. \tag{3.28}$$

The effective Poisson's ratio is determined from the empirically determined relation [83]:

$$\nu^\star = 0.262 \log \phi_M + 0.365. \tag{3.29}$$

The effective elastic property relations for the gold/polymer nanocomposite are significantly different from that of the nanoporous gold. Carolan et al. [148] proposed an adaptation to the Gibson-Ashby scaling law given by (3.28) to account for a second continuous phase:

$$E^\star = E_P + (E_M - E_P)\phi_M^2, \tag{3.30}$$

where E_P is the Young's modulus of the polymer phase. The relation was then specifically calibrated for the gold/polymer nanocomposite by [70] to give

$$E^\star = E_P + (E_M - E_P)\phi_M^{2.45}. \tag{3.31}$$

This relation is used for all volume fractions of the nanocomposite.

The effective Poisson's ratio was found to be constant $\nu = 0.3$ at all volume fractions for the nanocomposite [70].

3.5 Results and discussion

The simulations of all micro-specimens were performed in Abaqus/Explicit using the inbuilt element deletion functionality. The material models described in Section 3.4.2 were implemented using Vumat subroutines written by Celal Soyarslan of Wuppertal University, Germany. To allow for appropriate computational times mass scaling was necessary. The inertial effects were minimized by applying the displacement slowly and as a smooth function. Load-displacement curves were created for all specimens for each realization. It was noted that the results for the three samples at each volume fraction were very similar; thus, it is only necessary to show the results of one sample per volume fraction. The results given in the following are for only the thickest specimens, except in Section 3.5.4.

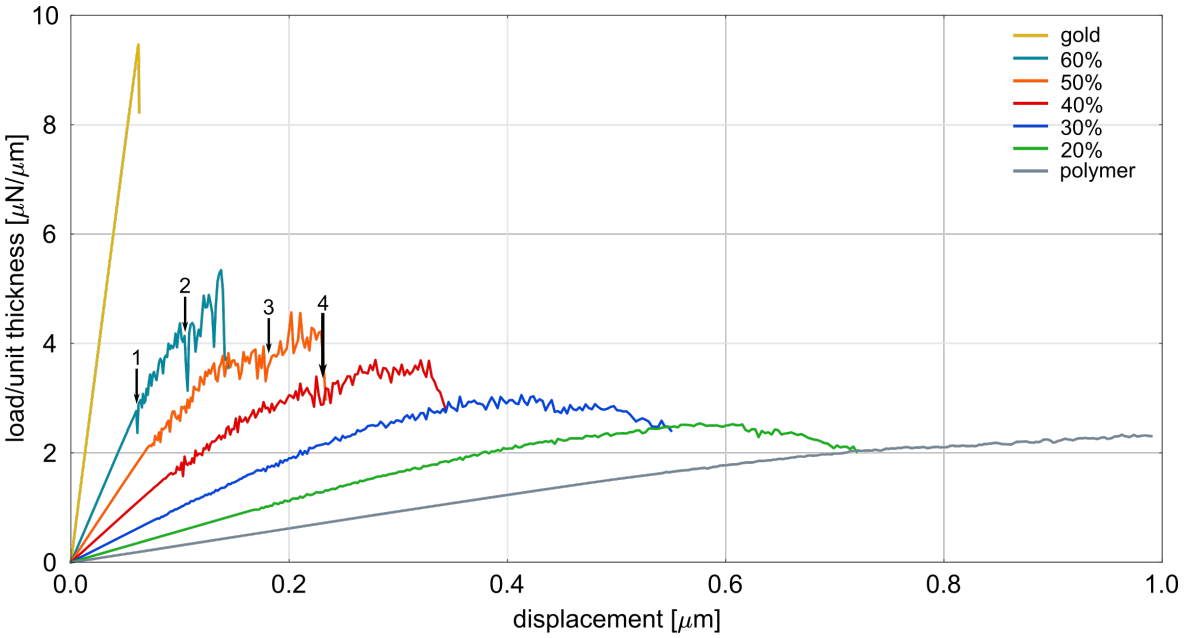

Fig. 3.9: Load-displacement curves of the nanocomposite material with different volume fractions of gold. The curves of a pure polymer and pure gold material are also given. With increasing volume fraction of gold the decreasing ductility shown by smaller displacements at fracture and the increasing strength shown by higher load/unit thickness values is evident. [3]

3.5.1 Fracture within gold/polymer nanocomposite

The load-displacement curves for the nanocomposite at the five different volume fractions are shown in Figure 3.9. Specimens of bulk polymer and bulk gold were also simulated to allow for comparisons to be made. The gold specimen displays a brittle fracture response with the fracture preceded only by a straight line which is representative of a pure linear elastic response and no plastic deformation before fracture. The polymer shows a representative elastic-plastic response, with no clear fracture point. As expected, the curves of the nanocomposite lie between the two bulk constituent curves. At lower gold volume fractions, between 20 and 40%, the material shows an elastic-plastic response where as in the higher volume fraction samples the elastic-plastic region of deformation becomes less obvious and the material moves towards a linear elastic fracture mechanism.

One of the main features shown in Figure 3.9 is that with an increase in the gold volume fraction the displacement at fracture decreases and the maximum load increases. The former reveals a decrease in ductility while the latter reveals the associated increase in strength that often accompanies a loss in ductility.

[3] Reproduced with permission from Elsevier (https://doi.org/10.1016/j.eml.2020.100815)

The volume fraction of polymer and the volume fraction of the gold directly contribute to these features. The polymer is a low load carrying capacity material; however it is extremely ductile and so can undergo significant displacement. The gold material is very strong but very brittle and so can withstand a large load but only at very small displacements. As with most composites, as the volume fraction of each constituent increases or decreases the prevalence of the mechanical properties of each constituent also increases or decreases respectively. That is, at low volume fractions of gold the ductility of the polymer is more obvious while the high strength of the gold is less so. Another feature contributing to the differing responses is the interconnectivity of the constituents. As the gold volume fraction increases, the interconnectivity of the gold ligament network increases and the interconnectivity of the polymer decreases. At the lowest gold volume fraction the gold network connectivity is relatively weak, additionally there is a small amount of this reinforcing material and thus the polymer material has to provide the majority of the support, thus resulting in the low load capacity at lower volume fractions. However, with a weaker connectivity the network is far less constrained against deformation and so a small amount of localized deformation of the gold network can occur without this deformation transferring over the gold network to other locations. This was similarly suggested by Beets et al. [40] with regards to pure NPG. On the other hand, at higher gold volume fractions there is a high degree of connectivity and so localized displacement of the network results in significant displacement throughout the sample.

A unique feature in the load-displacement curves of, particularly, the higher volume fraction specimens are their jagged nature. The sudden drops are associated with brittle ligament breakages occurring in the gold ligament network and the rise that follows is an indicator that the load has been re-distributed to adjacent ligaments. As ligaments break, the network weakens and the polymer is required to carry more of the load. The repetitive failure of ligaments continues until a critical number of ligaments have failed which weakens the gold ligament network to a point where the load transferred to the polymer is in excess of what it can withstand. Thus a crack propagates through the polymer network and the nanocomposite fails catastrophically. Times of notably large ligament fracture are marked $1-4$ on Figure 3.9. Figure 3.10(a) shows an example of the fracture of a gold ligament, which causes the drop at marker 1 in Figure 3.9. The resultant re-distribution of the stress within the gold and polymer networks is also shown in Figures 3.10(b) and 3.10(c) respectively where locations of significant stress re-distribution are encircled. The stress within the gold is transferred to locations relatively far from the crack tip while the polymer shows a stress increase at the location

where the gold fractured.

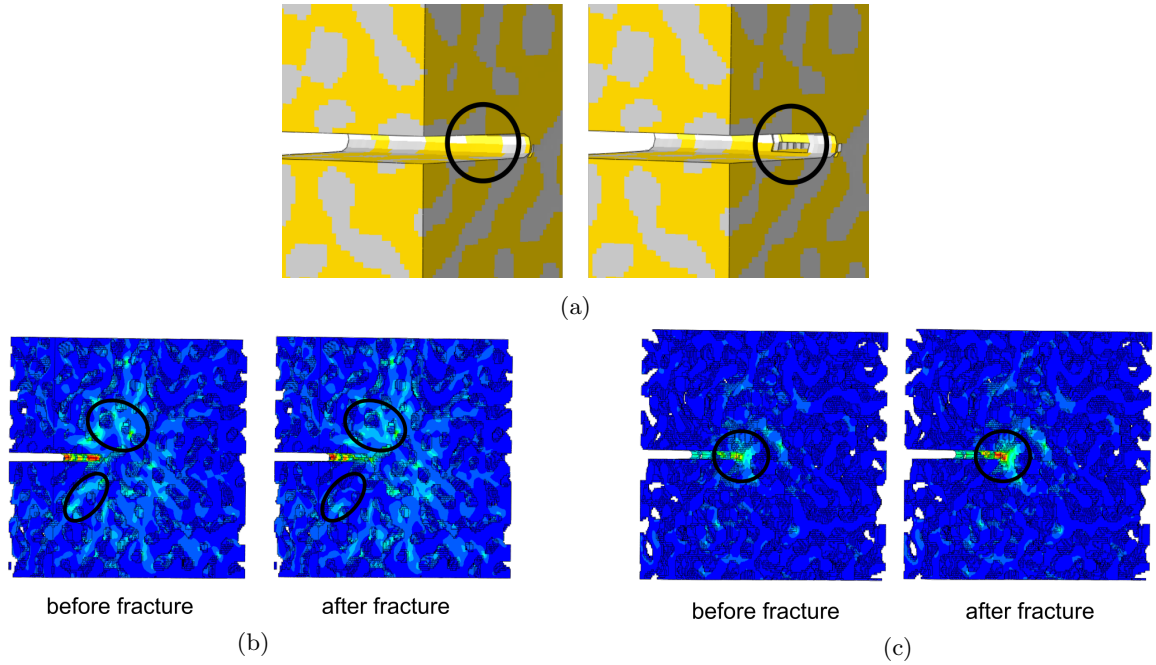

Fig. 3.10: (a) The gold ligament failure associated with marker 1 on Figure 3.9 and the stress re-distribution within the (b) gold and (c) polymer network associated with this.

There is far less jaggedness seen in the specimens with lower volume fractions. This however is not a result of the lack of ligament breakage but rather due to the damping effects of the polymer. In these specimens, the gold ligaments are surrounded by large amounts of polymer and so when the gold fractures the sudden loss of load carrying capacity is reduced as the polymer is able to absorb the energy transferred. Due to its ductile nature and large volume fraction, it can deform without failing. The stronger interconnectivity within the polymer gives it additional strength against fracture.

Figure 3.11 shows the number of elements that were deleted due to their exceeding the critical damage limit in specimens of each volume fraction for the polymer and metal phases separately. This allows comparisons to be made about the amount of damage required by each specimen to undergo complete failure.

The ratio of gold to polymer elements deleted at the ultimate fracture point is similar to the volume fraction of each constituent. That is, at high gold volume fractions more gold fails than polymer while at lower gold volume fractions significantly more polymer

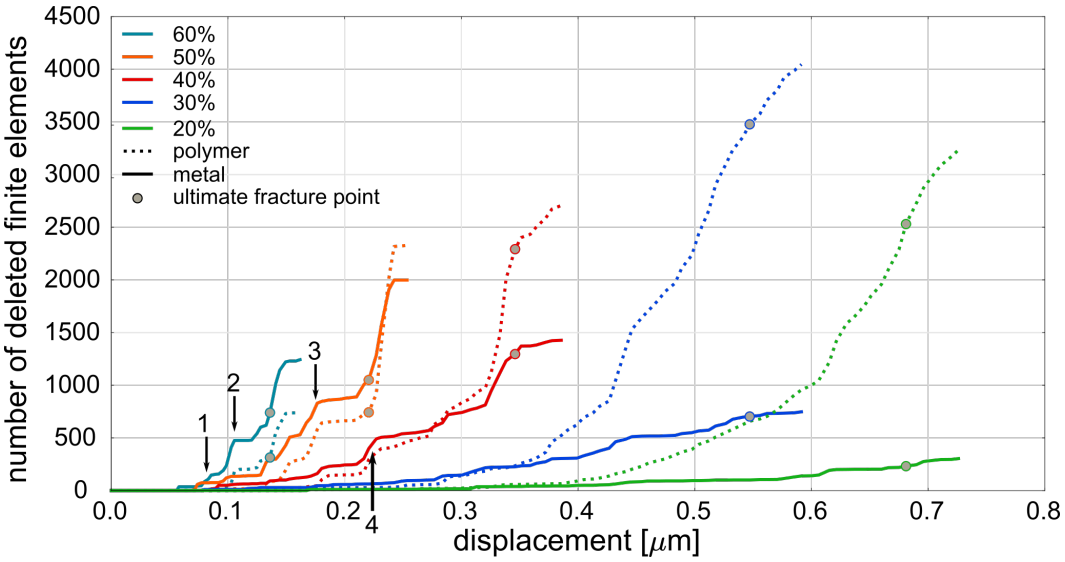

Fig. 3.11: The cumulative number of elements of each constituent that failed and thus were deleted during the CT test for each specimen at each volume fraction. The point of ultimate fracture is indicated with the filled in circles. The points marked 1 to 4 on Figure 3.9 are similarly marked here.[4]

failure is seen. In all samples the first element to fracture is of the gold constituent. The locations marked $1-4$ on Figure 3.9 are marked on Figure 3.11 and occur when several gold elements are deleted, thus indicating large gold ligament fractures as was previously suggested.

The sudden long vertical line segments at the ultimate fracture point indicates the brittle nature of the $60-40\%$ samples which are similar to the trends noted in the investigation by Kahng et al. of brittle randomly fused networks [117]. The complete failure of these specimens occurs when a large number of gold elements suddenly fail, which shows that the gold constituent controls the fracture displacement at the higher volume fractions. These gold ligament fractures are accompanied by a large number of polymer elements failing as a result of the sudden transfer of the load carried by the gold to the surrounding polymer phase (as also seen in Figure 3.10(c)). This load exceeds the maximum load that can be carried by the polymer and thus the polymer will immediately fail at this location.

Different behaviour is seen at the lower gold volume fractions. The failure of gold elements is very gradual. There are no significantly long vertical sections representative of a large number of gold elements failing. Although the gold still fractures in a brittle manner (that is, suddenly with no plastic deformation) this is not evident on

[4] Reproduced with permission from Elsevier (https://doi.org/10.1016/j.eml.2020.100815)

the curves. At these volume fractions, however, there is significant failure within the polymer as, with little reinforcement, it experiences most of the stress. Also, at ultimate failure there is no sudden rise in the fracture of gold elements as was noted at the higher volume fractions, only a continued exponential increase in polymer element failure. This suggests that the polymer material controls the fracture displacement at these lower volume fractions.

Additionally, at higher volume fractions the curves of the two constituents follow roughly the same trend. That is, both the gold and polymer suddenly rise and plateau simultaneously. Whereas at the lower volume fractions, the failure of the two constituents happens independently of each other. The polymer has an exponential increase in failed elements while the gold maintains a gradual and slow linear rate of failing elements.

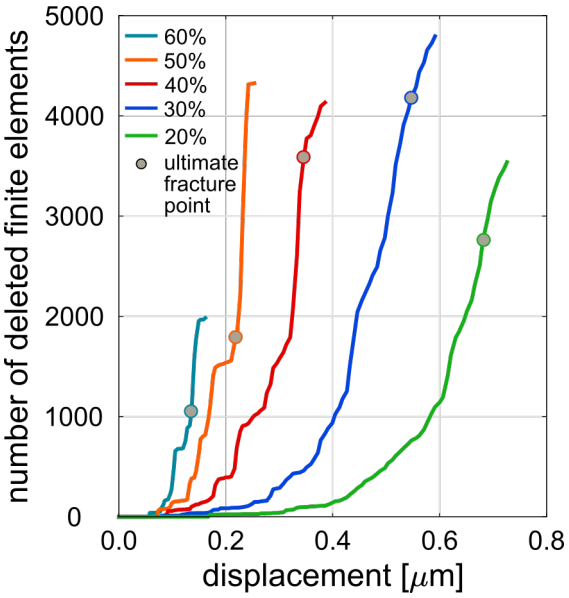

Fig. 3.12: The cumulative number of elements that failed in the full nanocomposite and were deleted during the CT test for each specimen at each volume fraction. The point of ultimate fracture is indicated with the filled in circles.

The resistance to failure of each specimen can be inferred, for comparative purposes, by looking at the total number of failed elements at ultimate fracture which is given in Figure 3.12. There is a trend of increasing resistance to failure as the gold volume fraction decreases from 60% to 30%. Based on the properties of each constituent this result is not unexpected. The gold material has a low resistance to fracture due to its brittle nature while the polymer has a high resistance to fracture corresponding to its

ductile nature. Thus, at high volume fractions one expects the gold to dominate the fracture behaviour, as observed here. A similar trend was noted by Spahr et al. [149] and Kinloch and Taylor [150] in their research of composites. Spahr et al. [149] noted that with an increase in fibres embedded in a polypropylene matrix, the fracture toughness of the material decreased. Kinloch and Taylor [150] noted a maximum fracture energy associated with a certain percentage of micro and nano-composite particles embedded in an epoxy matrix and above this a decrease in toughness was seen. Both researchers attributed this decrease to a lack of polymer material available to allow for the full distribution of the stresses within the composite. Following similar logic, Kinloch and Taylor [150] calculated that a minimum inter-particulate distance exists and with more particulates added this distance decreases which results in insufficient matrix material around each particles to successfully distribute the load. This concept would be analogous in this gold/polymer nanocomposite to both the decreased connectivity and decreased pore size of the polymer network as the gold volume fraction increases.

Thus, at the lowest volume fraction one would expect the number of elements to be at a maximum, however, this is not the case here. Interestingly, the 20% volume fraction specimen shows a decrease in fracture resistance. A suggested reason for this is that the gold network is at its weakest to begin with and then is continually weakened by ligament fractures while the polymer is unable to withstand the load imposed on it. The interplay between the strength of the gold network and the stress transfer ability of the polymer thus gives the 30% volume fraction sample the largest fracture resistance even though it does not have the largest strength as noted in Figure 3.9.

Figure 3.13 provides a visual depiction of the elements that are deleted during the CT tests. These, therefore, provide a visual representation of the crack propagation through the specimens. The volume of fractured material in Figure 3.13 is consistent with the results in Figure 3.12 where the 30% volume fraction specimen has the largest volume of fractured elements, while above and below this volume fraction a smaller volume of fractured elements is required for ultimate fracture to occur.

Comparing the crack propagation of the 20% and 60% volume fraction samples, significant differences are illustrated. At the lowest metal volume fraction, there is a significant amount of gold secondary cracking (cracking at locations far away from the crack tip). There is also a small amount of polymer fracturing as a result of the load transferring to the polymer as was explained earlier. This is consistent with the ductile

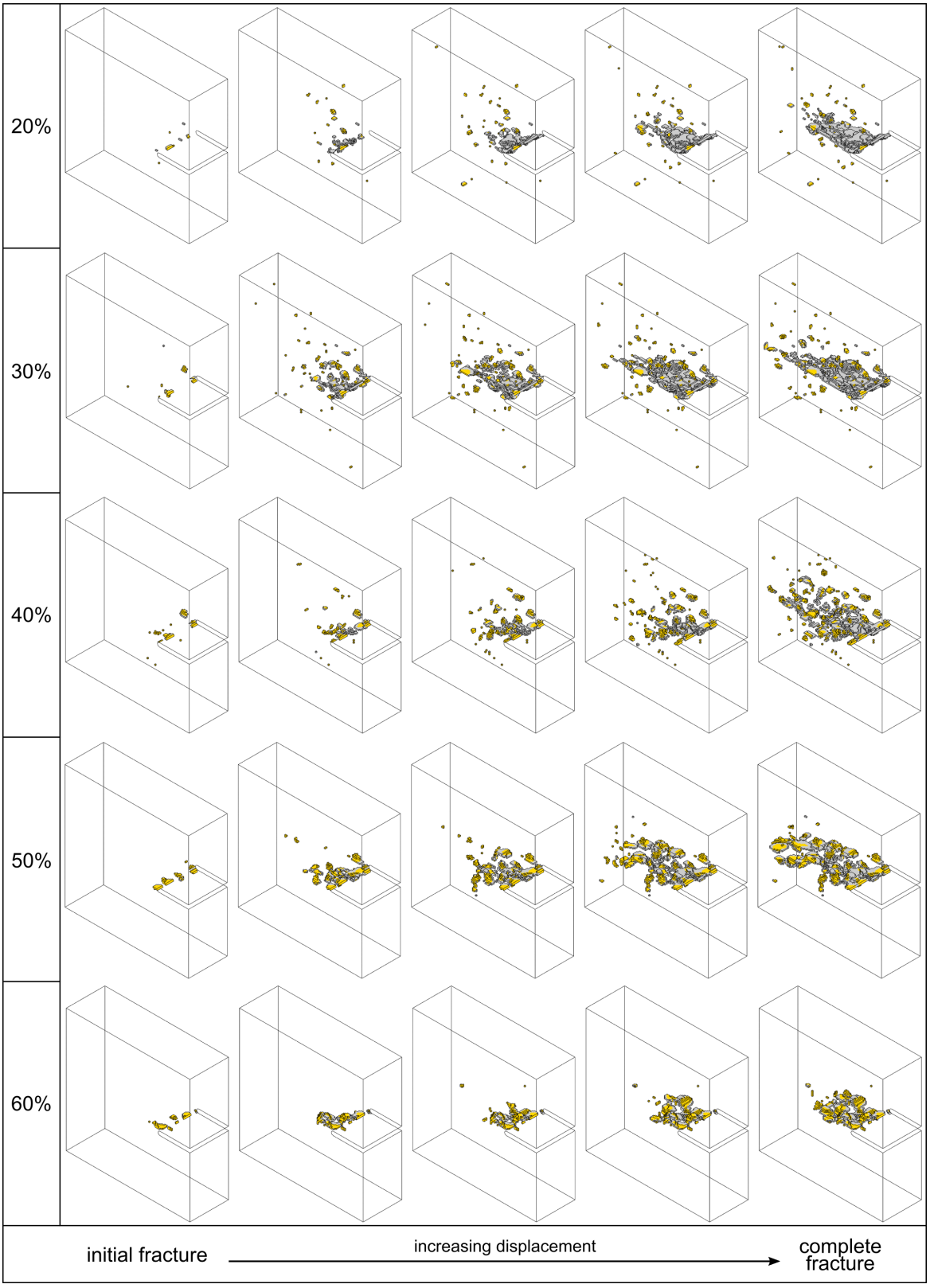

Fig. 3.13: Crack development and propagation through the VE section at each volume fraction. The deleted polymer elements due to failure are depicted in grey and the metal elements in gold.

network description of randomly fused networks [117]. This extensive secondary cracking is attributed to the low connectivity of the gold network allowing large localized deformation to occur. At these locations, the large amount of polymer causes the gold to undergo a large local displacement which causes it to fracture. As it is far away from the crack tip, however, this does not cause the entire material to fail. In contrast to this in the highest volume fraction specimens there is almost no secondary cracking. This is again consistent with a randomly fused network description of fracture [117]. As mentioned previously, due to the high connectivity of the gold network, localized deformation is prevented.

The presence of secondary cracking creates a high possibility of delamination. Lower volume fraction nanocomposite samples may thus be even weaker than observed here.

As the crack propagates it is also clear that the crack does not propagate in a straight line (that is, perpendicular to the applied loading). When the crack propagates through the polymer it will encounter gold ligaments in its path. As the gold is significantly stronger than the polymer the path of least resistance is not through the gold but rather around the gold. Thus the crack is deflected towards either locations of fractured gold or through the polymer. Both vertical and lateral crack propagation are evident in Figure 3.13. The vertical re-direction of the crack is shown in Figure 3.14 where the side view of the VE sections are depicted. The vertical deflection of the crack is most pronounced in the 40% volume fraction specimen as here the material has similar sized gold and polymer ligaments and so as the crack propagates through the polymer phase it encounters relatively large gold ligaments that hinder its progression. In the 60% volume fraction specimen a small amount of crack deflection is seen. Here the crack propagation occurs mainly in the gold phase and, since this is the stronger material, it does not encounter an obstacle that would arrest its propagation. At the lowest volume fraction there is also almost no vertical movement. As the gold network is less prevalent in this specimen and the polymer pores are comparatively large, the polymer can easily move through the material without being arrested by the presence of a gold ligaments.

Interestingly, Figure 3.14 shows that both the 20% and 60% volume fraction samples have two of the shortest crack lengths at ultimate fracture. At the lowest volume fraction this is due to the low strength of the material as a result of its large percentage of polymer while at the highest volume fraction, the brittleness of the material, due to its large percentage of gold, results in only a short crack needed for ultimate fracture.

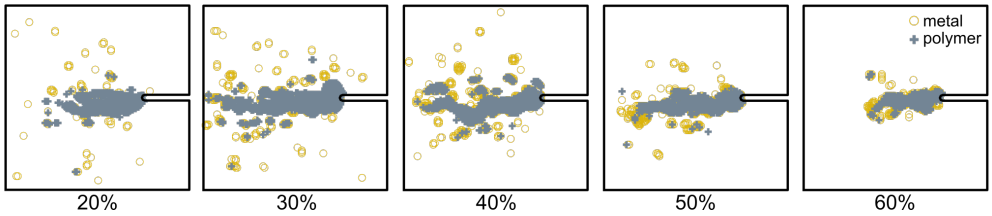

Fig. 3.14: Side view of the crack propagation through the specimen at each volume fraction showing the vertical crack deflection. The metal elements are depicted with a gold circle and the polymer with a grey cross

3.5.2 Comparison between gold/polymer nanocomposite and pure nanoporous gold

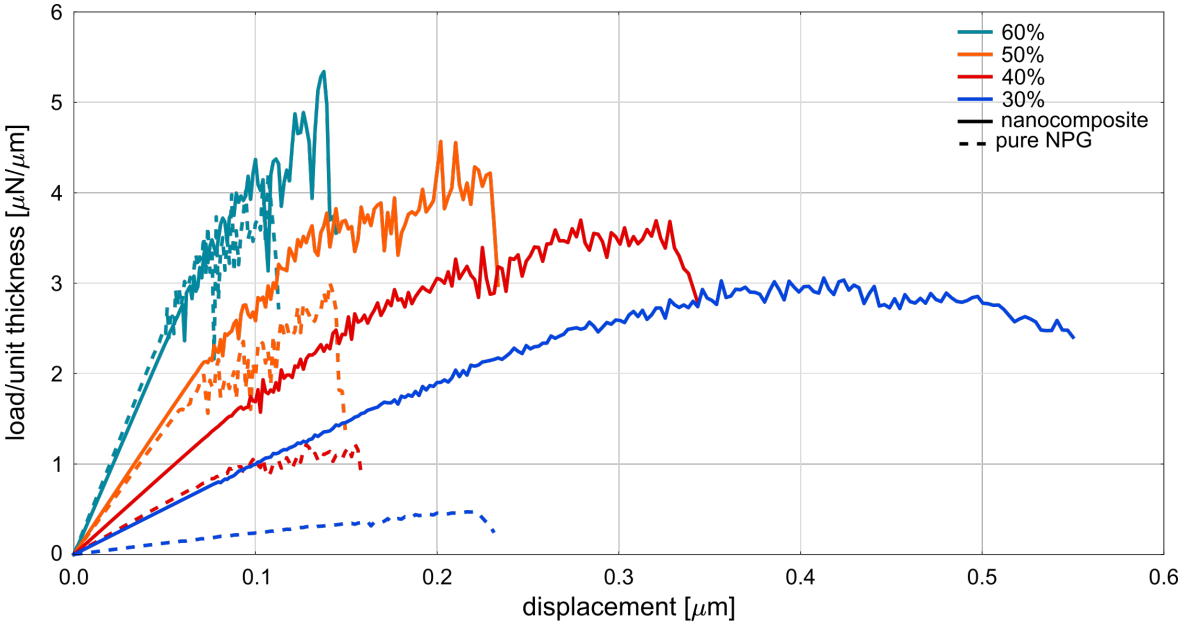

Fig. 3.15: Comparative load-displacement curves between the nanocomposite material and pure NPG specimens. Here the brittleness of the pure NPG can be seen in contrast to its composite counterpart. [5]

Load-displacement curves are shown in Figure 3.15 comparing the nanocomposite with its pure NPG counterpart. At the lowest volume fraction, both the maximum loads and the ultimate fracture displacements are significantly less for the pure NPG samples than for the nanocomposites. The lower ultimate fracture point is an indicator of the higher brittleness of pure NPG compared to the nanocomposite as discussed in the literature [5, 44]. Within the samples of pure NPG, the same trend as seen in the nanocomposite of increasing strength and decreasing fracture displacement for increas-

[5] Reproduced with permission from Elsevier (https://doi.org/10.1016/j.eml.2020.100815)

ing volume fraction of metal is shown. Furthermore a similar jaggedness in the curves is shown although there are far fewer ligament fractures required in the pure NPG for the network to weaken to a point where the entire material fractures. As discussed earlier, in the nanocomposite, when the gold ligament breaks, the stress is transferred and distributed through the gold network as well as to the polymer. Also, although the polymer is a low load carrying material, it was able to carry a fraction of the load thus reducing the load on the gold ligament network. The polymer network clearly stabilizes the ligaments in the nanocomposite thus delaying complete material failure.

In the lowest volume fraction pure NPG specimens, the small thickness of the specimens may result in a weaker connectivity than would be truly representative of pure NPG and this may result in the very low fracture strength and displacement at this volume fraction.

Figure 3.16 gives the displacement at ultimate fracture and the maximum load of pure NPG, the corresponding nanocomposite and bulk specimens of gold and polymer. Additionally, the upper and lower bounds by means of a weighted average formula of each property are shown. These bounds are calculated using the following:

$$f_{\text{upper}} = \left(\frac{\phi_M}{f_M} + \frac{\phi_P}{f_P} \right)^{-1} \quad \text{and} \quad f_{\text{lower}} = \phi_M f_M + \phi_P f_P \,,$$

where f_{upper} and f_{lower} are the upper and lower bounds respectively for a material property f of the composite. f_M and f_P are the values of property f for the bulk metal and bulk polymer constituent respectively. These bounds would correspond to a fibre-reinforced composite with brittle long fibres and a ductile matrix.

Figure 3.16(a) shows a decrease in fracture displacement with increasing volume fraction for both the nanocomposite and pure NPG specimens, although it is more obvious in the nanocomposite. This was similarly shown by Coldea et al. [151] in the investigation of polymer-infiltrated-ceramic-network composites. The improved ductility of the nanocomposite is represented by the larger fracture displacements compared to the small displacements achieved by the pure NPG at all volume fractions. As the volume fraction increases, however, the difference between the displacement of the nanocomposite and pure NPG becomes smaller; at a 60% volume fraction the fracture displacements are very similar. This is indicative of an increasing brittleness of the nanocomposite with an increase in the metal volume fraction.

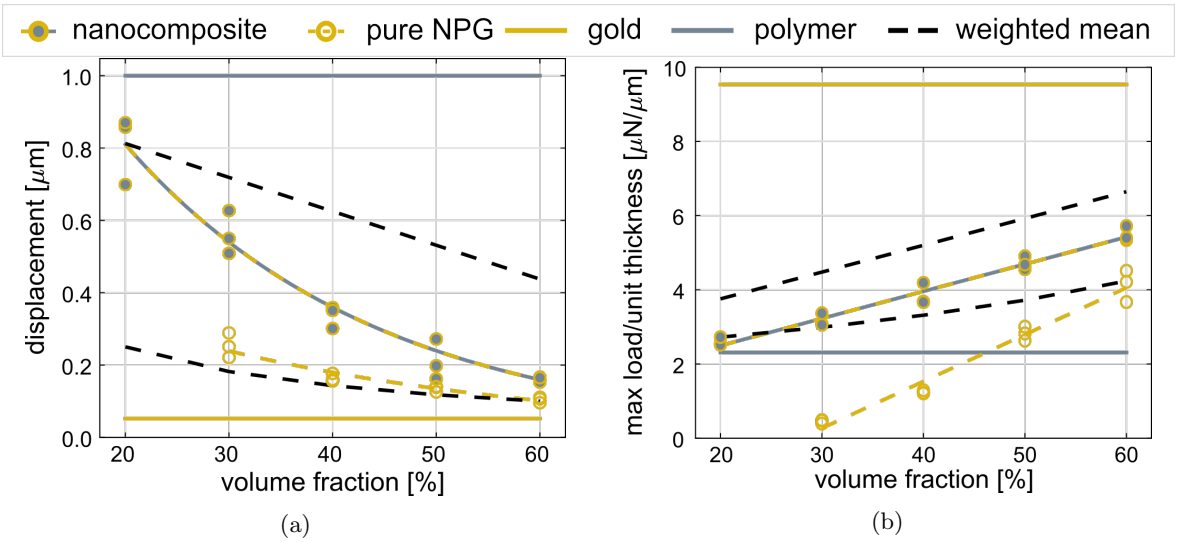

(a) (b)

Fig. 3.16: Influence of the gold volume fraction on (a) the displacement at complete fracture and (b) the maximum load sustained by nanocomposite and pure nanoporous gold specimens. Results for the bulk constituents as well as upper and lower bounds of a continuous and unidirectional fibre-reinforced composite are also included.[6]

In Figure 3.16(a) the lower bound estimates the fracture displacement for a fibre-reinforced composite loaded transverse to its fibre direction while the upper bound refers to the fracture displacement if loaded along the fibre direction. Both the nanocomposite and the pure NPG have fracture displacements that lie within the bounds of the fibre-reinforced composite. The nanocomposite spans almost the entire range of these bounds. Unlike fibre-reinforced composites the displacements achieved by the nanocomposite are expected in all directions of loading. Thus at a 20% volume fraction the nanocomposite will have the maximum available ductility of the fibre-reinforced composite in all directions unlike the composite which only has this high ductility when loaded along the fibre direction. A decrease in ductility will occur when loading the conventional composite at angles other than this. This makes the nanocomposite more versatile in its application and easier to use when designing structures with a complex mixture of loading. At the same time, however, the 60% volume fraction nanocomposite specimen will not show any improvement in its ductility if the loading direction changes whereas the fibre-reinforced composite will improve its ductility as the loading direction becomes parallel to the fibre direction. Thus, even though it may be simpler to design for, the use of the conventional fibre-reinforced composite could prove to be a superior choice if ductility is needed, especially in the cases of simple loading conditions (e.g., uniaxial).

[6] Reproduced with permission from Elsevier (https://doi.org/10.1016/j.eml.2020.100815)

Nanoporous gold performs poorly in both fracture displacement and maximum load especially when compared to its nanocomposite counterpart. This was again noted in the investigation of failure of ceramic/polymer materials [151]. The fracture displacement of the pure NPG material lies very close to the weighted average lower bound at each volume fraction. This is the weakest and most brittle response of the conventional fibre-reinforced composite. Improved ductility in the conventional composite is possible by changing the orientation of the loading, whereas, pure NPG will show no improvement in ductility and thus will exhibit this brittle response independent of the loading direction.

Compared to the bulk gold sample, both the pure NPG and nanocomposite have larger fracture displacements even though the pure NPG is very brittle. Upon loading its network structure allows for the distortion and re-orientation of ligaments without the generation of excessive stress. Thus it is able to deform more than bulk gold without fracturing. This also explains the decrease in fracture displacement with increasing volume fraction as the connectivity is strengthened.

Figure 3.16(b) shows the improvement in strength of both the pure NPG and nanocomposite that accompanies the increase in gold volume fraction. The pure NPG samples show a stronger dependence on gold volume fraction with increasing load compared to the nanocomposite. Other than at the lowest gold volume fraction, the nanocomposite lies within the bounds of fibre-reinforced composites where at a 20% volume fraction the nanocomposite shows a weaker response than the weakest loading direction of the conventional composite. In Figure 3.16(a), however, this nanocomposite showed an equal and possibly greater fracture displacement (i.e., superior ductility), thus highlighting the trade-off between strength and ductility. The differing responses to different loading directions and the required design complexity would also be a factor to consider in deciding between these two types of composites.

The nanocomposite is never able to replicate the strength of a fibre-reinforced composite in its strongest direction (given by the weighted mean upper bound) at any volume fraction (unlike the large span of the fracture displacement of the nanocomposite cf. Figure 3.16(a)). The strength of the nanocomposite lies closer to the weaker response of the conventional composite (given by the weighted mean lower bound) at all volume fractions. However it is worth mentioning, again, that this response is independent of loading direction, unlike that of the conventional composite.

The pure NPG has a lower strength than its nanocomposite at all volume fractions

with the difference between the two again decreasing as the volume fraction increases. At the lower gold volume fractions, pure NPG shows a much weaker response, even less than the polymer, and is significantly lower than the bulk gold sample even at its highest volume fraction (at a 60% gold volume fraction pure NPG has 40% of the strength of bulk gold). It is also always weaker than the weakest response of the fibre-reinforced composite.

For each property investigated, the results of the nanocomposite lie closer to that of the weaker performing constituent (i.e., closer to the fracture displacement of the gold and maximum load of the polymer) at all volume fractions. This shows how the weaker performing constituent dictates the material's performance in each of these properties. In other words, the maximum load is more significantly affected by the low load carrying capacity of the polymer compared to the superior strength of the gold constituent and the displacement at fracture is influenced more by the brittle nature of gold compared to the ductility of the polymer. The fracture displacement relative to the bulk polymer sample and the maximum load relative to the bulk gold material are given in Table 3.4. This allows one to see the percentage influence of the superior property of each constituent on the properties of the nanocomposite.

Table 3.4: Comparison of the displacement at complete fracture and maximum load between nanocomposite specimens and that of pure polymer and gold specimens respectively for each gold volume fraction.

Volume fraction [%]	$\text{Disp}/\text{Disp}_{\text{polymer}}$ [%]	$\text{Load}/\text{Load}_{\text{gold}}$ [%]
20	81	27
30	56	33
40	34	40
50	24	49
60	16	58

Considering first the relative load carrying capacity at each volume fraction, the percentage influence is generally consistent with the amount of gold present in the nanocomposite. That is, at a 60% volume fraction the relative maximum load is similar (58%) and is similarly consistent at the other volume fractions with a slightly higher comparative load at the lower volume fractions e.g., a 27% comparative load at a 20% volume fraction. The combined loss of strength due to the porous nature of the gold ligament network (which results in the lower strength values seen in the pure NPG samples in Figure 3.15) and the influence of the polymer on the load carrying capacity

of the material are thus suggested to be of equal relevance.

Focusing next on the comparative fracture displacements and the relationship between the percentage polymer, the same trend is not noticed. At a 20% gold volume fraction the comparative displacement is similar to the percentage polymer present (81% with 80% polymer) however at a 60% gold volume fraction, there is a significantly lower comparative displacement (16% with 40% polymer). This suggests that at the lower volume fractions the brittle nature of the gold does not have as great an influence on the ductility of the material. This is likely as a result of the decrease in connectivity as the gold volume fraction decreases.

Figure 3.17 gives the crack propagation of the pure NPG. Compared with the nanocomposite (Figure 3.13), a few similarities are noted. The dispersed nature of the crack at the lower volume fraction is evident, and at the highest (60%) and lowest (20%) volume fractions the samples have the shortest crack lengths. However, all pure NPG specimens have shorter crack lengths than their nanocomposite counterparts.

The number of deleted gold elements at ultimate fracture in the pure NPG samples compared to the nanocomposite specimens is given in Table 3.5. At volume fractions between 30 and 50% the number of fractured gold elements in the pure NPG specimens are significantly lower than in the nanocomposite specimens as the polymer supports and stabilizes the gold network in the nanocomposite, allowing for more gold ligaments to break without complete fracture occurring. At a 60% volume fraction, the difference is negligible as a result of the small percentage of polymer surrounding the gold network.

Table 3.5: The number of deleted gold elements at complete fracture in the pure NPG and nanocomposite samples respectively.

Volume fraction [%]	Number of deleted elements	
	Pure NPG	Nanocomposite
30	52	697
40	350	1296
50	1403	1567
60	1258	1230

The 30% specimen shows a large amount of secondary cracking in Figure 3.17 with no

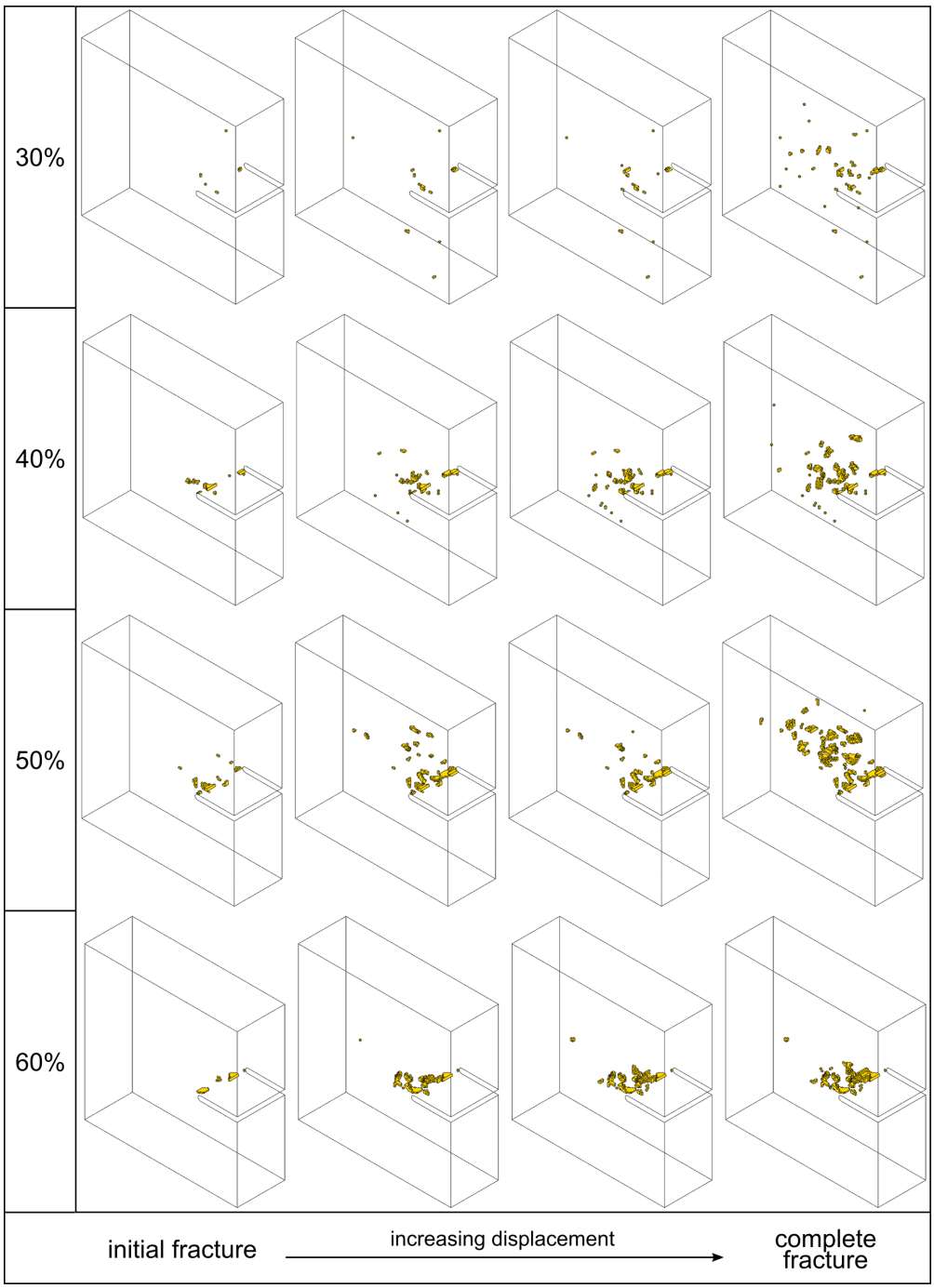

Fig. 3.17: Crack development and propagation through the VE sections of NPG at each volume fraction where the deleted metal elements due to failure are depicted in gold.

distinct crack propagation emanating from the crack tip at ultimate fracture. Table 3.5 also gives a very small number of deleted and hence fractured elements at complete fracture. The low connectivity of this low volume fraction specimen is suggested as the reason for very few ligament failures required for complete fracture to occur.

The comparative fracture resistance of each specimen is quantified by calculating the

work to fracture from the area underneath each load-displacement curve in Figures 3.9 and 3.15. The results are shown in Figure 3.18.

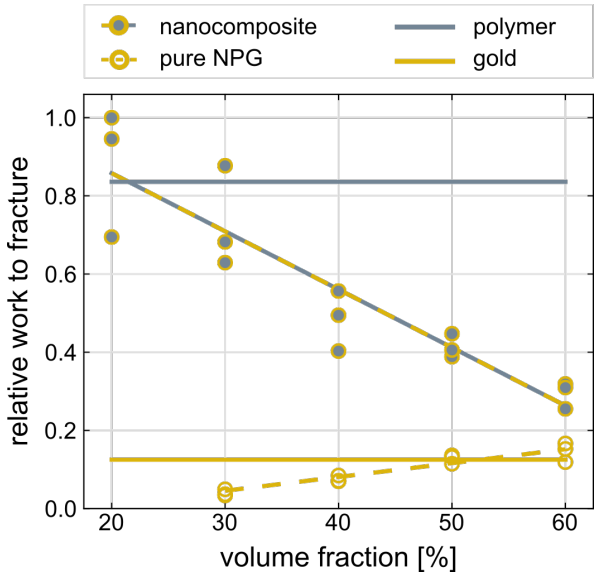

Fig. 3.18: Relative work to fracture of pure NPG and nanocomposite at different gold volume fractions. The work to fracture is also given for bulk polymer and gold for comparison. The nanocomposite specimens show a significantly improved resistance to fracture compared to the pure NPG specimens.[7]

Resistance to fracture decreases with increasing volume fraction in the nanocomposite. This is due to the improved ductility with decreasing gold volume fraction and the prevalence of different toughening mechanisms. There are three extrinsic toughening mechanisms exhibited by the nanocomposite: i) secondary cracking, ii) crack deflection and iii) crack bridging.

As discussed in Section 3.2.3, secondary cracking of the gold material in locations far away from the crack tip allows for the dissipation of energy from the crack tip without advancement of the crack tip [152, 153]. As seen in Figure 3.13, the lower the volume fraction of gold, the further away from the crack tip this secondary cracking occurs, which is a pre-requisite for this mechanism to be effective. In the higher volume fraction specimens, the secondary cracking occurs closer to the crack tip, thus allowing for the crack to advance suddenly by means of a coalescence of the cracks. This secondary cracking results in a crack length long enough to cause complete failure, thus contributing to its relatively brittle fracture response.

[7] Reproduced with permission from Elsevier (https://doi.org/10.1016/j.eml.2020.100815)

Crack deflection, the movement of the crack vertically and laterally when hindered by a gold ligament, results in a tortuous crack path. As lateral crack propagation blunts the crack tip, the stress concentration at the crack tip is reduced, and hence the driving force of the crack is decreased. This is noted to some extent in all the nanocomposite samples in Figures 3.13 and 3.14.

Crack bridging occurs when the polymer is stretched across the crack tip between two gold ligaments. The tensile extension of the polymer allows for energy to be released without causing complete fracture. Other metal infiltrated ceramic composites show a similar mechanism that has contributed to their improved ductility [150, 154]. Understandably, the greater the volume of polymer (lower volume fraction of gold), the more prevalent this mechanism becomes. This is shown in Figure 3.19 where the strain in the loading direction at the fractured surfaces of the 20% and 50% specimen are shown. The greater the extension the greater the energy dissipated by this mechanism. The 20% sample shows significantly greater extension of the polymer material.

At the lowest volume fraction, the nanocomposite has a high resistance to fracture, even greater than that of the highly ductile bulk polymer material. While the bulk polymer only has intrinsic toughening mechanisms, the 20% gold volume fraction specimen has both intrinsic toughening and shows all three extrinsic toughening mechanisms.

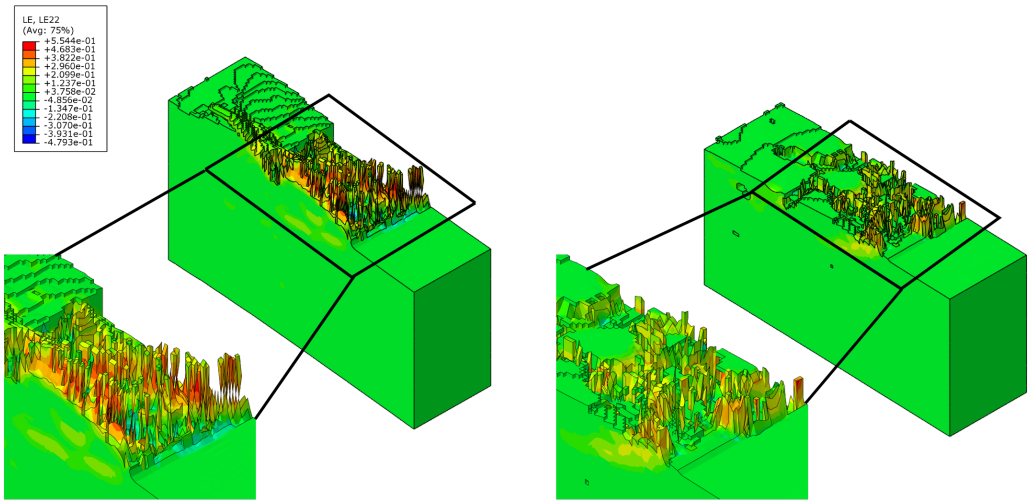

Fig. 3.19: Strain plots of the fractured surfaces of the 20% (left) and 50% (right) gold volume fraction specimens at complete fracture. There is more strain and thus more significant crack bridging noted in the lower volume fraction sample.

As expected, the pure NPG has a lower fracture resistance than the nanocomposite at all volume fractions. A slight increase in resistance with increasing volume fraction is noted. Aside from the intrinsically brittle nature of the gold as a cause, the lack of polymer matrix to allow for stress re-distribution away from the crack tip results in a process zone that is limited by the ligament diameter. The small size of the process zone causes a high stress concentration at the crack tip which drives the crack propagation. Additionally, none of the three toughening mechanisms can be utilized by pure NPG. At the lowest volume fractions, pure NPG even shows a lower resistance to fracture than the extremely brittle bulk gold specimen. Due to the porous nature and low connectivity at these volume fractions pure NPG has a much reduced load carrying capacity and strength.

Figures 3.20(a) through 3.20(d) provide comparisons of a combination of mechanical properties using four Ashby plots: strength-density (Figure 3.20(a)), Young's modulus-strength (Figure 3.20(b)), toughness-Young's modulus (Figure 3.20(c)) and toughness-strength (Figure 3.20(d)). Strength here was determined from the largest load reached on the load-displacement curves, and toughness was quantified from the work to fracture calculations. In all four plots the volume fraction of gold increases from left to right.

In Figure 3.20(a) it is most desirable for materials to lie in the upper left corner as these materials have the greatest strength-to-weight ratio. Compared to the pure NPG material, the nanocomposite has a higher strength to weight ratio. Although the nanocomposite and the pure NPG span a similar density ($x-$axis), the nanocomposite has a much greater strength ($y-$axis), especially at the lower volume fractions (far left values). This is a highly sought after feature for any material as an increase in strength would not cause a large increase in density, thus giving a light, strong material.

Figure 3.20(b) shows that although both materials are able to cover a similar range of Young's moduli by changing the volume fraction of gold, the nanocomposite has the additional property of superior strength especially at the higher volume fractions. Interestingly the larger volume fraction pure NPG specimens have an equal and even greater strength than the lowest volume fraction nanocomposite specimen but with much higher Young's moduli. This may be beneficial when designing a structure as materials with similar strengths are available at different stiffness values.

In Figure 3.20(c), tough materials are expected to lie in the upper left corner and

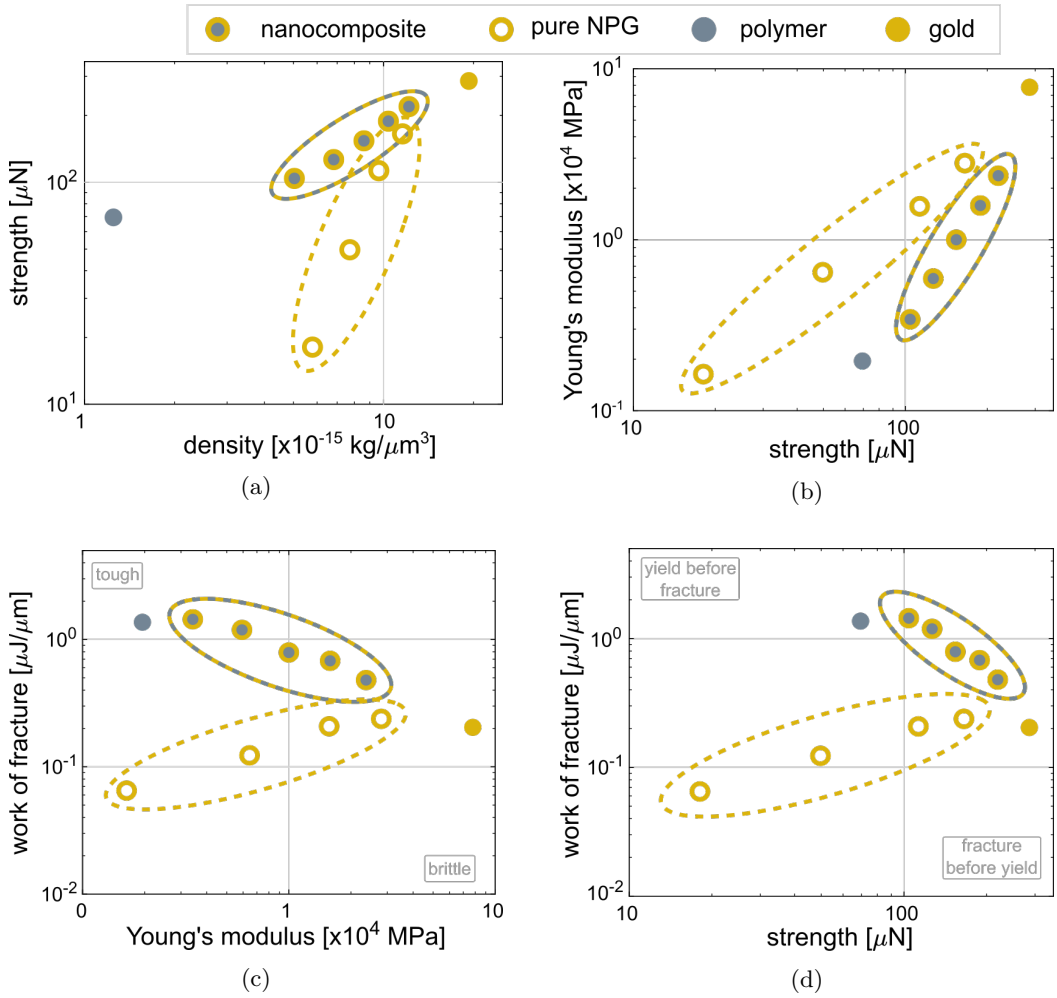

Fig. 3.20: Ashby plots: (a) strength-density, (b) Young's modulus-strength, (c) toughness-Young's modulus and (d) toughness-strength. Volume fraction increases within encircled material type in all plots from left to right.[8]

brittle materials in the bottom right. Again, the pure NPG and nanocomposite sit in a similar position horizontally but the nanocomposite sits higher than pure NPG at all volume fractions. This is due to the ductility enhancement in the nanocomposite by the impregnation of the polymer. The nanocomposite has a favourable combination of a relatively high toughness at a variety of Young's moduli.

Finally, the combination of strength and toughness in the nanocomposite compared to the pure NPG material is evident in Figure 3.20(d). At the lowest volume fraction, the nanocomposite has both a greater strength and toughness than the bulk polymer indicative of a relatively strong yet ductile material. On the other hand, the pure NPG material shows the unfavourable characteristics of both a weak and brittle material. Another feature indicated by this plot is the likelihood of the type of failure

[8] Reproduced with permission from Elsevier (https://doi.org/10.1016/j.eml.2020.100815)

of a material. It is favourable for materials to yield before fracture as yielding is a slower, less catastrophic, process. From Figure 3.20(d) is is evident that the nanocomposite is more likely to undergo yielding before fracture compared to the pure NPG material. Classically, as one moves diagonally from the upper left to bottom right, a decrease in the size of the process zone is also noted. This is in agreement with what is observed in the nanocomposite, and will be discussed further in the following section.

As expected, in all categories the results for the nanocomposite lie between those of the bulk gold and polymer values on all four diagrams, thus creating a selection of a combination of properties in the range between these two very different materials. Furthermore, although the pure NPG shows weaker performance on all plots, it does provide an even wider range of material options, which may be useful for certain applications.

3.5.3 Midplane and free surface

Figure 3.21 displays the stress plots of each constituent individually at the free surface of the RVE as well as at the midplane. The pure polymer sample has a very large process zone, indicative of its ductile nature. The pure gold sample has a very small process zone compared to the polymer, indicative of its highly brittle nature. The most noticeable feature is the decrease in the area of the process zone in the polymer constituent with an increase in gold volume fraction. A large process zone allows the specimen to undergo greater displacement before reaching the critical stress at the crack tip, which would result in fracture. As this process zone decreases, the stress is concentrated in a region around the crack tip, and less energy is distributed throughout the material. This results in only a small amount of deformation before the stress at the crack tip initiates crack propagation and the material fractures. This small process zone is consistent with the findings of Spahr et al. [149] and Kinloch and Taylor [150], as discussed in Section 3.5.1.

The effects of the size of the process zone on material ductility can also be extended to explain the extreme brittleness of the pure NPG samples. In pure NPG, the stress distribution and hence area of the process zone is confined to the ligament diameters, thus resulting in a small process zone and an extremely brittle response. There may be some distribution throughout the ligament network, but this would be small compared to the distribution by the polymer in the nanocomposite.

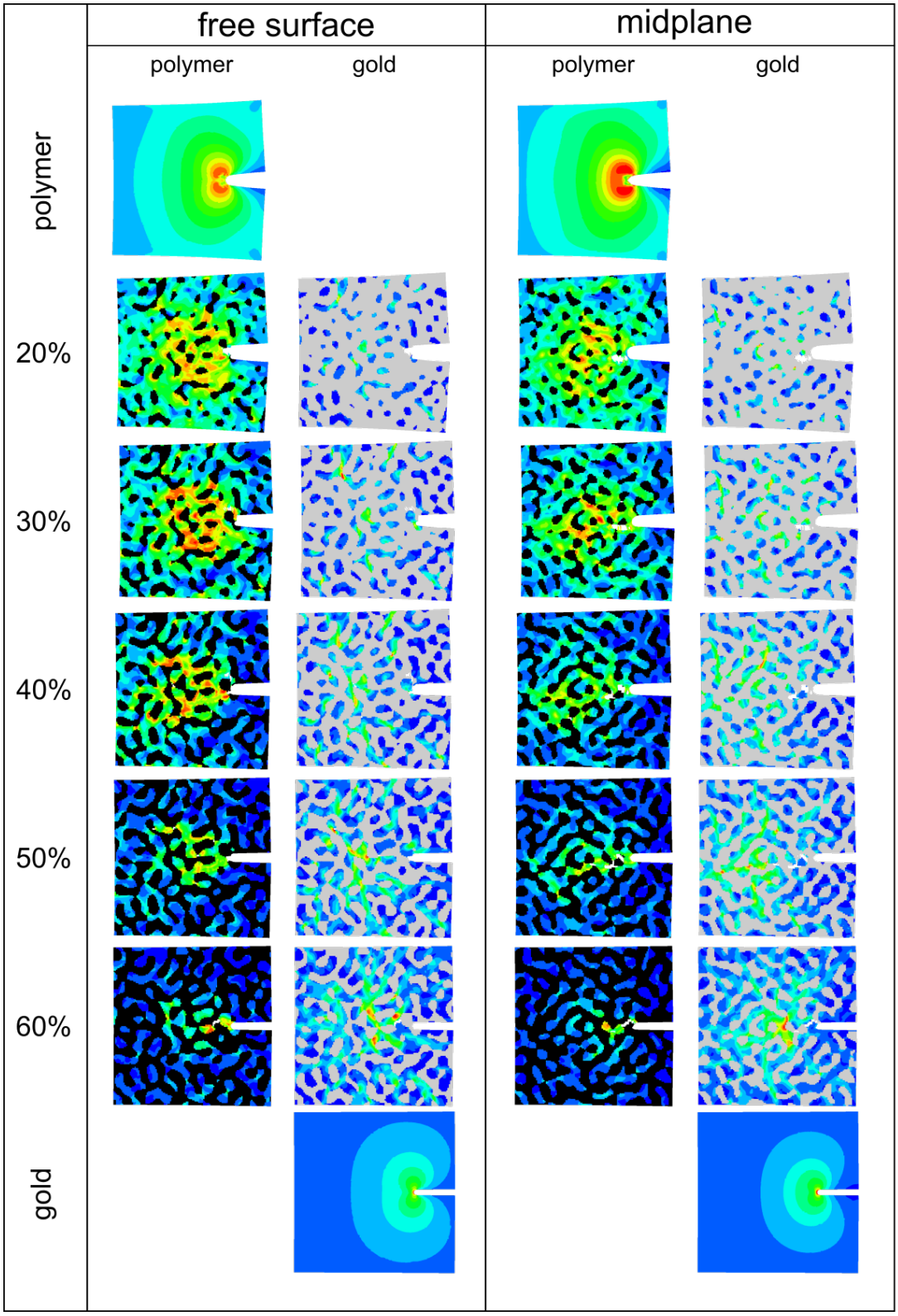

Fig. 3.21: A comparison between the von Mises stress distribution at the free surface and midplane surface of the RVE sections just before they undergo ultimate fracture (90% of ultimate fracture displacement). The stress contours for the pure polymer and pure gold material are also given.[9]

The gold constituent does not show a trend in process zone area changes with volume fraction. At all gold volume fractions, however, localized regions of high stress concentrations far away from the crack tip are seen. These localised stress locations are more prevalent in the larger volume fraction samples. As previously stated, at larger volume fractions the network connectivity is strengthened, thus preventing localized displacement of the material without significant increases in the stress at these locations. These localised regions result in secondary cracking occurring far away from the crack tip, which enhances the fracture toughness. Areas of secondary cracking are shown and encircled in Figure 3.22.

A larger process zone is shown on the free surface than on the midplane surface of all specimens. As the material is less constrained on the outer surface deformation can occur as was described in Section 3.2.4 with regards to the case of plane strain fracture behaviour. As a result more elements fail at the midplane compared to at the free surface. This is also shown in Figure 3.22.
In Figure 3.22 crack initiation is not seen in the 50% sample. Most of the failed and hence removed elements in the bottom right frame of Figure 3.22 are of the gold constituent due to the stiffness of the gold network. A few of the surrounding polymer elements failed due to the load transfer described previously. This secondary cracking does not directly contribute to the failure of the material. Many gold ligaments fail while the material continues to withstand an increase in load (Figure 3.9). Crack initiation has therefore yet to occur in this higher volume fraction specimen, whereas in the 20% volume fraction sample a noticeable crack propagation is seen. Crack bridging is also seen in the 20% specimens in Figure 3.22.

Figure 3.23 shows the decrease in lateral deformation of the nanocomposite samples with increasing gold volume fraction. At higher gold volume fractions a state of plane strain dominates the behaviour. A state of plane strain is indicative of a brittle fracture response. On the other hand, in the lower gold volume fraction samples the ductility of these samples allows for lateral contraction which shows a state of plane stress dominating at the free surface. This state is indicative of a ductile fracture response. Thus a transition from a ductile to a more brittle material is shown by the decrease in lateral contraction.

[9] Reproduced with permission from Elsevier (https://doi.org/10.1016/j.eml.2020.100815)

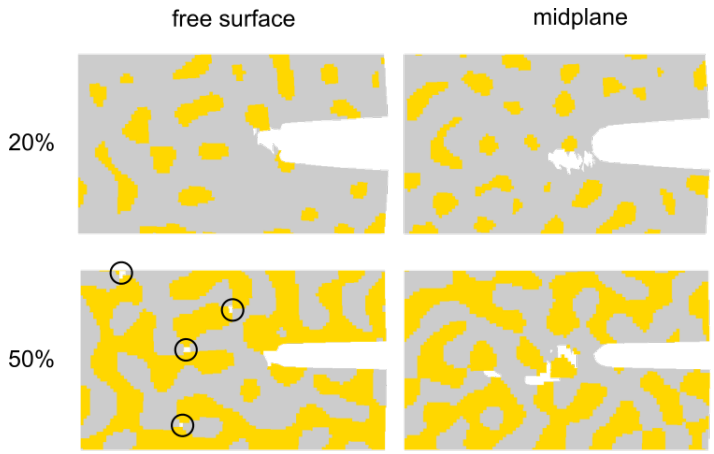

Fig. 3.22: Close up of crack tip of the 20 and 50% volume fraction specimens at the midplane and free surface. Longer crack tip and more damage was noted at the midplane compared to the free surface.

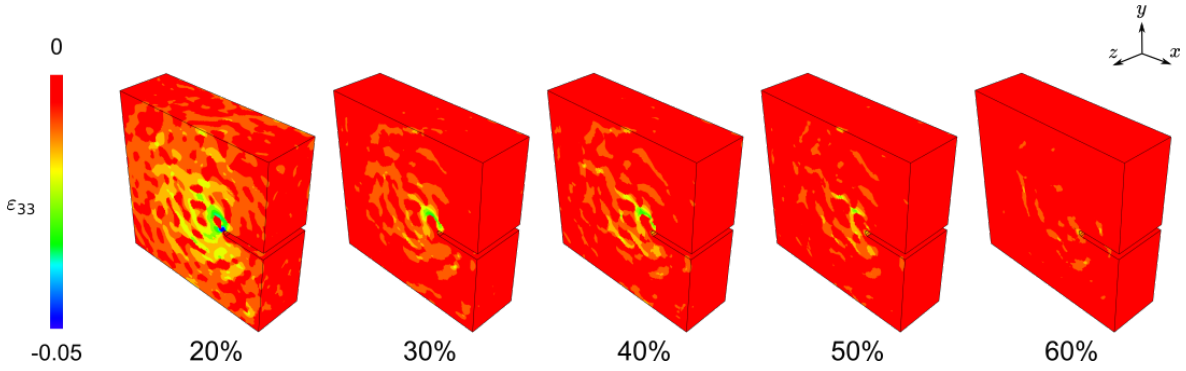

Fig. 3.23: Comparison of lateral strain (ε_{33}) showing more thinning at lower volume fractions which is indicative of a more ductile material.

3.5.4 Effects of specimen thickness

To further investigate plane strain-plane stress effects, Figure 3.24 gives the displacement at which the first finite element is deleted due to reaching the critical damage limit. In the 20% and 30% volume fraction the displacement at which the first element is removed increases as the thickness decreases. This is as expected and suggests a move towards plane stress fracture from a more brittle plane strain fracture. This trend is not as clearly observed in the specimens containing more than 30% gold. These specimens are stiffer and more brittle and so display plane strain fracture at all thicknesses due to the high resistance to contract laterally. Additionally, the ductility increase associated with the decrease of gold volume fraction is noted by a corresponding increase in displacement at first element failure with a decrease in gold volume fraction at each thickness ratio.

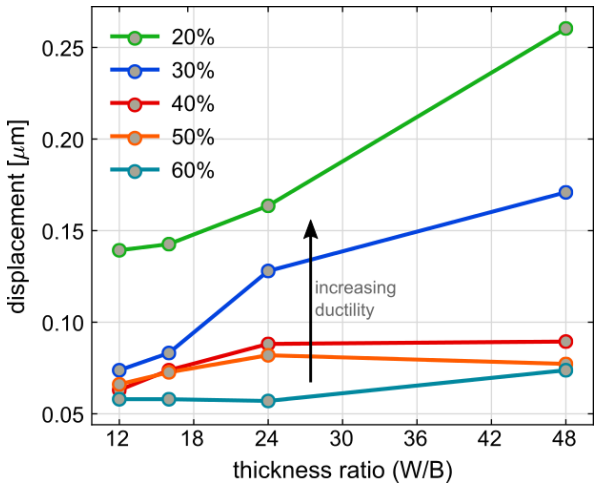

Fig. 3.24: Plane strain-plane stress effects are shown by looking at the displacement of the CT-specimens when the first finite element is deleted due to damage. At the lower volume fractions the clear trend of delayed failure with decreasing thickness is noted. This is not noticeable above 40% due to the intrinsic brittleness of the specimens as the metal volume fraction increases.

4

Chemo-electro-mechanical coupling in the nanocomposite

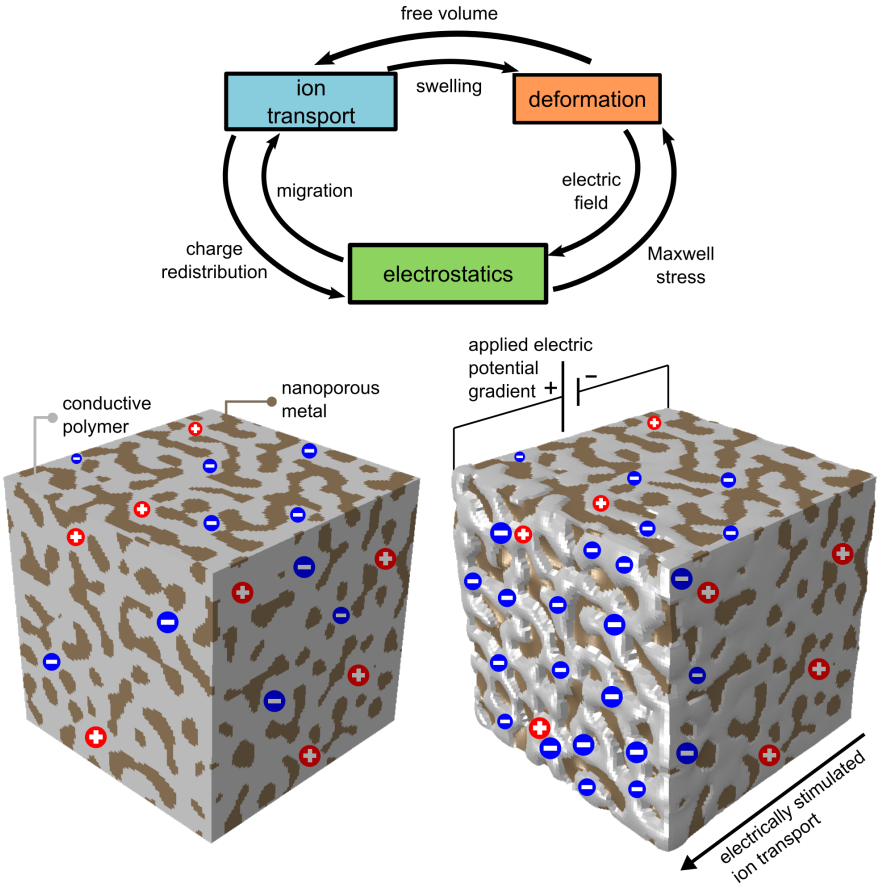

The motivation for this chapter is the functionality that arises from impregnation of the pores in nanoporous gold with a polymer. Within the polymer a mechanism exists such that, upon electrical stimulation, it shrinks or expands. With the nanoporous gold providing a reinforcing skeleton, there is an opportunity for this material to be used in actuation applications. The effects of the gold volume fraction on the actuation response of this material is investigated here.

4.1 Introduction

Certain polymers have the ability to change size or shape in the presence of an electric field. These materials are termed electroactive polymers (EAPs). Compared to other commonly used electrically stimulated materials such as shape memory alloys or electroactive ceramics, electroactive polymers have many superior properties, including actuation strains that are orders of magnitude larger, and significantly lower power consumption than these other compounds. These properties have motivated their use as sensors or actuators in microelectronic mechanical systems (MEMS), or as artificial biomimetic robots or muscles. The mechanism by which EAPs deform can be of an electronic or ionic nature, which motivates their division into two major groups: Electronic EAPs and Ionic EAPs [155].

4.1.1 Electronic EAPs

In electronic EAPs an electric field and Coulomb forces cause the polymer to deform. In electronic EAPs the deformation is as a result of an electric field causing the polarization of the crystalline material, or a rearrangement of cross-linked polymer chains. The Coulomb field can also directly cause strains in these materials. Examples of electronic EAPs include electrostrictive, electrostatic, piezoelectric, and ferroelectric materials. The advantages of these materials include their fast response time and high mechanical energy density. A shortcoming is the high activation electric field required to activate the deformation mechanisms.

4.1.2 Ionic EAPs

Ionic EAPs undergo a volume change due to, for example, the movement of ions within the polymer network as in an ionomeric polymer-metal composite [156], the diffusion of ions through a material from an electrolyte as in conductive polymers [157], ionic polymer gels [158] or, for carbon nanotubes, a change in the carbon-carbon bond length. These EAPs are advantageous as they exhibit large strains under a relatively low activation voltage. The diffusion of ions, however, means that these materials have a slower actuation process compared to the actuation reaction of electronic EAPs which is orders of magnitude faster. Examples of these materials include ionic polymer-metal composites (IPMC), conductive polymers, carbon nanotubes, and ionic polymer gels. In this work we only consider conductive polymers.

Conductive polymers

Conductive polymers (CPs) such as polypyrrole (PPy) and polyaniline (PANI) are insulating in their neutral state. A conductive state is reached through a chemically or electrochemically induced process called 'doping', whereby a charge is induced through reduction or oxidation of the polymer. This results in compensatory cations or anions moving into the polymer to balance this charge. Although this mechanism allows these polymers to be used in a variety of applications such as batteries, super-capacitors and chemical separators, to name a few, this doping mechanism also facilitates the volume expansion and contraction of conductive polymers, which motivates its use as an actuator. The movement of ions into and out of the electrode results in its expansion (as shown in Figure 4.1) and shrinkage respectively [159–162]. These compensatory ions are provided by an electrolyte into which the conductive polymers are immersed. Whether oxidation causes ions to enter or exit the polymer depends on the size of the anions.

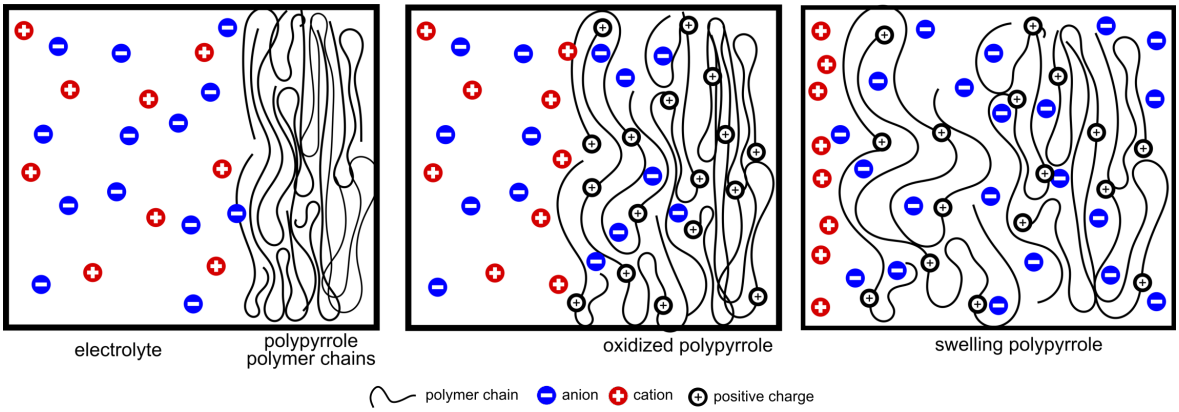

Fig. 4.1: Schematic representation of the volumetric swelling caused by an influx of small ions due to the oxidation of the conductive polymer as described by (4.1).

If the anions in the polymer are small enough to move, deformation occurs as a result of the gain or loss of anions in a region. Alternatively, if the anions are too large to move, cation movement causes the volume change in the polymer [155]. These two reactions may be summarised as

$$[(\text{polymer})]_{\text{solid}} + \text{n}\left(A^{-}\right)_{\text{solution}} \underset{\textbf{red}}{\overset{\textbf{ox}}{\rightleftharpoons}} \left[(\text{polymer})^{\text{n}+} \quad \text{n}(A^{-})\right]_{\text{solid}} + \text{n}\left(e^{-}\right)_{\text{metal}} \tag{4.1}$$

and

$$\left[(\text{polymer}) \quad \text{n}(MA^-) \quad \text{n}\left(C^+\right)\right]_{\text{solid}} \underset{\text{red}}{\overset{\text{ox}}{\rightleftharpoons}} \left[(\text{polymer})^{\text{n}+} \quad \text{n}(MA^-)\right]_{\text{solid}} + \text{n}\left(C^+\right)_{\text{solution}} + \text{n}\left(e^-\right)_{\text{metal}} , \quad (4.2)$$

respectively. Here n$(\cdot)$ is the number of the $(\cdot)$ chemical species within the reaction.

In (4.1), anion (A^-) movement compensates for the polymer charge with oxidation causing expansion and reduction causing shrinkage of the polymer. In (4.2) due to the immobility of macroscopic anions (MA^-), cation (C^+) movement occurs to compensate for the polymer charge with reduction causing expansion and oxidation causing shrinkage of the polymer.

Simultaneous anion and cation movement can occur when medium sized anions are present. However, this results in a smaller volume change than the previous two cases.

The redox reactions and resulting deformation occur within an electrochemical cell arrangement in which a conductive polymer is connected as a working electrode [163]. The presence of a counter electrode and electrolytic solution is also necessary. If the conductive polymer is attached to a film that undergoes no volume change in either a bilayer (Figure 4.2(a)) or trilayer (Figure 4.2(b)) arrangement, the polymer's expansion or contraction results in a bending deformation.

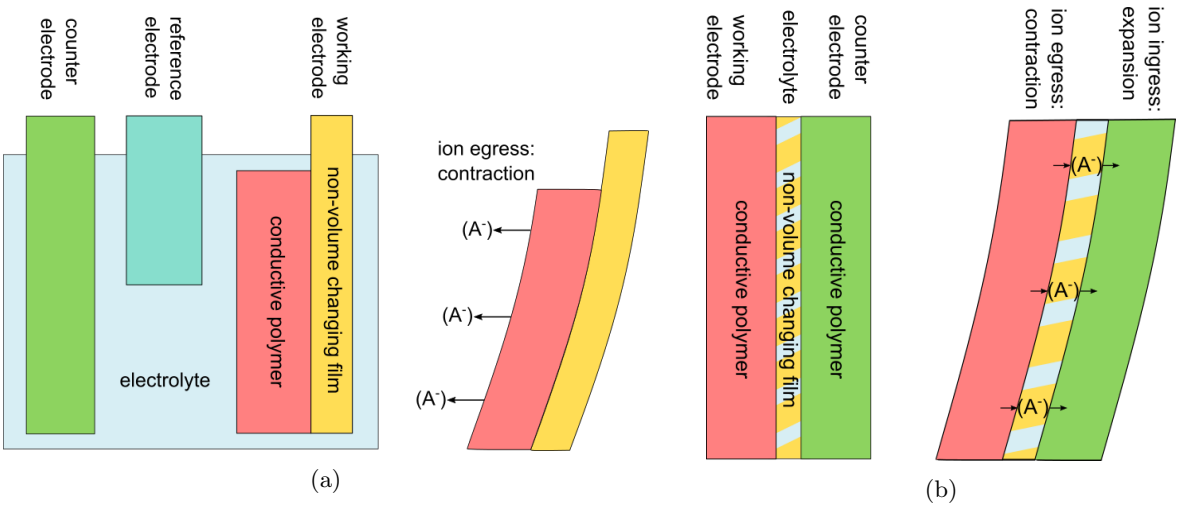

(a) (b)

Fig. 4.2: Conductive polymer film in a (a) bilayer and (b) trilayer arrangement with an electrolytic film between the two CP electrodes through which the ions move. A volume shrinkage as a result of ions exiting the material and expansion due to ions entering results in a bending deformation.

In the trilayer arrangement, a counter electrode is no longer necessary as one of the two polymer films would now take on this role. This arrangement also creates an opportunity to remove the electrolyte by using an electrolytic film in place of the non-volume changing film (e.g., a paper film soaked in an electrolytic solution) to facilitate the anion movement between the films. The removal of the need for an electrolyte solution could greatly expand the applications of conductive polymers.

There are several advantages to the use of conductive polymers as actuators [163]. CPs utilize both electronic and ionic conductive mechanisms as the redox reaction is triggered by an electric field. This is similar to the mechanisms in the the body to actuate muscles. This suggests that CPs may be easily implemented as artificial muscles, compared to pure electronic or purely ionic polymers. CPs are also biocompatible and require low voltages for actuation, two necessary characteristics of materials to be used within the human body. Additionally, their actuation force can easily exceed that of human muscles. The strain produced due to volume change is also significant.

Some disadvantages of CPs include the fact that ion diffusion is relatively slow and so the actuation speed is slow. The actuation speed can be optimized by minimizing the film thickness; however, this often results in a decreased actuator force. The ionic conductivity is also a parameter that can be increased to improve actuator speed. Delamination of CP films can also hinder their performance as an actuator. The extensional strain of CPs (i.e., not in bending) is not very large, which mimics the operating mode for natural muscles. Finally, degradation due to electrochemical over-oxidation is another disadvantage that can arise when using a CP, although this can be avoided by controlling the applied potential.

One of the greatest hindrances to the use of EAPs (ionic or electronic) in MEMS is the relatively low actuation force generated. One avenue used to improve performance is to incorporate a reinforcement phase. Various substrates have been suggested for this purpose, for example, the use of flexible metal films to create bilayer or sandwich structures, embedding nanoscale particles (such as the incorporation of multi-walled carbon nanotubes), or creating interpenetrating composites from polymer networks or nanoporous metals.

Nanoporous metals are favourable for several reasons [164]. Their porous, bi-continuous nature allows for the unhindered transport of ions through the polymer phase. These favourable flow paths would facilitate relatively fast actuation speeds. The complex interconnectedness of the two phases suggests a smaller possibility of delamination

compared to film or sandwich structures. Nanoporous metals would also support deformation in every direction, thus allowing for the possibility of various modes of actuation. Compared to the incorporation of nanoparticles and creation of interpenetrating polymer networks, nanoporous metals also provide greater mechanical robustness.

There have been a few experimental investigations into the actuation responses of nanoporous gold. Wang et al. [165] deposited a film of polypyrrole onto the surface of nanoporous gold and achieved a strain amplitude of 0.19% when placed in an electrolytic solution. Detsi et al. [166] achieved a strain of 0.15% with polyaniline covering the ligaments in a nanoporous gold material.

Pure nanoporous gold has also shown to undergo electrically induced strain [72, 167]. This strain is caused by a charge build-up on the surface of the gold which induces a surface stress [7, 168, 169]. Unfortunately, by coating this surface with a conductive polymer, a charge build-up on the surface is now prevented and so this actuation mechanism is no longer available [166, 170].

4.2 Theory

The behaviour of conductive polymers is modelled as a coupled problem involving mass (ion) transport, electrostatics and deformation [156, 171, 172]. There are three forms of coupling: electro-mechanical, chemo-mechanical and chemo-electric fields (Figure 4.3).

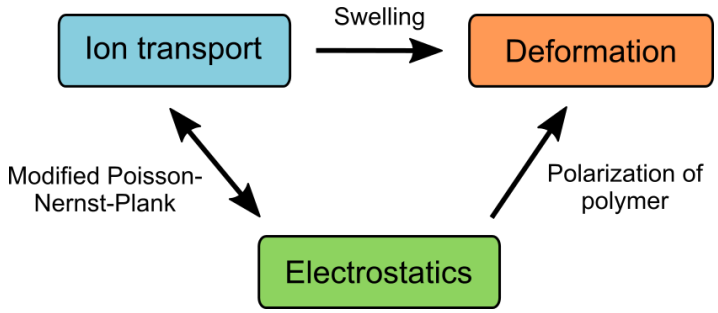

Fig. 4.3: Coupled multi-physics problem within conductive polymers.

Electro-mechanical coupling is a result of polarization of the polymer. This causes an extension of cross linked chains within the polymer and hence deformation. Mass transport is coupled to the deformation as the movement of ions and their mixing within the polymer causes it to either expand or contract [156]. Finally, the coupling between

the ion transport and the evolution of the electric field (chemo-electric coupling) is modelled using a Poisson-Nernst-Planck (PNP) framework where the Nernst-Planck equation describes the motion of a charged chemical species in a fluid [173] due to diffusion and migration. This is combined with Poisson's equation (i.e., Gauss's law for an electric field).

In conductive polymers, elastic waves are approximately five orders of magnitude slower than electromagnetic waves [174]. Compared to the mechanisms in the polymer relating to ion transport and deformation these are very slow. Hence the effects due to the magnetic fields are neglected. Additionally, only small strains are considered in this work.

Numerical modelling of a material requires, firstly, for the governing equations of each primary field to be defined. Secondly, for the constitutive relations that describe the behaviour in terms of the primary variables must be detailed and finally the problem must be fully defined with the prescription of boundary and initial conditions.

4.2.1 Governing equations

Chemo-electro-mechanical behaviour is described in terms of three primary fields: displacement $\boldsymbol{u}$, electrostatic potential ϕ^{e} and the ion concentration field c in a body Ω [156, 171, 172]. The three governing equations are as follows:

Mechanical behaviour

Mechanical behaviour is governed by balance of linear moment law and occurs throughout the composite:

$$\rho \ddot{\boldsymbol{u}} = \operatorname{div} \boldsymbol{\sigma} + \boldsymbol{b} \quad \text{in} \quad \Omega \,. \tag{4.3}$$

Electrostatic behaviour

Electric behaviour is governed by Gauss's law

$$-\operatorname{div} \mathfrak{d} + F \left[zc - c_{\mathrm{ini}} \right] = 0 \quad \text{in} \quad \Omega \,. \tag{4.4}$$

The electric displacement field $\mathfrak{d}$ for a electrically linear and isotropic material is given by

$$\mathfrak{d} = \epsilon_0 \epsilon_\mathrm{r} \mathfrak{e} \,. \tag{4.5}$$

Here, ϵ_0 denotes the absolute permittivity constant (in a vacuum), ϵ_r defines the relative permittivity of the material, and the electric field $\mathfrak{e}$ is classically defined in terms of the electric potential ϕ^e by

$$\mathfrak{e} = -\mathrm{grad}\, \phi^e \,. \tag{4.6}$$

The second term in (4.4) refers to the total charge density made up of free charges where F is Faraday's constant and $zc - c_\mathrm{ini}$ is the difference between the initial ion concentration and the charge density of mobile ions in the polymer. z is the charge number or valance of the ion.

Ion transport

The equation governing the transport of an ion species within the polymer is given by

$$\dot{c} = -\mathrm{div}\, \boldsymbol{j} + w \quad \text{in} \quad \Omega \,. \tag{4.7}$$

Here, $\boldsymbol{j}$ and w are the flux and the source term, respectively.

4.2.2 Constitutive equations

In a metal/polymer composite the body Ω comprises a metal part Ω_M and a polymer part Ω_P such that $\Omega = \Omega_M \cup \Omega_P$. The constitutive equations are based on those proposed by Wilmers et al. [6]. As our attention is confined to small strains, linearizations of the equations proposed by Wilmers et al. [6] are used. The constitutive equations for each part of body Ω are defined through a free energy function.

Metal part

In the metal component only a purely mechanical response will be considered. Thus only the balance of linear momentum equation is of relevance in this phase. The Helmholtz free energy for an isotropic and linear elastic material is given by

$$\rho\psi(\boldsymbol{\varepsilon}) = \mu \boldsymbol{\varepsilon} : \boldsymbol{\varepsilon} + \frac{1}{2}\lambda[\mathrm{tr}\boldsymbol{\varepsilon}]^2 \,, \tag{4.8}$$

in which μ and λ denote the Lamé parameters. The total stress within this phase is thus given by

$$\boldsymbol{\sigma} = \frac{\partial \rho\psi}{\partial \boldsymbol{\varepsilon}} = 2\mu\boldsymbol{\varepsilon} + \lambda[\mathrm{tr}\boldsymbol{\varepsilon}]\boldsymbol{I} \,. \tag{4.9}$$

Polymer part

The polymer phase, on the other hand, is governed by the full chemo-electro-mechanical coupled problem. The Helmholtz free energy is additively decomposed into parts: mechanical ψ^u, electro-mechanical ψ^ϕ, and chemo-mechanical ψ^c:

$$\psi(\boldsymbol{\varepsilon}, \mathfrak{d}, c) = \psi^u(\boldsymbol{\varepsilon}) + \psi^\phi(\boldsymbol{\varepsilon}, \mathfrak{d}) + \psi^c(\boldsymbol{\varepsilon}, c)\,. \tag{4.10}$$

The mechanical part is given by (4.8).

The polymer is assumed to be an isotropic and electrically linear dielectric material, so that the electro-mechanical energy is given by

$$\rho\psi^\phi(\boldsymbol{\varepsilon}, \mathfrak{d}) = \frac{1}{\epsilon_0\epsilon_\mathrm{r}}\left[[\mathfrak{d}\otimes\mathfrak{d}] : \boldsymbol{I} + \boldsymbol{\varepsilon} : [\mathfrak{d}\otimes\mathfrak{d}] - \frac{1}{2}\mathrm{tr}\boldsymbol{\varepsilon}\,[\mathfrak{d}\cdot\mathfrak{d}]\right]. \tag{4.11}$$

The chemo-mechanical part is given by

$$\rho\psi^c(\boldsymbol{\varepsilon}, c) = \frac{1}{z}kF\,[zc - c_\mathrm{ini}]\,\mathrm{tr}\boldsymbol{\varepsilon} + R\theta\left[ln\left(\frac{c}{c_\mathrm{ini}}\right)c - c\right], \tag{4.12}$$

where k is a proportionality constant, R is the gas constant, and θ is the absolute temperature. The energy contribution from the chemo-mechanical part can be seen to comprise two contributions: a part developing as a result of an excess or depletion of ions in a region (first term), and a part that accounts for the mixing of ions within the polymer network (second term). Only the mechanics terms have been linearized due to the assumption of small strains thus the second term has not been linearized, doing so would remove the effects of the mixing of ions.

From this form of the Helmholtz free energy (4.10) the full Cauchy stress $\boldsymbol{\sigma}^\mathrm{total}$ is decomposed into contributions from mechanical $\boldsymbol{\sigma}$, electro-mechanical $\boldsymbol{\sigma}^\phi$, and chemo-mechanical $\boldsymbol{\sigma}^c$ components:

$$\begin{aligned}\boldsymbol{\sigma}^\mathrm{total} = \frac{\partial\rho\psi}{\partial\boldsymbol{\varepsilon}} &= \boldsymbol{\sigma} &&+\boldsymbol{\sigma}^\phi &&+\boldsymbol{\sigma}^c\\ &= 2\mu\boldsymbol{\varepsilon} + \lambda\mathrm{tr}\boldsymbol{\varepsilon}\boldsymbol{I} &&+\frac{1}{\epsilon_0\epsilon_\mathrm{r}}\left[\mathfrak{d}\otimes\mathfrak{d} - \frac{1}{2}[\mathfrak{d}\cdot\mathfrak{d}]\,\boldsymbol{I}\right] &&-\frac{1}{z}kF\,[zc - c_\mathrm{ini}]\,\boldsymbol{I}\,.\end{aligned} \tag{4.13}$$

Here the electro-mechanical contribution is associated with the Maxwell stress induced by an applied electric field, and the chemo-mechanical contribution is associated with ion accumulation. The chemo-mechanical contribution, as explained in [6] and [156], arises from molecular interactions of ions in regions of high or low concentrations due

to the imbalance of charge density.

The total electric field is also split into two contributions based on the constitutive relation given by (4.11): a part $\mathfrak{e}^M$ associated with the electric field according to Maxwell's first equation of electrostatics, and a part $\mathfrak{e}^u$ developing from the applied deformation. Thus

$$\begin{aligned}\mathfrak{e} = \frac{\partial \rho\psi}{\partial \mathfrak{d}} = \ & \mathfrak{e}^M \ + \mathfrak{e}^u \\ & = \frac{1}{\epsilon_0\epsilon_\mathrm{r}}\mathfrak{d} + \frac{1}{\epsilon_0\epsilon_\mathrm{r}}\left[\boldsymbol{\varepsilon}\cdot\mathfrak{d} - \mathfrak{d}\ \mathrm{tr}\boldsymbol{\varepsilon}\right] . \end{aligned} \tag{4.14}$$

For small deformations $\mathfrak{e}^u \approx 0$ and so is neglected here. Making use of (4.6) the electric displacement within the polymer is given by

$$\mathfrak{d} = -\epsilon_0\epsilon_\mathrm{r}\mathrm{grad}\,\phi^\mathrm{e} . \tag{4.15}$$

The classic Nernst-Planck equation to describe the flux of ions in the polymer is derived from a chemical potential of mixing given by

$$\mu^\mathrm{mix} = \phi^\mathrm{e}Fz + \frac{\partial\psi}{\partial c} = Fz\left[\phi^\mathrm{e} + \frac{k}{z}\mathrm{tr}\boldsymbol{\varepsilon}\right] + R\theta\ ln\left(\frac{c}{c_\mathrm{ini}}\right) . \tag{4.16}$$

Using the general relation

$$\boldsymbol{j} = -\frac{c}{R\theta}\mathrm{D}\,\mathrm{grad}\,\mu^\mathrm{mix} , \tag{4.17}$$

where D is the diffusion constant for the polymer and neglecting any dependence on the deformation state of the material, (4.16) and (4.17) yield

$$\boldsymbol{j} = -\mathrm{D}\left[\mathrm{grad}\,c + c\frac{zF}{R\theta}\mathrm{grad}\,\phi^e\right] . \tag{4.18}$$

Here the flux comprises two terms: The first term is a flux driven by the concentration gradient of the ions and hence represents a flux due to diffusion. The second term is a flux driven by the electric potential gradient and represents a flux due to migration due to the need for electro-neutrality within the polymer.

Using (4.18), there exists a possibility for non-physical concentration values to be produced. This is because the size and volume of the polymer chains and ions are not accounted for. Treating these entities as infinitely small points allows for concentrations to increase indefinitely above realistic limits. In the real material, however, this is obviously not the case. There exists a saturation point within the polymer after which

no more ions can be accommodated. To this end, a modification now given to (4.18) proposed by Schlake [175] accounts for the limited amount of available volume into which ions can diffuse.

Three components contribute to the total volume V_{total}: the solvent material (fixed polymer chains and ions), mobile ions, and available space into which ions can move. The volume density fraction of the mobile ion species at a material point is given by

$$\frac{V_{\text{ions}}}{V_{\text{total}}} = v_{\text{ions}} = \frac{4}{3}\pi N_A R_{\text{ions}}^3 c\,, \tag{4.19}$$

where R_{ions} is the radius of an individual ion species and N_A is Avogadro's constant. The volume fraction of available space is thus given by

$$v_o = 1 - \left[v_{\text{ions}} + v_{\text{solvent}}\right], \tag{4.20}$$

where v_{solvent} is the volume density fraction of the solvent material.

This results in a modification to the ion flux $\boldsymbol{j}$, which becomes [1]

$$\boldsymbol{j} = -\mathrm{D}\left[v_o \operatorname{grad} c + c\frac{zF}{R\theta} v_o \operatorname{grad}\phi^{\mathrm{e}} + c \operatorname{grad} v_{\text{ions}} + \frac{1}{R\theta} c v_o \operatorname{grad} W_i\right]. \tag{4.21}$$

W_i can represent an externally applied potential; however, no additional external potentials other than the electric potential are applied here and so this term and its gradient $\operatorname{grad} W_i$ vanish.

As the volume of available space decreases with ions moving into it $v_o \to 0$ with $v_o = 0$ representing a fully saturated state.

The concentration fields of four test cases of this modification are shown in Figure 4.4. Here the polymer phase includes mobile ions and an electric field is applied across the polymer. The movement of the mobile ions is initiated by the electric potential gradient (i.e., migration of ions to establish electro-neutrality in the polymer) after which both diffusion and migration contribute to the movement.

In all four cases, saturation is clearly seen in the modified case, compared to the unmodified case. The unmodified cases also all reached significantly larger maximum concentration values compared to their modified counterparts. Additionally, the effects of

[1] Details on the derivation of this modified flux term can be found in [175].

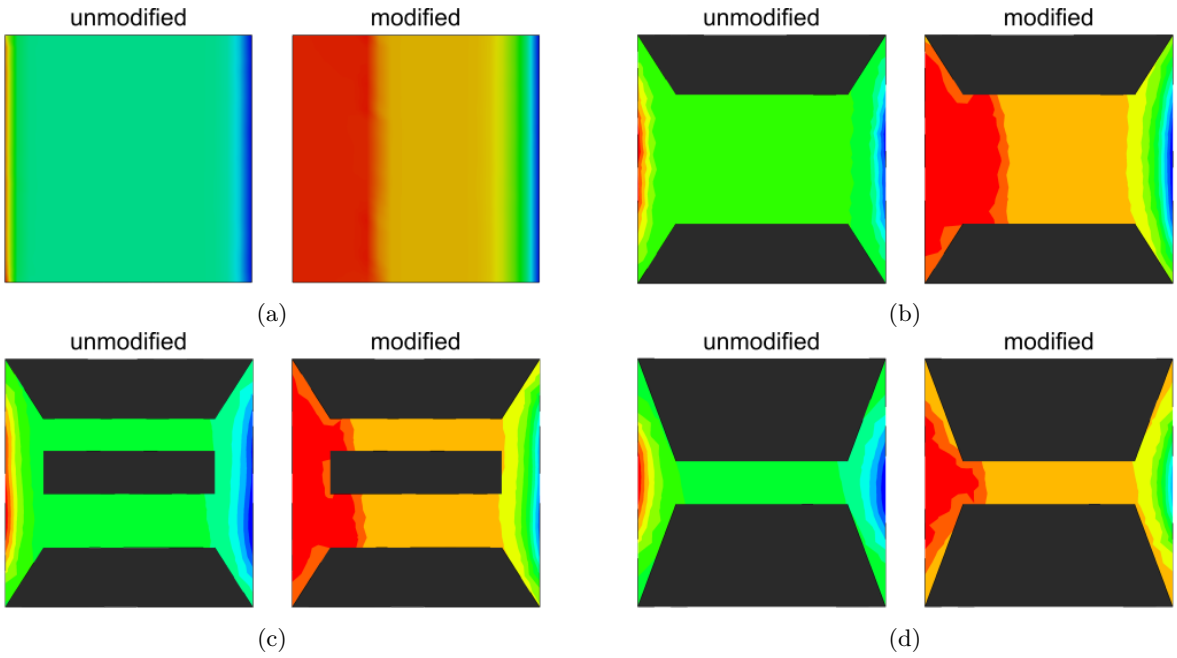

Fig. 4.4: Four test cases to show the effects of the modification made to the classic Nernst-Planck equation. The modification presented in (4.21) shows that the effects of saturation and crowding is captured. Regions of a high and low concentration of ions are indicated by red and blue regions respectively. It should be noted that for each test case the maximum value of ion concentration for the modified cases was significantly lower than that of the unmodified case.

ion crowding can also be seen, most notably in Figure 4.4(c), where the saturated concentration region extends further into the larger (lower) pore compared to the smaller (upper) pore. Crowding of ions at the entrance to the pore has created a slight bottleneck effect. This is also seen when comparing the extent of the saturated concentration regions in the larger pore of Figure 4.4(b), compared with the smaller pore of Figure 4.4(d).

4.2.3 Summary

The governing equations together with boundary conditions and initial conditions are summarised in Tables 4.1 and 4.2.

Table 4.1: Equations governing the three fields within the conductive polymer

Deformation	$\rho\ddot{\boldsymbol{u}} = \operatorname{div}\left(2\mu\boldsymbol{\varepsilon} + \lambda\left[\operatorname{tr}\boldsymbol{\varepsilon}\right]\boldsymbol{I} + \frac{1}{\epsilon_0\epsilon_\mathrm{r}}\left[\mathfrak{d}\otimes\mathfrak{d} - \frac{1}{2}\left[\mathfrak{d}\cdot\mathfrak{d}\right]\boldsymbol{I}\right] - \frac{1}{z}kF\left[zc - c_\mathrm{ini}\right]\boldsymbol{I}\right)$
Electrostatic	$0 = \operatorname{div}\left(\epsilon_0\epsilon_\mathrm{r}\operatorname{grad}\phi^\mathrm{e}\right) + F\left[zc - c_\mathrm{ini}\right]$
Ion transport	$\dot{c} = -\mathrm{D}\operatorname{div}\left(v_o\operatorname{grad}c + c\frac{zF}{R\theta}v_o\operatorname{grad}\phi^\mathrm{e} + c\operatorname{grad}v_\mathrm{ions}\right)$

Table 4.2: Boundary and initial conditions of the conductive polymer

	Boundary conditions		Initial condition
Deformation	$\boldsymbol{u}\vert_{\partial\Omega_u} = \bar{\boldsymbol{u}}$,	$\boldsymbol{\sigma n}\vert_{\partial\Omega_n} = \bar{\boldsymbol{t}}$	$\boldsymbol{u}_{t=0} = \boldsymbol{0}$
Electrostatic	$\phi^e\vert_{\partial\Omega_u} = \bar{\phi}^e$,	$\mathfrak{e}\cdot\boldsymbol{n}\vert_{\partial\Omega_n} = \bar{\mathfrak{e}}$	–
Ion transport	$c\vert_{\partial\Omega_u} = \bar{c}$,	$\boldsymbol{j}\cdot\boldsymbol{n}\vert_{\partial\Omega_n} = \bar{j}$	$c_{t=0} = c_\mathrm{ini}$

4.3 Finite element model

4.3.1 Model description

The chemo-electro-mechanical response of a gold/polymer nanocomposite is modelled here to investigate the effects of the volume fraction of metal on the evolution of the three primary fields. Additionally, details of the micromechanical response are also probed. This investigation is conducted on four RVEs with gold volume fractions of 25, 34, 42 and 50%. These RVEs were generated using the level set method as described in Section 1.3. These RVEs were meshed with $96 \times 96 \times 96$ voxel elements. Computations were performed using facilities provided by the University of Cape Town's ICTS High Performance Computing team (hpc.uct.ac.za). The polymer used is a perchlorate-doped polypyrrole ($\mathrm{PPy/ClO_4^-}$) where perchlorate anions act as the transported anions. The material parameters for both the gold and polymer material are given in Table 4.3.

4.3.2 Boundary conditions

The RVEs here are considered to be small samples of the gold/polymer nanocomposite material that make up a working electrode within an electrolytic cell as shown in Figure 4.5.

Using the equations given in Table 4.1, a local chemo-electro-mechanical response to the

Table 4.3: Table of material parameters for gold and polypyrrole

	Symbol	Value
Gold		
Mass density	ρ	19.3 g/cm^3 [176]
Lamé parameters	λ	198.6 GPa [177]
	μ	27.08 GPa [177]
Polypyrrole		
Mass density	ρ	1.47 g/cm^3 [178]
Lamé parameters	λ	0.346 GPa [27]
	μ	0.231 GPa [27]
Absolute permittivity	ϵ_0	$8.854{\cdot}10^{-12}$ F/m
Relative permittivity	ϵ_r	10000 [176]
Faraday's constant	F	96485.337 C/mol
Valence mobile species	z	-1 [176]
Electro-mechanical coupling parameter	k	50 J/C [156]
Diffusivity	D	$10{\cdot}10^{-10}$ m^2/s [176]
Initial ion concentration	c_ini	$1.3{\cdot}10^2$ mol/m^3
Mobile anion radius	R_ions	0.240 nm [179]
Solvent volume fraction density	v_solvent	0.67 [180]
Avogadro's constant	N_A	$6.02214{\cdot}10^{23}$ mol^{-1}

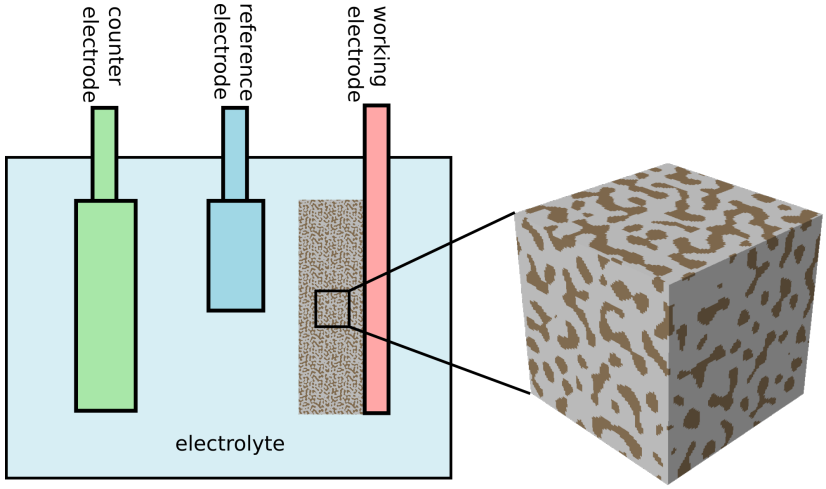

Fig. 4.5: Schematic depiction of the electrolytic cell set-up with a gold/polymer nanocomposite acting at the working electrode in order to undergo electrically induced deformation. [2]

electrical stimulus is modelled in the RVE. It is important for the boundary conditions to be able to represent the global response of the macroscopic material into which it is embedded. To assist with the description of application of the boundary conditions,

[2] Reproduced with permission from Elsevier (https://doi.org/10.1016/j.jmps.2019.103848)

the conventions of a RVE with faces and normals labelled as in Figure 4.6 will be used throughout.

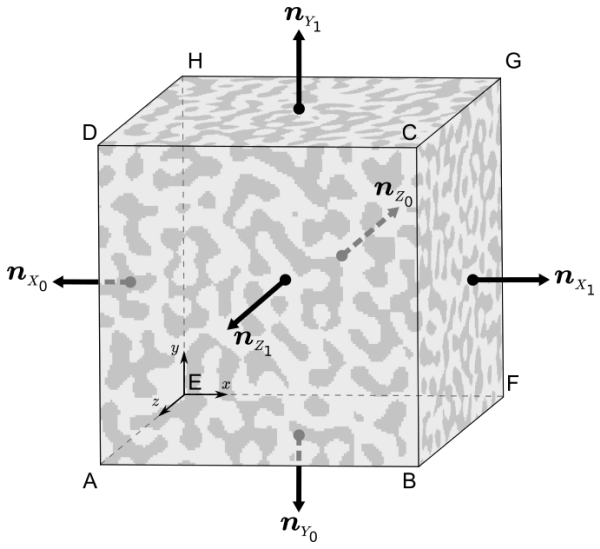

Fig. 4.6: Description of the normal vectors and face naming convention used to describe the boundary conditions applied to the RVE. The faces are defined by the following vertices: X_0 – EADH, X_1 – BFGC, Y_0 – AEFB, Y_1 – DCGH, Z_0 – ABCD, Z_1 – EFGH.[3]

Electrostatics

The boundary conditions applied to the electric field are shown in Figure 4.7. A linear potential gradient is applied across the RVE by applying Dirichlet boundary conditions $\phi^e = -1.00\,\mathrm{V}$ and $\phi^e = +1.00\,\mathrm{V}$ on sides X_0 and X_1 respectively. Neumann boundary conditions are applied on all remaining faces (Y_0, Y_1, Z_0, Z_1), that is, $\mathfrak{e} = \mathbf{0}$.

Ion transport

The ion transport is driven by both the concentration gradient as well as the potential gradient. As a uniform concentration is assumed at the start, it is only the electric potential, applied as described in the previous section, that generates ion flux in the direction of the potential gradient. Neumann boundary conditions are set with $\boldsymbol{j} = \mathbf{0}$ on faces Y_0, Y_1, Z_0 and Z_1.

[3] Reproduced with permission from Elsevier (https://doi.org/10.1016/j.jmps.2019.103848)
[4] Reproduced with permission from Elsevier (https://doi.org/10.1016/j.jmps.2019.103848)

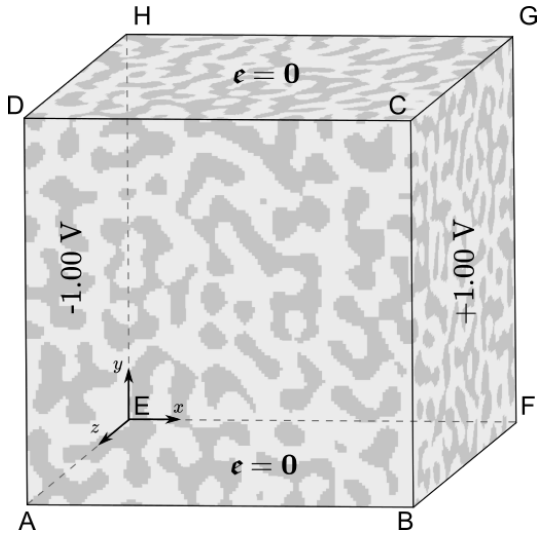

Fig. 4.7: Schematic depiction of the electrostatic boundary conditions used. [4]

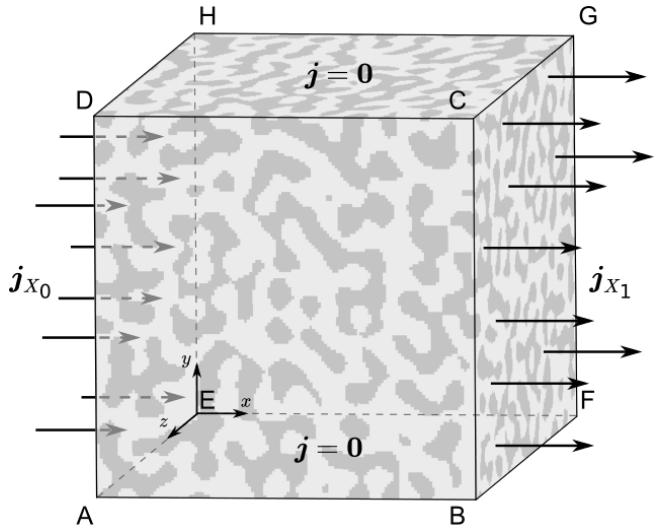

Fig. 4.8: Schematic depiction of the ion transport boundary conditions used. [5]

On the remaining two faces the influx and efflux of ions occurs with influx occurring on the X_0 face and efflux occurring on the X_1 face (See Figure 4.8). The application of the electric potential and hence the creation of a potential gradient causes oxidation to occur within the polymer. This oxidation causes the polymer no longer to be electrically neutral, which results in an influx of ions to balance the charge. The influx on face X_0 is thus given by

$$\boldsymbol{j}_{X_0} = -\frac{zF}{R\theta} c v_o \mathrm{D} \operatorname{grad} \phi^e \,. \tag{4.22}$$

As this is an embedded RVE in a larger material sample, the efflux of ions from the RVE (and into another section of the nanocomposite) will still be occurring on the X_1 face. Within the RVE, the balance of mass in this control volume still needs to be

[5] Reproduced with permission from Elsevier (https://doi.org/10.1016/j.jmps.2019.103848)

maintained. By integrating (4.7) over the domain the mass balance in the RVE is given by

$$\int_{\Omega} \dot{c}\,\mathrm{dV} = -\int_{\Omega} \operatorname{div} \boldsymbol{j}\,\mathrm{dV}. \tag{4.23}$$

The use of the divergence theorem on the right-hand-side of (4.23) yields

$$\int_{\Omega} \dot{c}\,\mathrm{dV} = -\int_{\partial\Omega} \boldsymbol{j}\cdot\boldsymbol{n}\,\mathrm{dA}. \tag{4.24}$$

As zero flux boundary conditions have been prescribed on faces Y_0, Y_1, Z_0 and Z_1, the right-hand side of (4.24) is simplified to read

$$\int_{\Omega} \dot{c}\,\mathrm{dV} = -\int_{\mathrm{A}_{X_0}} \boldsymbol{j}\cdot\boldsymbol{n}\,\mathrm{dA} - \int_{\mathrm{A}_{X_1}} \boldsymbol{j}\cdot\boldsymbol{n}\,\mathrm{dA}, \tag{4.25}$$

where $\mathrm{A}_{(\cdot)}$ is the polymer surface area on the $(\bullet)$ face. The term on the left-hand side can be calculated by summing the rate of change in concentration at each node from the last time increment. The first term on the right-hand side arises from the influx of ions, which is also known as it is prescribed by (4.22). The efflux (given by the second term on the right-hand side) can thus be calculated by rearranging (4.25) and evaluating the integrals to give

$$\boldsymbol{j}\cdot\boldsymbol{n}|_{\mathrm{A}_{X_1}} = -\frac{\displaystyle\int_{\Omega} \dot{c}\,\mathrm{dV} + \boldsymbol{j}\cdot\boldsymbol{n}|_{\mathrm{A}_{X_0}}\mathrm{A}_{X_0}}{\mathrm{A}_{X_1}}. \tag{4.26}$$

Mechanical conditions

To simulate the global response of the surrounding material a form of mixed boundary conditions is used. The resistance of the adjacent material is accounted for by assuming a spring on these faces (see Figure 4.9) such that the traction at the external faces is given by

$$\boldsymbol{\sigma}\boldsymbol{n} = p\,\boldsymbol{u}\,, \tag{4.27}$$

where p is a spring constant. As $p \to 0$ the boundary mimics a traction free Neumann boundary and as $p \to \infty$ a zero displacement Dirichlet boundary is enforced.

4.3.3 Finite element implementation

Multiplying (4.3), (4.4), and (4.7) by test functions $\delta\boldsymbol{u}$, $\delta\phi^{\mathrm{e}}$, and δc_0, respectively which satisfy the homogeneous Dirichlet boundary conditions, applying the divergence theorem and introducing the Neumann boundary conditions the following weak formulation

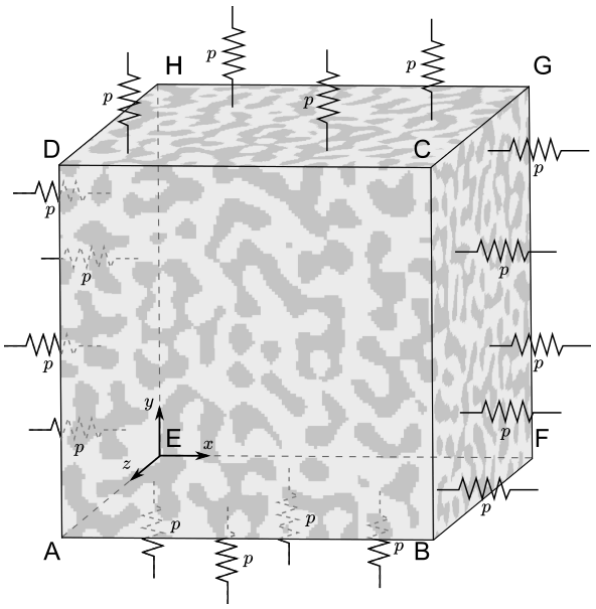

Fig. 4.9: Schematic depiction of the mechanical boundary conditions used. [6]

of the problem is obtained:

$$\int_\Omega \rho\delta\boldsymbol{u}\cdot\ddot{\boldsymbol{u}}\,\mathrm{dV}+\int_\Omega \boldsymbol{\sigma}:\mathrm{grad}\,\delta\boldsymbol{u}\,\mathrm{dV}-\int_\Omega \delta\boldsymbol{u}\cdot\boldsymbol{b}\,\mathrm{dV}-\int_{\partial\Omega}\delta\boldsymbol{u}\cdot(\boldsymbol{\sigma}\boldsymbol{n})\,\mathrm{dA}=0\,; \tag{4.28}$$

$$-\int_\Omega \epsilon_0\epsilon_\mathrm{r}\boldsymbol{\mathfrak{e}}\cdot\mathrm{grad}\,\delta\phi^\mathrm{e}\,\mathrm{dV}-\int_\Omega \delta\phi^\mathrm{e}F[c-c_\mathrm{ini}]\,\mathrm{dV}+\int_{\partial\Omega}\delta\phi^\mathrm{e}\,\epsilon_0\epsilon_\mathrm{r}\boldsymbol{\mathfrak{e}}\cdot\boldsymbol{n}\,\mathrm{dA}=0\,; \tag{4.29}$$

$$\int_\Omega \delta c_0\,\dot{c}_0\,\mathrm{dV}-\int_\Omega \boldsymbol{j}\cdot\mathrm{grad}\,\delta c_0\,\mathrm{dV}-\int_\Omega \delta c_0\,w\,\mathrm{dV}+\int_{\partial\Omega}\delta c_0\,\boldsymbol{j}\cdot\boldsymbol{n}\,\mathrm{dA}=0\,. \tag{4.30}$$

The same polynomial degree of interpolation is adopted for all variables, so that

$$\boldsymbol{u}(\boldsymbol{X})=\sum_{I=1}^{\mathrm{Nen}}N^I(\boldsymbol{X})\boldsymbol{u}^I,\quad \phi^\mathrm{e}(\boldsymbol{X})=\sum_{I=1}^{\mathrm{Nen}}N^I(\boldsymbol{X})\phi^{\mathrm{e}\,I}\quad\text{and}\quad c_0(\boldsymbol{X})=\sum_{I=1}^{\mathrm{Nen}}N^I(\boldsymbol{X})c_0^I\,, \tag{4.31}$$

where $N^I(\boldsymbol{X})$ are the elemental shape functions and $\boldsymbol{u}^I,\phi^{\mathrm{e}\,I}$ and c_0^I are the nodal degrees of freedom associated with the displacement, electrostatic and ion concentration field.

With these substitutions (4.28) becomes

$$\boldsymbol{M}^{IJ}\ddot{\boldsymbol{u}}^J+\boldsymbol{R}_u^I=\boldsymbol{P}_u^I\,,\quad\text{with}\quad(I,J=1,...,\mathrm{N_{en}}) \tag{4.32}$$

[6] Reproduced with permission from Elsevier (https://doi.org/10.1016/j.jmps.2019.103848)

where $\boldsymbol{M}$, $\boldsymbol{R}_u$, and $\boldsymbol{P}_u$ are the mass matrix, the internal force vector, and the external force vector respectively. In component form,

$$\begin{aligned} \boldsymbol{M}^{IJ} &= \rho \int_\Omega N^I N^J \,\mathrm{dV}\,; \\ \boldsymbol{R}_u^I &= \int_\Omega \boldsymbol{\sigma} \mathrm{grad}\, N^I \,\mathrm{dV} - \int_{\partial\Omega} N^I \boldsymbol{\sigma}\boldsymbol{n} \,\mathrm{dA}\,; \\ \boldsymbol{P}_u^I &= \int_\Omega N^I \boldsymbol{b} \,\mathrm{dV}. \end{aligned} \tag{4.33}$$

Similarly, (4.30) becomes

$$\boldsymbol{D}^{IJ}\dot{\boldsymbol{c}}^J + \boldsymbol{R}_c^I = \boldsymbol{P}_c^I\,, \tag{4.34}$$

where $\boldsymbol{D}$, $\boldsymbol{R}_c$ and $\boldsymbol{P}_c$ are the mass permittivity matrix, the internal flux vector and the external source vector, respectively. Their nodal representation is

$$\begin{aligned} \boldsymbol{D}^{IJ} &= \int_\Omega N^I N^J \,\mathrm{dV}\,; \\ \boldsymbol{R}_c^I &= -\int_\Omega \boldsymbol{j} \cdot \mathrm{grad}\, N^I \,\mathrm{dV} + \int_{\partial\Omega} N^I \boldsymbol{j}\cdot\boldsymbol{n} \,\mathrm{dA}\,; \\ \boldsymbol{P}_c^I &= \int_\Omega N^I w \,\mathrm{dV}. \end{aligned} \tag{4.35}$$

Accordingly, the first law of electrostatics in its discretized form at the local nodal level is written as

$$\boldsymbol{K}_\phi^{IJ}\boldsymbol{\phi}^{\mathrm{e}\,J} = \boldsymbol{P}_\phi^I, \tag{4.36}$$

where $\boldsymbol{K}_\phi$ and $\boldsymbol{P}_\phi$ are the stiffness matrix and the external source vector, respectively. At the nodal level they read

$$\begin{aligned} \boldsymbol{K}_\phi^{IJ} &= \int_\Omega \epsilon_0\epsilon_\mathrm{r} \mathrm{grad}\, N^I \mathrm{grad}\, N^J \,\mathrm{dV}\,; \\ \boldsymbol{P}_\phi^I &= \int_\Omega F \left[\sum_{K=1}^{\mathrm{Nen}} N^K c^K - c_\mathrm{ini}\right] N^I \,\mathrm{dV} - \int_{\partial\Omega} N^I \epsilon_0\epsilon_\mathrm{r}\boldsymbol{\mathfrak{e}}\cdot\boldsymbol{n} \,\mathrm{dA}\,. \end{aligned} \tag{4.37}$$

The relations for $\boldsymbol{\sigma}, \boldsymbol{j}$ and $\boldsymbol{\mathfrak{e}}$ to their respective primary field variables are given by (4.13), (4.21) and (4.6).

Solution method

Implicit method

Using a time independent method, (4.36) is solved within ABAQUS/STANDARD. As the electro static problem is linear with respect to ϕ^e, the problem is of the form

$$\boldsymbol{K}_\phi \boldsymbol{d} = \boldsymbol{P}_\phi \,, \tag{4.38}$$

where $\boldsymbol{K}_\phi$ and $\boldsymbol{P}_\phi$ are given by (4.37) and $\boldsymbol{d} = \boldsymbol{\phi}^{\mathrm{e}\,J}$.

Explicit methods

The equations (4.32) and (4.34) are solved using an explicit time integration scheme within ABAQUS/EXPLICIT. Although the time-scale is defined by the slow diffusion process, dynamics are included to allows for an explicit solver to be used as an FE problem of this size would not solvable using the implicit solver of ABAQUS/STANDARD.

Specifically, (4.32) is solved using an explicit central-difference rule. This uses a time stepping scheme where $t_1 < t_2 < ... < t_{\text{end}}$ and the time increment is defined as $\Delta t = t_k - t_{k-1}$. The solution at time $t = t_k$ is represented as $\boldsymbol{u}^I(t_k) = \boldsymbol{u}^I_k$. The kinematic state is advanced to time t_{k+1} using the velocity at time $t_{k+1/2} = t_k + \Delta t/2$ and the acceleration at time t_k.

With the advanced velocity field given by

$$\dot{\boldsymbol{u}}^I_{k+1/2} = \dot{\boldsymbol{u}}^I_{k-1/2} + \frac{\Delta t_{k+1} - \Delta t_{k-1}}{2} \ddot{\boldsymbol{u}}^I_k \,, \tag{4.39}$$

the unknown displacement field at time t_{k+1} is given by

$$\boldsymbol{u}^I_{k+1} = \boldsymbol{u}^I_k + \Delta t_{k+1} \dot{\boldsymbol{u}}^I_{k+1/2} = \boldsymbol{u}^I_k + \Delta t_{k+1} \dot{\boldsymbol{u}}^I_{k-1/2} + \frac{\Delta t^2_{k+1} - \Delta t_{k+1}\Delta t_{k-1}}{2} \ddot{\boldsymbol{u}}^I_k \,, \tag{4.40}$$

where the acceleration at the current time step is determined directly from the discretized equation; that is,

$$\ddot{\boldsymbol{u}}^I_k = \left[\boldsymbol{M}^{IJ}\right]^{-1} \left[\boldsymbol{P}^J_u - \boldsymbol{R}^J_u\right] \,. \tag{4.41}$$

As explicit methods calculate future quantities using quantities calculated only at previous time steps they are conditionally stable. Stability limits on the size of the time step must thus be calculated. The stability limit for this central difference integration scheme is determined from the smallest time it takes for an elastic wave to cross any of

the elements in the mesh. The maximum suitable time step for the central-difference rule is given by

$$\Delta t_{\boldsymbol{u}} = \ell \sqrt{\frac{\rho}{\lambda + 2\mu}}\,, \tag{4.42}$$

where ℓ is the smallest characteristic length of any element within the mesh.

The transport equation (4.34) is analogous to the transient heat equation and is solved using an explicit forward-difference integration scheme, so that the concentration field at time t_{k+1} is found from

$$\boldsymbol{c}_{k+1}^{I} = \boldsymbol{c}_{k}^{I} + \Delta t_{k+1} \dot{\boldsymbol{c}}_{k}^{I}\,. \tag{4.43}$$

Here

$$\dot{\boldsymbol{c}}_{k}^{I} = \left[\boldsymbol{D}^{IJ}\right]^{-1} \left[\boldsymbol{P}_{c}^{J} - \boldsymbol{R}_{c}^{J}\right]\,. \tag{4.44}$$

The maximum stable time increment for this scheme is given by

$$\Delta t_{\boldsymbol{c}} = \frac{\ell^2}{\mathrm{D}}\,. \tag{4.45}$$

The time increment for the simultaneous solution of both fields is chosen so that, from (4.42) and (4.45),

$$\Delta t = \min\left(\Delta t_{\boldsymbol{u}}, \Delta t_{\boldsymbol{c}}\right)\,. \tag{4.46}$$

Staggered explicit-implicit method

In order to solve the three fields using Abaqus, the displacement and transport problem (in Abaqus/Explicit) must be coupled to the electrostatics problem (in Abaqus/Standard) using a staggered method. This involves first solving for the displacement and concentration fields monolithically for n time increments. The Abaqus/Explicit simulation is then paused and the concentration field is imported into Abaqus/Standard, from which the electric potential is obtained. Finally, the resulting electric potential field is imported back into Abaqus/Explicit. The displacement and concentration problem is then calculated for the next n time increments using the new updated electric potential. This is repeated until the end of the simulation is reached. As the electric potential field does not evolve in time with the displacement and concentration problem, the explicit-implicit interfacing needs to occur regularly, often and throughout the simulation. This interfacing is quite time expensive and so is performed every 5 time increments. Using test simulations it was shown that more frequent interfacing did not yield differences in the developing fields. The solution scheme

is summarized in Algorithm 1.

Algorithm 1: Explicit-implicit solution method

Result: Calculation of $\boldsymbol{u}, c, \phi^{\mathrm{e}}$
initialization;
while $t_k < t_{\mathrm{end}}$ **do**
  initialize i;
  for n increments **do**
    Calculate $\boldsymbol{u}, c$ using central-difference scheme in Abaqus/Explicit;
    $i = i + 1$;
    $t_k = t_i$;
  Extract concentration field at $t = t_k$ and import into Abaqus/Standard input file;
  Calculate ϕ^{e} using forward-difference scheme in Abaqus/Standard;
  Extract electrostatic field at $t = t_k$ and import into Abaqus/Explicit;

Four Abaqus subroutines are utilized in order to achieve this:

Uel: This subroutine creates user elements that are defined by non-standard (linear or non-linear) constitutive equations or involve non-standard degrees of freedom. This subroutine is called for each element individually; the material behaviour for that element needs to be defined within the subroutine. This information is then passed to the Abaqus solver. In a linear problem, this process is only required once. Here, a Uel subroutine is created to solve the electrostatic field. It requires the coding of the stiffness matrix $\boldsymbol{K}_{\phi}$ (termed the Jacobian in Abaqus documentation) and the right-hand side vector $\boldsymbol{P}_{\phi}$. The stiffness matrix is a function of the shape function and material parameters while the right-hand side vector involves the shape functions and concentrations which are calculated at the integration points.

Vuel: Similar to the Uel, this subroutine also creates a user-defined element within Abaqus/Explicit. This subroutine is used to solve the concentration and displacement fields using an explicit time scheme. It requires the coding of the mass $\boldsymbol{M}$ and permittivity matrix $\boldsymbol{D}$ for the displacement and concentration problem respectively as well as their respective right-hand side vectors, $\boldsymbol{P}_u - \boldsymbol{R}_u$ and $\boldsymbol{P}_c - \boldsymbol{R}_c$ respectively. This requires the calculation of the concentration, displacement and electric potential as well as their respective gradients at the integration points. These values are used in the relations given by (4.13) and (4.21) to calculate the required vectors and matrices.

The implementation of the boundary conditions is also carried out in this subroutine. For boundary elements, the boundary nodes are identified and boundary conditions are applied. The implementation of the displacement boundary is achieved by multiplying the nodal displacement value by the spring constant p and adding it to the right-hand side vector.

The flux boundary conditions are slightly more difficult to implement. Here the element needs to be categorized as an influx or efflux boundary element (zero flux boundary conditions are automatically assumed and so are not dealt with).

If it is an influx element, concentration on the influx face and electric potential across the element are calculated and the influx given by (4.22) is added to the right-hand side vector.

If it is an efflux element, the rate of change of concentration across the RVE in the previous time increment ($\int_\Omega \dot{c}\,\mathrm{dV}$) and the total influx ($\boldsymbol{j}\cdot\boldsymbol{n}|_{A_{X_0}}$) is read from an external file and (4.26) is added to the right-hand side of that vector. The calculation and writing of the rate of change of concentration and the total influx are also done within the VUEL subroutine.

VEXTERNALDB: This subroutine pauses the ABAQUS/EXPLICIT simulation and allows for external programs to run and dynamically communicate data between these programs. In this method, data needs to be passed to and from ABAQUS/-EXPLICIT and ABAQUS/STANDARD.

Within the VEXTERNALDB subroutine an external shell script is run after n increments in ABAQUS/EXPLICIT. This script facilitates the following:

- Extracts and writes the current concentration field from the explicit simulation of an external file using a Python code;
- Runs the ABAQUS/STANDARD electrostatic problem with this new concentration field;
- Extracts the new electric potential field from the electrostatic problem and writes the data to an external file. This data is then passed to the explicit problem through another subroutine.

In addition to this, the VEXTERNALDB subroutine also assists in calculating and storing the $\int_\Omega \dot{c}\,\mathrm{dV}$ and $\boldsymbol{j}\cdot\boldsymbol{n}|_{A_{X_0}}$ terms necessary for the flux boundary condition calculation.

VUFIELD: This is the final subroutine necessary for the implementation of this staggered explicit-implicit method. This subroutine allows one to prescribe and modify pre-defined field variables. It is thus used here to update the electric field within ABAQUS/EXPLICIT every n increments after the VEXTERNALDB subroutine has extracted it from the electrostatic problem.

The use of subroutines within ABAQUS is summarized in Figure 4.10.

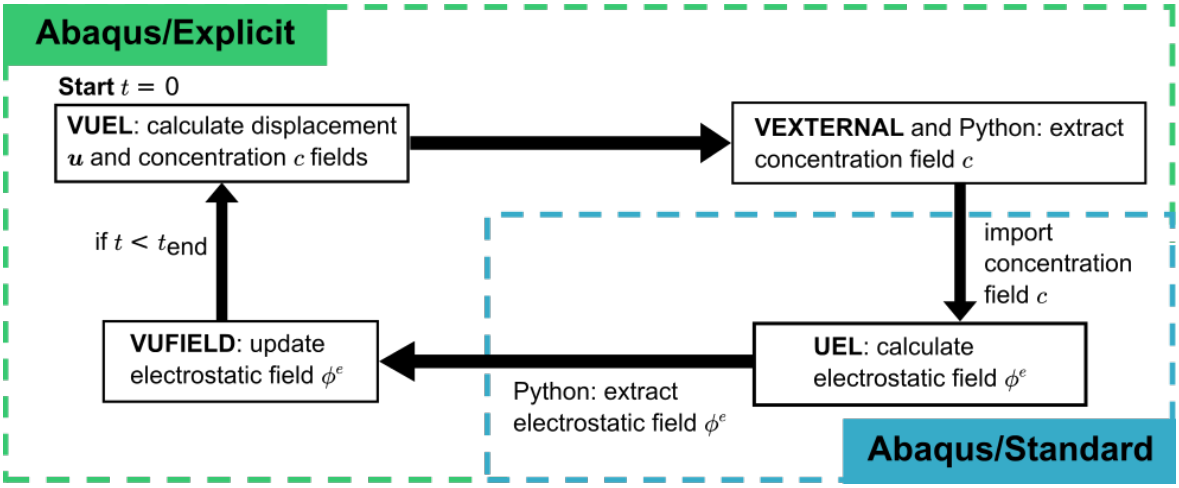

Fig. 4.10: Details of the computational implementation of an staggered explicit-implicit solution scheme used to solve the couple chemo-electro-mechanical problem. [7]

4.4 Results and discussion

The chemo-electro-mechanical response of the four RVEs described in Section 4.3.1 is simulated over 1750 ns using ABAQUS. The resultant fields are probed to investigate possible structure-property relationships that develop in regard to the volume fraction or topological and morphological characteristics of the nanocomposite.

4.4.1 Electrostatic response

The change of the electric potential across the RVEs at the lowest (25%) and highest (50%) gold volume fraction specimens at the beginning and end of the simulation are

[7] Reproduced with permission from Elsevier (https://doi.org/10.1016/j.jmps.2019.103848)

shown in Figure 4.11. A slight shift in the potential over time can be seen in both RVEs. This is due to the presence of the mobile ions that have moved into the polymer constituent. Due to the high electric potential gradient across the RVE (compared to what would be present in a macroscale model) the ions are unable to fully neutralize the charge within the conductive polymer.

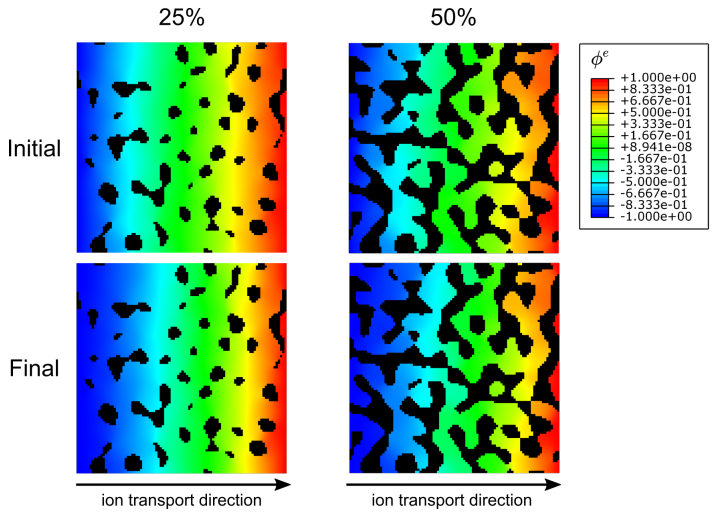

Fig. 4.11: The development of the electric potential field in the 25% and 50% RVEs. A slight shift is noted due to the ions moving into the polymer. The gold material is shown in black.

4.4.2 Ion transport

In Figure 4.12 the development of the concentration field over the simulation is shown for each RVE. Crowding and saturation, as described by the modification to the classic Nernst-Planck equation and shown in the test cases in Figure 4.4, are evident in this figure.

A significant structural-property relationship seen in this figure is a decreasing speed of ion transport as the volume fraction of gold increases. It is clear that the 25% gold volume fraction RVE reaches its equilibrium concentration long before that of the 50% gold volume fraction RVE. This is due to two factors: firstly, as ion transport does not occur within the gold phase the gold ligaments perpendicular to the ion flow direction hinder the ion transport; as the gold volume fraction increases the number of these ligaments increases and so the ion transport is delayed.

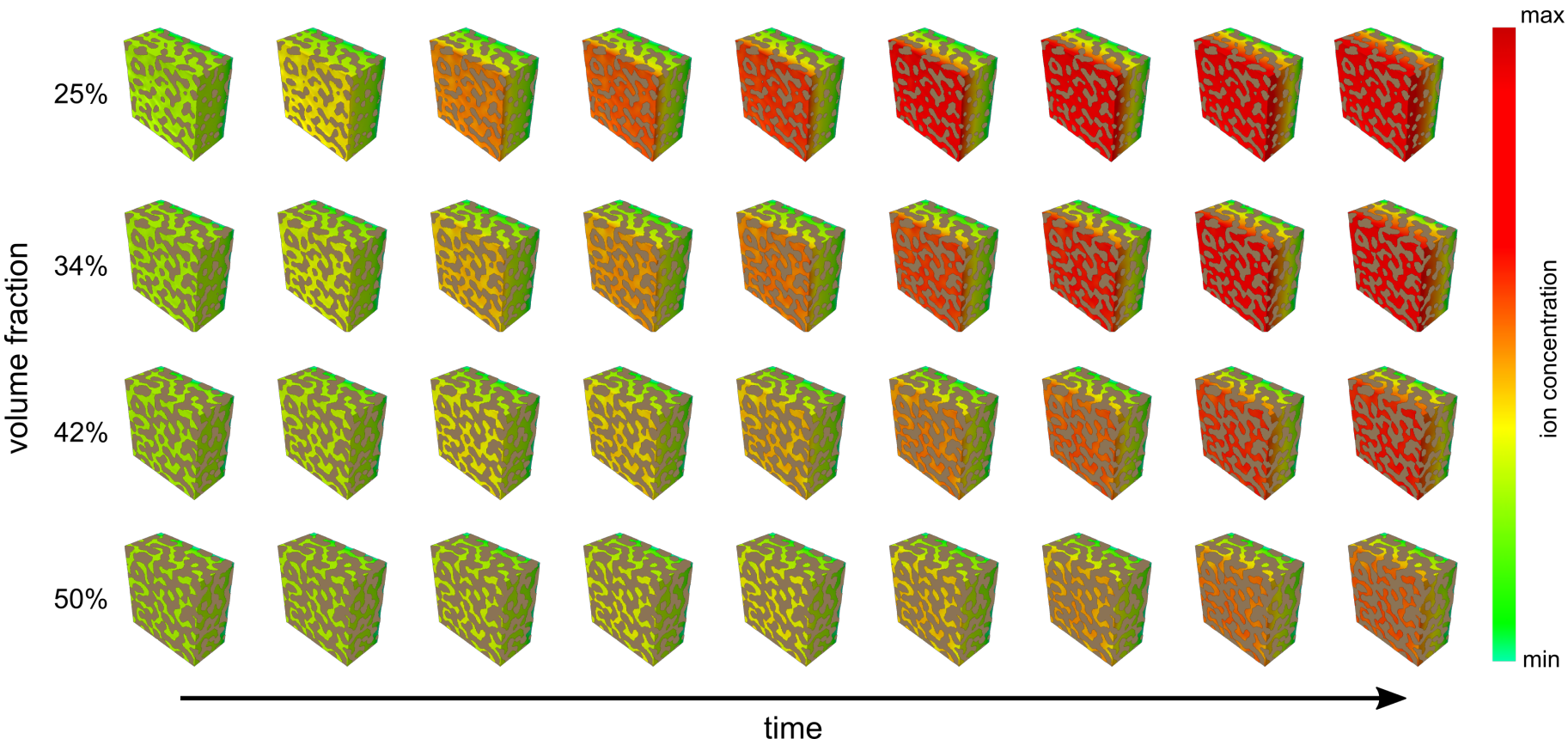

Fig. 4.12: Ion concentration development over time in the polymer phase midway through each RVE. Brown regions represent the metal constituent where no ion transport occurs. It is evident that with increasing metal content the ion transport slows down significantly.[8]

[8] Reproduced with permission from Elsevier (https://doi.org/10.1016/j.jmps.2019.103848)

Secondly, ion transport is affected by the size of the polymer pores through which it travels. Since the diameter of the ligaments increases with an increasing gold volume fraction, the diameter of pore channels would thus decrease. Accordingly the combination of larger gold ligaments and smaller ion transport channels contributes to the slower ion transport through larger volume fraction nanocomposite specimens.

Ion transport is directly linked to the response time of the actuator. That is, fast ion transport will result in a swift actuation response. Thus one needs to consider whether the mechanical benefits of adding more reinforcement to the nanocomposite are more important than the speed of the actuation response. The ability to orientate a significant portion of the ligaments in the direction longitudinal to ion transport in order to minimize the obstruction to ion flux while maintaining a certain volume fraction could present an opportunity to optimize the material to its function as a strong and fast actuator.

Another feature noted in the development of the concentration field is a slightly speckled pattern on the influx face. Areas of relatively higher ion concentration are those where the polymer pore channel is blocked by a gold ligament running perpendicular to the ion flow. In areas of low ion concentration the polymer pore channels are not blocked by gold ligaments and ion movement is unhindered, so that the ions move through the RVE faster and do not pile up at the influx face. The amount of speckling increases with volume fraction.

Figure 4.13 clearly shows two locations within the RVEs where, at the lower volume fractions, there is no hindrance by the gold and thus no build-up of ions, while at the higher volume fractions (42% and 50%) two locations with locally high concentrations are caused by the presence of a perpendicular gold ligament. Due to the bicontinuous nature of the nanocomposite the flow of ions is not completely hindered. As the simulation progresses these ions are pushed out laterally and eventually move through the polymer constituent.

4.4.3 Deformation response

Figure 4.14 gives the average displacement on a plane midway through the RVE in the direction longitudinally and transversely to the ion flux at the end of the simulation ($t = 1750$ ns). This plane was selected so as to mitigate effects of the influx boundary condition. The ions flow predominately in the $x-$direction. The displacement in

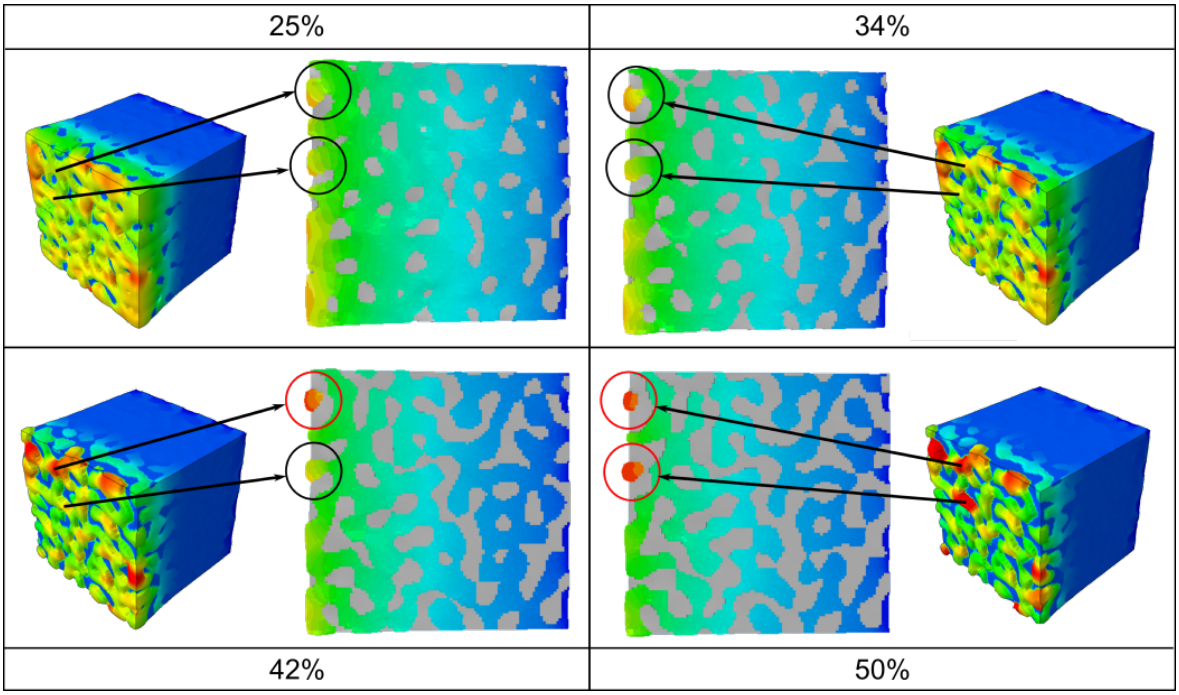

Fig. 4.13: Cross sections of the RVEs showing the concentration field and revealing perpendicular gold elements that have slowed down the ion flow through the the RVE and caused a build up of ions (red encircled areas) resulting in a speckled pattern on the influx face of the RVEs. The black circled regions show the unimpeded flow of ions at the lower volume fractions. This is most prominent at higher gold volume fractions.

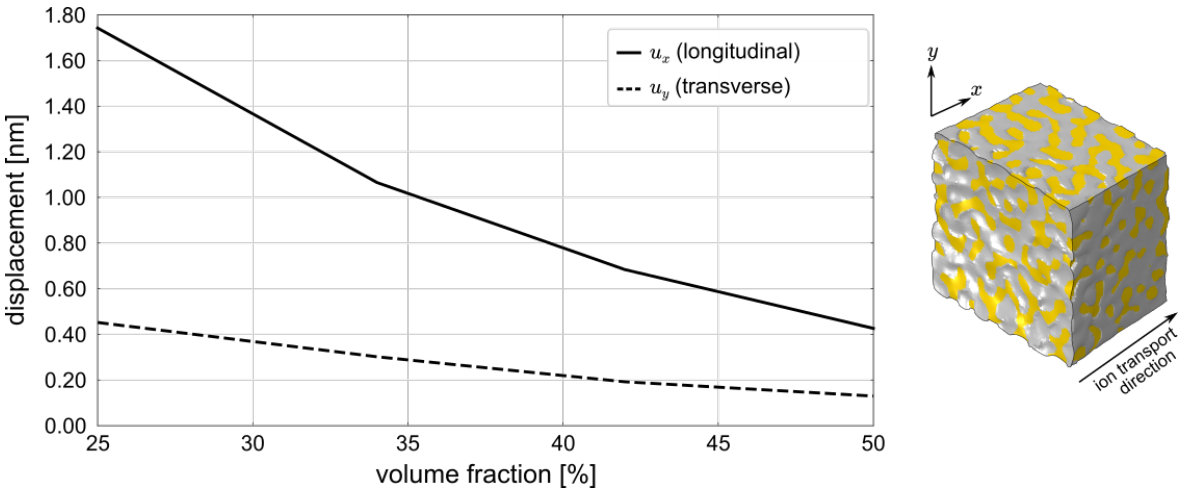

Fig. 4.14: The average displacement of a plane midway through the RVE longitudinally and transversely to the ion transport direction as indicated on the left of the graph. [9]

the $z-$direction is quantitatively and qualitatively similar to the displacement in the $y-$direction and so is not given here. Figure 4.15 shows a cross section of each RVE at the end of the simulation where the deformations have been exaggerated to allow for visual comparisons to be made.

[9] Reproduced with permission from Elsevier (https://doi.org/10.1016/j.jmps.2019.103848)

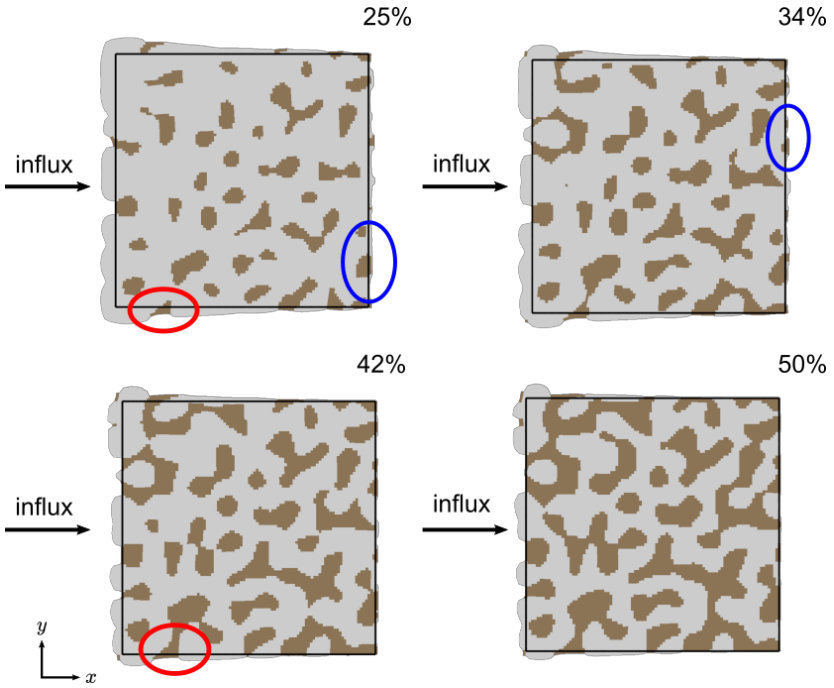

Fig. 4.15: Cross section showing the deformation of the RVEs. For visual comparison, the deformations have been exaggerated. The gold material is shown in brown and the polymer in grey. The solid black lines represent the undeformed RVE. The blue circles indicate areas where the gold has been pushed out in the direction transverse to the ion flux due to the expanding polymer. The red encircled areas indicate bulging areas where the gold has remained relatively undeformed compared to the polymer. [10]

These figures show a clear relationship between the deformation and the gold volume fraction. The gold constituent does not undergo expansion or shrinkage itself and so its deformation can only be facilitated by the deformation of the polymer surrounding it. Thus, as the volume fraction of gold increases there is a combination of both less polymer material to produce and apply a force as well as more gold to counteract this reduced force. Additionally, the higher interconnectivity of the gold adds a further strengthening factor that will aid in its resistance to the movement and deformation caused by the polymer.

In Figure 4.14 a difference in the magnitude of deformation between the longitudinal and transverse directions is noted. This difference is attributed to two different mechanisms of displacement. In the direction longitudinal to the ion flux, the deformation is a result of a displacing mechanism while transversely the displacement results from a deformation of the gold due to it being carried by the surrounding polymer.

[10] Reproduced with permission from Elsevier (https://doi.org/10.1016/j.jmps.2019.103848)

In Figure 4.15 the blue encircled regions show examples of the displacing mechanism. Here, the gold has been pushed outwards by the expansion of the polymer phase occurring earlier in the RVE.

The transverse deformation results from the polymer exerting a force directly on the gold which causes it to deform. However, compared to the compliant polymer, the gold's high stiffness hinders this deformation mechanism. This mechanism is less effective due to the high stiffness of the gold and the high compliance of the polymer, thus resulting in a smaller displacement compared to that in the longitudinal direction. The hindrance of the polymer's deformation by the gold also causes bulging of the polymer. Examples of this are seen within the regions encircled in red in Figure 4.15. The amount of bulging decreases with a decrease in gold volume fraction as there is more polymer and hence a larger force can be exerted on the gold (of which there is also less, which decreases its efficacy in resisting deformation). This bulging creates opportunities for delamination to occur which is, obviously, disadvantageous to the use of this composites as an actuator.

Using the relation for the effective Young's modulus of the nanocomposite (Equation (2.39)) the Young's moduli of the 25%, 34%, 42% and 50% RVEs are calculated to be $4.49, 7.34, 11.00$ and 15.82 GPa respectively. Thus with only double the amount of gold, the 50% RVE is 4 times stiffer than the 25% RVE. Similarly the deformations of the 50% RVE are 4 and 3.5 times smaller in the longitudinal and transverse directions respectively compared to that for the 25% RVE. The deformations thus seem to scale equally to the stiffness of the material and so there exists a trade-off between stiffness and strength on the one hand, and the deformation of the actuator on the other as is noted with conventional composites.

A noteworthy feature of the deformation of the RVE is that it occurs in all three directions. Even though some directions present larger deformations than others, this three-dimensional facilitated and reinforced deformation is an advantage over other conventional composites such as fibre-reinforced composites as it creates the opportunity for a wider variety of actuation mechanisms to be utilized.

Figure 4.16 shows the development of the average transverse displacement and the ion concentration at the midway plane over time. For the first 250 ns the ion concentration remains at its initial state as ions are still moving through the first half of the RVE. Following this, the ion concentration increases non-linearly until a plateau is reached.

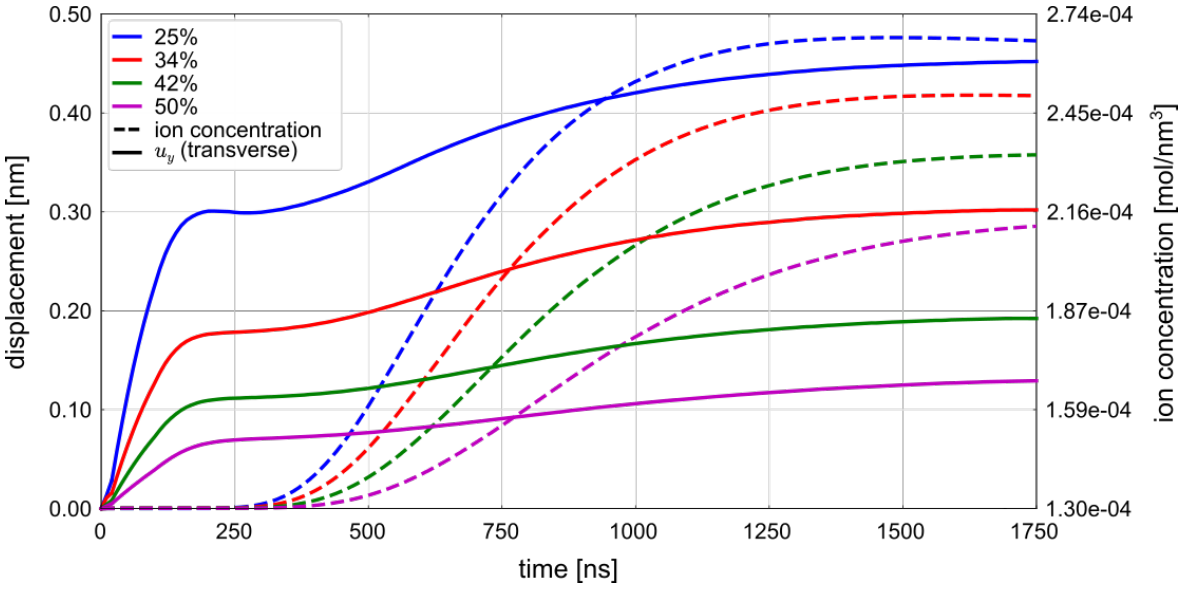

Fig. 4.16: The average displacement transverse to the ion flux direction (solid lines) of a plane midway through an RVE and the average ion concentration (dashed line) on this plane for each volume fraction.[11]

As also noted in Figure 4.12, ion flux occurs faster in the material with lower gold volume fractions. The 25% volume fraction RVE reaches its equilibrium concentration far sooner than the larger volume fraction RVEs. The first increase in ion concentration occurs earliest in the lowest gold volume fraction RVE with a slight delay noted as the gold volume fraction increases. The higher equilibrium concentrations at higher volume fractions results from there being less polymer material.

For the first 250 ns there is a drastic increase in the transverse displacement despite no increase in ion concentration. The displacement occurring during this time must therefore be a result of the displacing deformation mechanism discussed previously. As there are no excess ions in the polymer at this location, the polymer here cannot be expanding; rather, the polymer in the first half (where ions are moving through) is deforming and this deformation is transferred over the interconnected gold network to cause the expansion seen. Following this period of time, as the ion concentration increases, the deformation also shows an increase as the second deformation mechanism begins to take effect, with the gold being carried by the expansion of the surrounding polymer. Evidence of the dependence of transverse deformation on the concentration also comes from the fact that as the concentration levels off in the last 250 ns, so too does the displacement.

[11] Reproduced with permission from Elsevier (https://doi.org/10.1016/j.jmps.2019.103848)

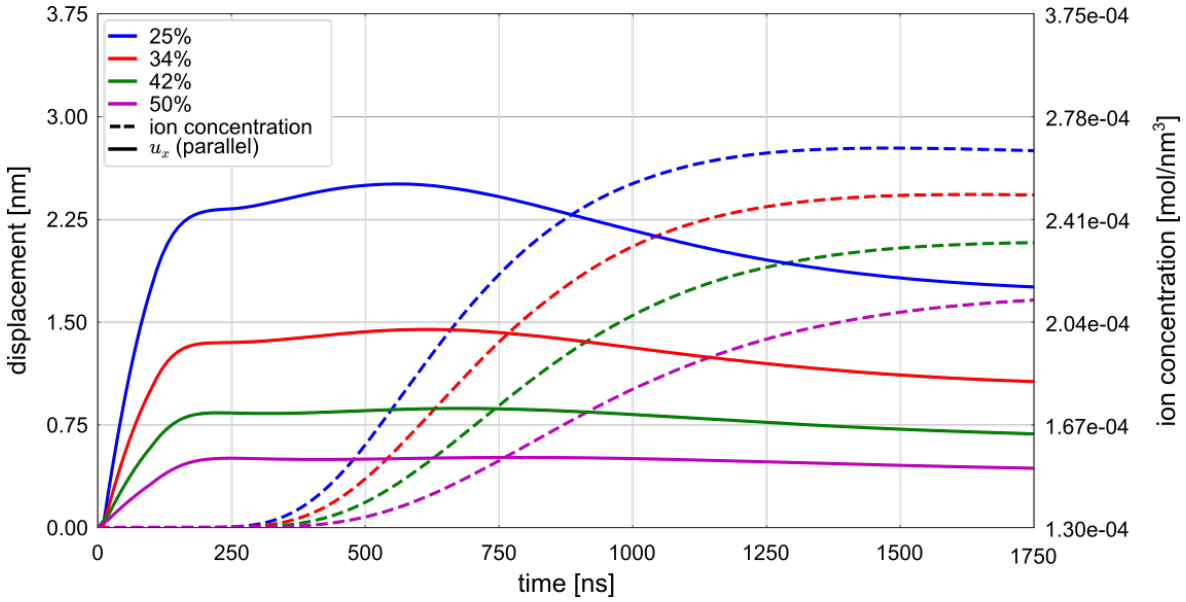

Fig. 4.17: The average displacement longitudinal to the ion flux direction (solid lines) of plane midway through an RVE and the average ion concentration (dashed line) on this plane for each volume fraction.

Figure 4.17 shows the longitudinal displacement at the midway plane in comparison to the ion concentration. As with the transverse displacement, in all RVEs there is an initial sharp increase in displacement resulting from the displacing deformation mechanism. As the ion concentration begins to increase, a slight increase in the deformation also occurs as the second deformation mechanism is initialized. Both mechanisms work together until a maximum displacement is reached.

Thereafter, the longitudinal displacement no longer follows the same trend as the transverse displacement and a decrease is seen even though the ion concentration increases. During this stage the second deformation mechanism becomes more prominent and the first mechanism is no longer acting suggesting that the longitudinal displacement is more dependent on the first mechanism rather than the second mechanism.

Finally, the development of the normal stress transverse to the ion flow direction of the gold constituent throughout the simulation for each RVE is shown in Figure 4.18. Three interesting features are noted:

(i) A shift from a compressive response to a tensile response is seen as the gold volume fraction increases;

(ii) The 42% RVE shows a decreasing compressive stress as the simulation develops, which is unexpected as Figure 4.16 and 4.17 show an overall increase in the deformation over time;

(iii) Between the 25% and 42% RVE there is a decrease in stress with increasing gold volume fraction as expected as the deformation decreases. However, the 50% volume fraction of gold shows an increase in the stress magnitude in the RVE over that in the 42% RVE even though the 42% RVE undergoes greater deformation.

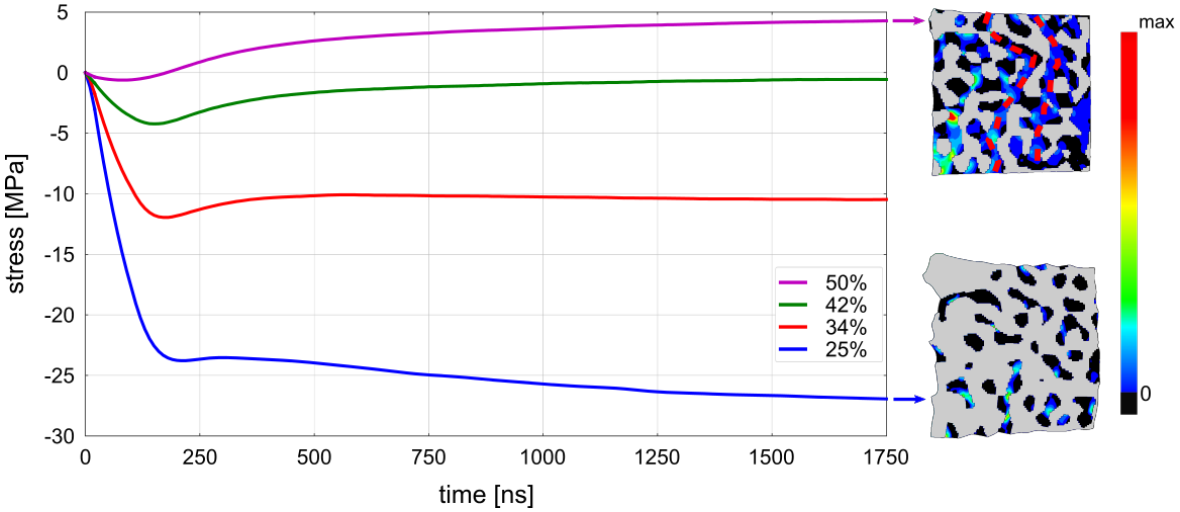

Fig. 4.18: The volume averaged transverse normal stress development within the gold constituent of each RVE. The contour plots of a cross sections of the 50% and 25% RVE are shown to the right. The black regions indicate regions of compression. The red lines indicate pathways that allow the gold to expand and thus decrease the compressive stress. The polymer constituent is shown in grey.[12]

Regarding (i), at the lowest volume fraction a compressive stress response within the gold constituent is noted. As the volume fraction increases the magnitude of the compressive stress decreases, until at the highest volume fraction a fully tensile stress response is seen. To explain why this feature exists in the gold phase two cross sections of the highest and lowest gold volume fraction RVEs are shown in Figure 4.18. The stress contours of the gold material acting transverse to the ion flow ($y-$direction) are depicted. As expected the polymer phase shows a tensile response throughout all four RVEs and so is shown here in grey. Black regions indicate areas of compressive stress. In agreement with the accompanying stress plots, it is clear from these stress contours that there are more regions of tensile stress than compressive stress in the 50% RVE. This can be understood by considering two extreme scenarios. Consider first a gold sphere surrounded by a polymer, secondly a polymer sphere surrounded by gold. In the first scenario, representative of a low volume fraction sample, as the polymer expands the gold experiences compressive forces from all sides resulting in a compressive

[12] Reproduced with permission from Elsevier (https://doi.org/10.1016/j.jmps.2019.103848)

response. In the second case, representative of a high volume fraction sample, the expansion of the polymer produces a force on the inner surface of the surrounding gold which pushes it outwards. This would in turn cause the gold to expand into the open space and undergo tensile deformation. Comparing the first case with that for the 25% RVE, here the gold is almost encapsulated by the polymer and hence experiences the expansion of the polymer as a compressive force. In the 50% RVE, as in case two, there is less polymer surrounding the gold and so fewer pockets of gold are under a compressive stress. Continuous gold pathways through the cross section of the RVE exist (see red dashed lines in Figure 4.18); along these the gold is able to expand and hence produce more areas of tensile stress.

Figure 4.18 reveals a unique response in the 42% RVE characterised by features (ii) and (iii). Feature (ii) is unique as one would expect the stress to increase as the deformation of the RVE increases due to the ion transport through the polymer. This is not the case in this RVE. In addition, feature (iii) is unexpected as it has been established that as the gold volume fraction increases the deformation within the RVE decreases. Thus one would expect the stress developed to also decrease. This trend is seen in the RVEs from 25-42% gold fraction but from the 42% to the 50% RVE the stress magnitude increases. A complex interaction between the gold and polymer interconnected phases is suggested as a reason behind both of these features. Above a certain volume fraction, the reinforcing effects of the gold constituent become disadvantageous as it becomes too constricting, and thus large deformations are not allowed. A lower volume fraction of polymer also prevents it from exerting enough force to overcome the stiffness of the gold. Below this volume fraction, however, the gold connectivity is weak and its reinforcing ability is decreased. The deformation of the polymer can no longer be prevented and this results in large deformations. The encapsulating nature of the polymer also results in a reduction in the number of expansion pathways. The deformation and associated stress development in the nanocomposite are both important properties that are affected by the volume fraction of gold, and need to be taken into account if this material is to be considered for use in actuation applications.

5

Summary, conclusions and recommendations

5.1 Summary

Nanoporous metals have unique and favourable properties, especially in compression. Due to their brittle and poor performance in tension, however, their usage has been limited. The creation of a composite in which the pores of the gold component are impregnated with a polymer has the potential to address this shortcoming. Previous experimental testing has shown drastic improvements in not only tensile but also its compressive behaviour, thus opening it up to more extensive use in structural applications. The presence of a polymer phase also creates the possibility for its usage in applications other than mechanical and structural, such as actuation and energy storage. The micromechanical response and mechanisms causing the interesting effects in metal/polymer nanocomposites are difficult to probe experimentally due to the nanoscale nature of this material. The use of the finite element method provides an avenue through which this can be investigated. In this work the response of a gold/polymer nanocomposite has been investigated under three different physical situations using representative volume elements.

Elastic response of the nanocomposite

First of all, the effective elastic properties of the nanocomposite were calculated by numerical homogenization using three different boundary conditions: kinematic uniform, static uniform and periodic. Periodic boundary conditions were successfully applied to a non-periodic mesh using a master/slave method. The isotropic behaviour of the nanocomposite was confirmed and quantified using a variety of anisotropic indices. The material behaviour was, thus, fully defined by calculating the effective Young's modulus and Poisson's ratio. Good agreement between the three numerical results was noted, confirming the representativeness of the material volume element. Under all three boundary conditions the effective Young's modulus lay within the Reuss-Voigt

and Hashin-Shtrikman bounds. Good agreement with experimental results and analytical scaling laws was also shown.

Under compression, the stress-strain micromechanical response along the centroid of the RVE was investigated. Comparing the constituents, the relatively compliant polymer constituent showed higher strain values while the relatively stiff gold material showed higher stress values. A combination of compressive and tensile values, especially in the gold material, were also revealed as a result of the complex network connection of the gold material. Comparison of the results of the constituents within the nanocomposite to homogeneous blocks of each constituent revealed that the polymer undergoes significantly more strain than its pure material counterpart while the gold experiences less strain and stress than its bulk counterpart.

A further investigation into the micromechanical response under compression was conducted by investigating the loading case and stress distributions in 10 ligaments within the RVE. This revealed a combination of bending and axial loading, significant torque and an unexpectedly large shear force. A shift from the presence of axial dominated loading modes of ordered network structures to a bending and torque dominated loading mode in pure NPG is suggested to play a role in its increased compliance, so too does the nanocomposite show similar loading modes even though the ligaments are now surrounded by a polymer material. In tension, NPG shows an axial dominated loading mode which is suggested, in part, to cause its brittle nature. In contrast to this the nanocomposite showed a significant amount of bending in the ligaments under tensile loading as the nanocomposite now has an elastic tension/compression symmetry. This shift to a more bending dominated loading mode may, in part, account for the improved tensile ductility of the nanocomposite.

The orientation of the ligaments was also shown to have a large influence on the type and magnitude of loading experienced. Compression-axis aligned ligaments showed compressive normal forces and substantially higher bending moments compared to non-aligned ligaments. Overall, compression-axis aligned ligaments experienced larger stresses.

Fracture of nanoporous gold and its polymer filled counterpart

The next investigation concerned the fracture behaviour of the nanocomposite through 'virtual' compact-tension (CT) testing. CT testing using specimens with an embedded pure NPG or gold/epoxy nanocomposite RVE at the crack tip were conducted using Abaqus/Explicit. The gold was modelled using a J_2 plasticity model coupled with

a Lemaitre damage model, while for the epoxy a Gearing-Anand amorphous polymer viscoplasticity model with a critical plastic stretch dependent failure criteria was used. Load-displacement curves and visualizations of the crack propagations were then created, and mechanical properties were calculated for samples of various gold volume fractions.

The most striking result was the exceptional improvement in ductility in the nanocomposite compared to the pure NPG sample at all volume fractions. Two main mechanisms were observed to have contributed to the increased ductility. The first was related to the stabilization of ligament breakages by the surrounding polymer. When a ligament broke, the load was transferred across a large area via the interpenetrating polymer and hence there was a decrease in the localized stress concentrations. Related to this is the second mechanism of ductility whereby a large fracture process zone was noted at the crack tip in the nanocomposite. This reduced the crack tip driving force allowing for more deformation to occur without reaching the critical limit. The amount of gold within the specimens significantly affected the size of the process zone with lower gold volume fraction samples showing significantly larger process zones accompanying a increase in ductility. Neither of these mechanisms occurs in the pure NPG samples. The second mechanism facilitating ductility cannot exist as the process zone size is limited to the diameter of the ligaments at the crack tip.

The effect of the volume fraction of gold on several mechanical properties was also investigated. With a decrease in the volume fraction of gold an increase in the ultimate fracture displacement and a decrease in the ultimate strength was seen. It was shown that the weaker performing constituent dictated the performance in each of these properties. That is, while the gold's brittle nature had a greater effect on the composite's displacement at fracture compared to the polymer's ductile nature, the polymer's low strength had a greater influence on the strength of the nanocomposite than did the gold's high strength. The increase in network connectivity resulting from an increased gold volume fraction was also considered to play a role in this increased strength. A relatively high resistance to fracture was found in the lowest volume fraction nanocomposite sample. It had a toughness equal to that of the highly ductile pure polymer material. Toughening mechanisms that were observed to contribute to the resistance to fracture include crack deflection, crack bridging and secondary cracking. The last two were highly prevalent in nanocomposite samples of low gold volume fractions.

Finally, the effects of specimen thickness on plane stress-plane strain fracture was investigated. A shift from plane stress to plane strain fracture was only noted in the

lower volume fraction samples as a result of their greater ductility. The lower ductility of the higher volume fraction samples prevented any through-thickness thinning which is necessary for plane stress fracture to occur.

Chemo-electro-mechanical coupling in the nanocomposite

The third situation investigated was that of the electrically stimulated deformation of the nanocomposite. This deformation is brought about by the volumetric expansion or shrinkage of an impregnated conductive polymer due to ion ingress or egress respectively. Using a coupled chemo-electro-mechanical theory, the micromechanical response was investigated by simulating nanocomposite RVEs taken from the working electrode of an electrolytic cell.

In order to implement this theory within Abaqus a staggered explicit-implicit solution scheme had to be developed, in which the ion transport and displacement fields were solved monolithically in Abaqus/Explicit while the electrostatic field was solved intermittently in Abaqus/Standard. This scheme made use of several Abaqus subroutines and Python scripting to facilitate data transfer and the interfacing between Abaqus/Explicit and Abaqus/Standard.

The simulation of RVEs with different gold volume fractions was carried out. In all samples a small shift was noted in the electrostatic field over time and significant differences between different volume fraction samples were noted in the ion transport and displacement fields.

The ion transport field showed a clear dependence on the volume fraction of gold. An increase in gold volume fraction was accompanied by a decrease in the ion transport rate through the RVE. This was attributed to a combination of an increase in the number of gold pores aligned normal to the direction of ion flow which act as barriers to ion flow and a decrease in the polymer pore channels through which the ions flow.

Inspection of the deformation field revealed two mechanisms of micromechanical deformation in the nanocomposite. The first causes deformation by the expansion of the polymer phase occurring earlier in the material pushing the gold ahead of it outwards. This mechanism causes deformation in all directions of the RVE. The second deformation mechanism, which mainly affects the deformation transverse to the ion flux direction, causes deformation by the polymer carrying the gold along. Unlike the second mechanism, the first mechanism has the ability to affect areas where ions have not yet entered.

An investigation into the average transverse stress development revealed interesting results, such as a shift from a compressive to tensile stress state as the gold volume fraction increased. This was attributed to the extent to which the gold was surrounded and somewhat constrained by the polymer constituent. Additionally, it was suggested that there may exist a unique ratio of gold to polymer such that the gold provides sufficient reinforcement and the polymer induces enough force to displace and carry the gold, thereby still allowing significant displacement to occur.

5.2 Conclusion

This work has studied the response of a gold/polymer nanocomposite under three scenarios. Relationships between material properties and the response of this material were suggested and, through the use of the finite element method in conjunction with representative volume elements, the micromechanical response has been probed. From this it is evident that a gold/polymer nanocomposite has unique and favourable characteristics in compression, tension and actuation. Nevertheless, depending on the application, trade-offs on its characteristics may have to be made. Factors such as the constituents' material properties, the volume fraction and network connectivity of constituents as well as the orientation of the ligaments were observed to influence the material's properties.

In many cases the nanocomposite was shown to perform similarly if not better than conventional composites. Advantages over and above these conventional composites were also found; for example, the isotropic response of the nanocomposite compared to the transversely isotropic nature of fibre-reinforced composites.

In addition to the investigation of the macroscopic response of the nanocomposite, the use of computational 'virtual' testing allowed the probing of the microstructure and the observation of micromechanical mechanisms that would be difficult to achieve otherwise. Through this, insights have been added to the knowledge base which could potentially then be used to tailor the microstructure of the nanocomposite with the aim of enhancing the macroscopic response. Additionally, mechanisms identified in this material could be induced in other materials to improve their response. For example, mechanisms identified here that contributed to an improvement in ductility may provide a guide to the study of other brittle materials.

A nanoporous metal impregnated with a polymer is a versatile and useful material. Its hierarchical structure lead to unique deformation mechanisms that enhance its performance over and above that of materials that are currently in use today. As more knowledge is gained about how its micromechanical response links to its macroscopic response it can be further enhanced and promoted for use in a variety of applications.

5.3 Recommendations

Nanoporous gold is a relatively new material and as such, there are still many avenues of research that exist through which insights can be gained into its behaviour and properties. The polymer impregnated nanoporous metal composite is an even more recent creation and its superior properties are still being investigated. Future work to be considered to aid in understanding the behaviour of these material include the following:

- Including length scale effects in the constitutive models. This can be achieved by implementing a gradient crystal plasticity model. Computational testing of gold/polymer nanocomposites under a variety of situations with these features included would allow for the high surface-to-volume ratio to be accounted for. Through this the influence of the size of ligament diameters on the material properties can be probed;
- The addition of an interface model between the constituents to explore the effects of delamination under all three scenarios;
- A computational investigation into the plastic response of the nanocomposite under a variety of loading conditions is an area of research that is not yet well developed (using a gradient crystal plasticity model as well);
- Computational and micromechanical investigation of the material's behaviour under different testing methods such as shear and bending tests as well as its response under fatigue and impact loading could also provide further insights into the benefits of the hierarchical structure of this material.

References

1. R. Lakes, Materials with structural hierarchy, Nature 361 (6412) (1993) 511–515.
2. J.-Y. Rho, L. Kuhn-Spearing, P. Zioupos, Mechanical properties and the hierarchical structure of bone, Medical Engineering & Physics 20 (2) (1998) 92–102.
3. P. Fratzl, R. Weinkamer, Nature's hierarchical materials, Progress in Materials Science 52 (8) (2007) 1263–1334.
4. M. P. Groover, Fundamentals of Modern Manufacturing: Materials, Processes, and Systems, Prentice Hall, 1996.
5. K. Wang, J. Weissmüller, Composites of nanoporous gold and polymer, Advanced Materials 25 (9) (2013) 1280–1284.
6. J. Wilmers, A. McBride, S. Bargmann, Interface elasticity effects in polymer-filled nanoporous metals, Journal of the Mechanics and Physics of Solids 99 (2017) 163–177.
7. J. Biener, A. Hamza, A. Hodge, Deformation Behavior of Nanoporous Metals, Springer US, Boston, MA, 2008, pp. 118–135.
8. J. R. Greer, W. C. Oliver, W. D. Nix, Size dependence of mechanical properties of gold at the micron scale in the absence of strain gradients, Acta Materialia 53 (6) (2005) 1821–1830.
9. J. Biener, A. M. Hodge, A. V. Hamza, L. M. Hsiung, J. H. Satcher Jr, Nanoporous Au: A high yield strength material, Journal of Applied Physics 97 (2) (2005) 024301.
10. A. Wittstock, J. Biener, J. Erlebacher, M. Baumer (Eds.), Nanoporous Gold, Royal Society of Chemistry Nanoscience & Nanotechnology, The Royal Society of Chemistry, 2012.
11. Y. Ding, M. Chen, J. Erlebacher, Metallic mesoporous nanocomposites for electrocatalysis, Journal of the American Chemical Society 126 (22) (2004) 6876–6877.
12. H.-J. Jin, J. Weissmüller, Bulk nanoporous metal for actuation, Advanced Engineering Materials 12 (8) (2010) 714–723.
13. J. Weissmüller, Charge-induced reversible strain in a metal, Science 300 (5617) (2003) 312–315.
14. E. Detsi, Z. Vuković, S. Punzhin, P. M. Bronsveld, P. R. Onck, J. T. M. De Hosson, Fine-tuning the feature size of nanoporous silver, CrystEngComm 14 (17) (2012) 5402–5406.
15. Z. Zhang, Y. Wang, Z. Qi, W. Zhang, J. Qin, J. Frenzel, Generalized fabrication of nanoporous metals (Au, Pd, Pt, Ag, and Cu) through chemical dealloying, The Journal of Physical Chemistry C 113 (29) (2009) 12629–12636.
16. J. Hayes, A. Hodge, J. Biener, A. Hamza, K. Sieradzki, Monolithic nanoporous copper by dealloying Mn–Cu, Journal of Materials Research 21 (10) (2006) 2611–2616.
17. M. Hakamada, M. Takahashi, T. Furukawa, M. Mabuchi, Coercivity of nanoporous Ni produced by dealloying, Applied Physics Letters 94 (15) (2009) 153105.
18. H.-J. Qiu, J. Kang, P. Liu, A. Hirata, T. Fujita, M. Chen, Fabrication of large-scale nanoporous nickel with a tunable pore size for energy storage, Journal of Power Sources 247 (2014) 896–905.
19. S. Shi, J. Markmann, J. Weissmüller, Actuation by hydrogen electrosorption in hierarchical nanoporous palladium, Philosophical Magazine 97 (19) (2017) 1571–1587.

20. J. Zhang, Q. Bai, Z. Zhang, Dealloying-driven nanoporous palladium with superior electrochemical actuation performance, Nanoscale 8 (13) (2016) 7287–7295.
21. I. Okulov, J. Weissmüller, J. Markmann, Dealloying-based interpenetrating-phase nanocomposites matching the elastic behavior of human bone, Scientific Reports 7 (1) (2017) 20.
22. W. Yang, X.-G. Zheng, S.-G. Wang, H.-J. Jin, Nanoporous aluminum by galvanic replacement: Dealloying and inward-growth plating, Journal of The Electrochemical Society 165 (9) (2018) C492–C496.
23. J. Biener, A. M. Hodge, A. V. Hamza, Microscopic failure behavior of nanoporous gold, Applied Physics Letters 87 (12) (2005) 121908.
24. J. Weissmüller, R. C. Newman, H.-J. Jin, A. M. Hodge, J. W. Kysar, Nanoporous metals by alloy corrosion: formation and mechanical properties, Material Research Society Bulletin 34 (08) (2009) 577–586.
25. H.-J. Jin, L. Kurmanaeva, J. Schmauch, H. Rösner, Y. Ivanisenko, J. Weissmüller, Deforming nanoporous metal: Role of lattice coherency, Acta Materialia 57 (9) (2009) 2665–2672.
26. J. Biener, A. M. Hodge, J. R. Hayes, C. A. Volkert, L. A. Zepeda-Ruiz, A. V. Hamza, F. F. Abraham, Size effects on the mechanical behavior of nanoporous Au, Nano Letters 6 (10) (2006) 2379–2382.
27. T. J. Balk, C. Eberl, Y. Sun, K. J. Hemker, D. S. Gianola, Tensile and compressive microspecimen testing of bulk nanoporous gold, The Journal of The Minerals, Metals & Materials Society 61 (12) (2009) 26–31.
28. N. J. Briot, T. Kennerknecht, C. Eberl, T. J. Balk, Mechanical properties of bulk single crystalline nanoporous gold investigated by millimetre-scale tension and compression testing, Philosophical Magazine 94 (8) (2014) 847–866.
29. S. Sun, X. Chen, N. Badwe, K. Sieradzki, Potential-dependent dynamic fracture of nanoporous gold, Nature Materials 14 (9) (2015) 894–898.
30. N. Badwe, X. Chen, K. Sieradzki, Mechanical properties of nanoporous gold in tension, Acta Materialia 129 (2017) 251–258.
31. N. Badwe, Fracture of nanoporous gold, Ph.D. thesis, Arizona State University (2014).
32. A. Hodge, J. Biener, J. Hayes, P. Bythrow, C. Volkert, A. Hamza, Scaling equation for yield strength of nanoporous open-cell foams, Acta Materialia 55 (4) (2007) 1343–1349.
33. E.-J. Gwak, H. Jeon, E. Song, N.-R. Kang, J.-Y. Kim, Twinned nanoporous gold with enhanced tensile strength, Acta Materialia 155 (2018) 253–261.
34. P. Liu, X. Wei, S. Song, L. Wang, A. Hirata, T. Fujita, X. Han, Z. Zhang, M. Chen, Time-resolved atomic-scale observations of deformation and fracture of nanoporous gold under tension, Acta Materialia 165 (2019) 99–108.
35. J. Stuckner, M. Murayama, Mechanical properties of nanoporous gold subjected to tensile stresses in real-time, sub-microscopic scale, Journal of Materials Science 54 (18) (2019) 12106–12115.
36. R. Li, K. Sieradzki, Ductile-brittle transition in random porous Au, Physical Review Letters 68 (8) (1992) 1168–1171.
37. E.-J. Gwak, J.-Y. Kim, Weakened flexural strength of nanocrystalline nanoporous gold by grain refinement, Nano Letters 16 (4) (2016) 2497–2502.
38. R. Xia, C. Xu, W. Wu, X. Li, X.-Q. Feng, Y. Ding, Microtensile tests of mechanical properties of nanoporous Au thin films, Journal of Materials Science 44 (17) (2009) 4728–4733.
39. X.-Y. Sun, G.-K. Xu, X. Li, X.-Q. Feng, H. Gao, Mechanical properties and scaling laws of nanoporous gold, Journal of Applied Physics 113 (2) (2013) 023505.
40. N. Beets, D. Farkas, Mechanical response of Au foams of varying porosity from atomistic simulations, JOM 70 (10) (2018) 2185–2191.
41. J. Li, Y. Xian, H. Zhou, R. Wu, G. Hu, R. Xia, Microstructure-sensitive mechanical properties of nanoporous gold: A molecular dynamics study, Modelling and Simulation in Materials Science and Engineering 26 (7) (2018) 075003.
42. C. Volkert, E. Lilleodden, D. Kramer, J. Weissmüller, Approaching the theoretical strength in nanoporous Au, Applied Physics Letters 89 (6) (2006) 061920.
43. M. Hakamada, M. Mabuchi, Mechanical strength of nanoporous gold fabricated by dealloying, Scripta Materialia 56 (11) (2007) 1003–1006.

44. K. Wang, A. Kobler, C. Kübel, H. Jelitto, G. Schneider, J. Weissmüller, Nanoporous-gold-based composites: toward tensile ductility, NPG Asia Materials 7 (6) (2015) e187.
45. K. Wang, Composites of Nanoporous Gold and Polymer, Ph.D. thesis, Technischen Universität Hamburg (2015).
46. N. Mameka, K. Wang, J. Markmann, E. T. Lilleodden, J. Weissmüller, Nanoporous gold-testing macroscale samples to probe small-scale mechanical behavior, Materials Research Letters 4 (1) (2016) 27–36.
47. L.-Z. Liu, X.-L. Ye, H.-J. Jin, Interpreting anomalous low-strength and low-stiffness of nanoporous gold: Quantification of network connectivity, Acta Materialia 118 (2016) 77–87.
48. L. Lührs, C. Soyarslan, J. Markmann, S. Bargmann, J. Weissmüller, Elastic and plastic Poisson's ratios of nanoporous gold, Scripta Materialia 110 (2016) 65–69.
49. K. Hu, M. Ziehmer, K. Wang, E. T. Lilleodden, Nanoporous gold: 3D structural analyses of representative volumes and their implications on scaling relations of mechanical behaviour, Philosophical Magazine 96 (32-34) (2016) 3322–3335.
50. S. Bargmann, C. Soyarslan, E. Husser, N. Konchakova, Materials based design of structures: Computational modeling of the mechanical behavior of gold-polymer nanocomposites, Mechanics of Materials 94 (2016) 53–65.
51. M. Graf, B. Roschning, J. Weissmüller, Nanoporous gold by alloy corrosion: Method-structure-property relationships, Journal of The Electrochemical Society 164 (4) (2017) C194–C200.
52. A. Hodge, R. Doucette, M. Biener, J. Biener, O. Cervantes, A. Hamza, Ag effects on the elastic modulus values of nanoporous Au foams, Journal of Materials Research 24 (04) (2009) 1600–1606.
53. L.-Z. Liu, H.-J. Jin, Scaling equation for the elastic modulus of nanoporous gold with "fixed" network connectivity, Applied Physics Letters 110 (21) (2017) 211902.
54. A. Mathur, J. Erlebacher, Size dependence of effective Young's modulus of nanoporous gold, Applied Physics Letters 90 (6) (2007) 061910.
55. J. Jiao, N. Huber, Deformation mechanisms in nanoporous metals: Effect of ligament shape and disorder, Computational Materials Science 127 (2017) 194–203.
56. N. Huber, R. Viswanath, N. Mameka, J. Markmann, J. Weißmüller, Scaling laws of nanoporous metals under uniaxial compression, Acta Materialia 67 (2014) 252–265.
57. B. Roschning, N. Huber, Scaling laws of nanoporous gold under uniaxial compression: Effects of structural disorder on the solid fraction, elastic Poisson's ratio, Young's modulus and yield strength, Journal of the Mechanics and Physics of Solids 92 (2016) 55–71.
58. K. Mangipudi, E. Epler, C. Volkert, Topology-dependent scaling laws for the stiffness and strength of nanoporous gold, Acta Materialia 119 (2016) 115–122.
59. C. Soyarslan, E. Husser, S. Bargmann, Effect of surface elasticity on the elastic response of nanoporous gold, Journal of Nanomechanics and Micromechanics 7 (4) (2017) 04017013.
60. G. Pia, F. Delogu, Nanoporous Au: Statistical analysis of morphological features and evaluation of their influence on the elastic deformation behavior by phenomenological modeling, Acta Materialia 85 (2015) 250–260.
61. L. J. Gibson, M. F. Ashby, The mechanics of three-dimensional cellular materials, Proceedings of the Royal Society A: Mathematical, Physical and Engineering Sciences 382 (1782) (1982) 43–59.
62. V. Deshpande, M. Ashby, N. Fleck, Foam topology: bending versus stretching dominated architectures, Acta Materialia 49 (6) (2001) 1035–1040.
63. G. Pia, M. Brun, F. Aymerich, F. Delogu, Gyroidal structures as approximants to nanoporous metal foams: clues from mechanical properties, Journal of Materials Science 52 (2) (2016) 1106–1122.
64. S. L. Choi, Mechanics of compliant nanoporous gold, Ph.D. thesis, University of Toronto (2009).
65. K. Hu, Micromechanical and three-dimensional microstructural characterization of nanoporous gold-epoxy composites, Ph.D. thesis, Hamburg University of Technology (2017).
66. X. Lang, A. Hirata, T. Fujita, M. Chen, Nanoporous metal/oxide hybrid electrodes for electrochemical supercapacitors, Nature Nanotechnology 6 (4) (2011) 232–236.
67. F. Meng, Y. Ding, Sub-micrometer-thick all-solid-state supercapacitors with high power and energy densities, Advanced Materials 23 (35) (2011) 4098–4102.

68. C. Stenner, L.-H. Shao, N. Mameka, J. Weissmüller, Piezoelectric gold: Strong charge-load response in a metal-based hybrid nanomaterial, Advanced Functional Materials 26 (28) (2016) 5174–5181.
69. E. Detsi, P. R. Onck, J. T. M. D. Hosson, Electrochromic artificial muscles based on nanoporous metal-polymer composites, Applied Physics Letters 103 (19) (2013) 193101.
70. C. Soyarslan, M. Pradas, S. Bargmann, Effective elastic properties of 3D stochastic bicontinuous composites, Mechanics of Materials (2019) 103098
71. J. Li, C. Tian, B. Lu, Y. Xian, R. Wu, G. Hu, R. Xia, Deformation behavior of nanoporous gold based composite in compression: A finite element analysis, Composite Structures 211 (2019) 229–235.
72. S. Gnegel, J. Li, N. Mameka, N. Huber, A. Düster, Numerical investigation of polymer coated nanoporous gold, Materials 12 (13) (2019) 2178.
73. T. I. Zohdi, P. Wriggers, Computational micro-macro material testing, Archives of Computational Methods in Engineering 8 (2) (2001) 131–228.
74. T. I. Zohdi, P. Wriggers, An Introduction to Computational Micromechanics, Springer Science & Business Media, 2008, Ch. 4, pp. 45–62.
75. S. Bargmann, B. Klusemann, J. Markmann, J. E. Schnabel, K. Schneider, C. Soyarslan, J. Wilmers, Generation of 3D representative volume elements for heterogeneous materials: A review, Progress in Materials Science 94 (2018) 322–384.
76. C. Cantrell, Molecular dynamics simulation of mechanical behavior of nanoporous copper foams, Ph.D. thesis, Massachusetts Institute of Technology (2006).
77. C. Soyarslan, H. Argeso, S. Bargmann, Skeletonization-based beam finite element models for stochastic bicontinuous materials: Application to simulations of nanoporous gold, Journal of Materials Research 33 (20) (2018) 3371–3382.
78. K. Mangipudi, E. Epler, C. Volkert, On the multiaxial yielding and hardness to yield stress relation of nanoporous gold, Scripta Materialia 146 (2018) 150–153.
79. H.-H. Cho, Y.-C. K. Chen-Wiegart, D. C. Dunand, Finite element analysis of mechanical stability of coarsened nanoporous gold, Scripta Materialia 115 (2016) 96–99.
80. D. Farkas, A. Caro, E. Bringa, D. Crowson, Mechanical response of nanoporous gold, Acta Materialia 61 (9) (2013) 3249–3256.
81. B.-N. D. Ngô, A. Stukowski, N. Mameka, J. Markmann, K. Albe, J. Weissmüller, Anomalous compliance and early yielding of nanoporous gold, Acta Materialia 93 (2015) 144–155.
82. B.-N. D. Ngô, B. Roschning, K. Albe, J. Weissmüller, J. Markmann, On the origin of the anomalous compliance of dealloying-derived nanoporous gold, Scripta Materialia 130 (2017) 74–77.
83. C. Soyarslan, S. Bargmann, M. Pradas, J. Weissmüller, 3D stochastic bicontinuous microstructures: Generation, topology and elasticity, Acta Materialia 149 (2018) 326–340.
84. J. D. Eshelby, The determination of the elastic field of an ellipsoidal inclusion, and related problems, Proceedings of the Royal Society of London. Series A. Mathematical and Physical Sciences 241 (1226) (1957) 376–396.
85. T. Mori, K. Tanaka, Average stress in matrix and average elastic energy of materials with misfitting inclusions, Acta Metallurgica 21 (5) (1973) 571–574.
86. R. Hill, A self-consistent mechanics of composite materials, Journal of the Mechanics and Physics of Solids 13 (4) (1965) 213–222.
87. E. Kerner, The elastic and thermo-elastic properties of composite media, Proceedings of the physical society. Section B 69 (8) (1956) 808.
88. R. Hill, The elastic behaviour of a crystalline aggregate, Proceedings of the Physical Society. Section A 65 (5) (1952) 349.
89. C. Huet, Application of variational concepts to size effects in elastic heterogeneous bodies, Journal of the Mechanics and Physics of Solids 38 (6) (1990) 813–841.
90. T. Kanit, S. Forest, I. Galliet, V. Mounoury, D. Jeulin, Determination of the size of the representative volume element for random composites: statistical and numerical approach, International Journal of Solids and Structures 40 (13) (2003) 3647–3679.

91. F. Larsson, K. Runesson, S. Saroukhani, R. Vafadari, Computational homogenization based on a weak format of micro-periodicity for RVE-problems, Computer Methods in Applied Mechanics and Engineering 200 (1) (2011) 11–26.
92. K. Terada, M. Hori, T. Kyoya, N. Kikuchi, Simulation of the multi-scale convergence in computational homogenization approaches, International Journal of Solids and Structures 37 (16) (2000) 2285–2311.
93. C. Miehe, A. Koch, Computational micro-to-macro transitions of discretized microstructures undergoing small strains, Archive of Applied Mechanics 72 (4) (2002) 300–317.
94. C. Felippa, K. Park, The construction of free-free flexibility matrices for multilevel structural analysis, Computer Methods in Applied Mechanics and Engineering 191 (19-20) (2002) 2139–2168.
95. A. Javili, S. Saeb, P. Steinmann, Aspects of implementing constant traction boundary conditions in computational homogenization via semi-Dirichlet boundary conditions, Computational Mechanics 59 (1) (2016) 21–35.
96. S. Saeb, P. Steinmann, A. Javili, Aspects of Computational Homogenization at Finite Deformations: A Unifying Review From Reuss' to Voigt's Bound, Applied Mechanics Reviews 68 (5) (2016) 050801.
97. Z. Xia, Y. Zhang, F. Ellyin, A unified periodical boundary conditions for representative volume elements of composites and applications, International Journal of Solids and Structures 40 (8) (2003) 1907–1921.
98. V.-D. Nguyen, E. Béchet, C. Geuzaine, L. Noels, Imposing periodic boundary condition on arbitrary meshes by polynomial interpolation, Computational Materials Science 55 (2012) 390–406.
99. J. Tyrus, M. Gosz, E. DeSantiago, A local finite element implementation for imposing periodic boundary conditions on composite micromechanical models, International Journal of Solids and Structures 44 (9) (2007) 2972–2989.
100. Z. Yuan, J. Fish, Toward realization of computational homogenization in practice, International Journal for Numerical Methods in Engineering 73 (3) (2008) 361–380.
101. K. Schneider, B. Klusemann, S. Bargmann, Fully periodic RVEs for technological relevant composites: not worth the effort!, Journal of Mechanics of Materials and Structures 12 (4) (2017) 471–484.
102. G. A. Kassem, Micromechanical Material Models for Polymer Composites through Advanced Numerical Simulation Techniques, Ph.D. thesis, Aachen University in Germany (2009).
103. C. M. Zener, S. Siegel, Elasticity and anelasticity of metals., The Journal of Physical and Colloid Chemistry 53 (9) (1949) 1468–1468.
104. T. Kanit, F. N'Guyen, S. Forest, D. Jeulin, M. Reed, S. Singleton, Apparent and effective physical properties of heterogeneous materials: representativity of samples of two materials from food industry, Computer Methods in Applied Mechanics and Engineering 195 (33) (2006) 3960–3982.
105. D. H. Chung, W. R. Buessem, The elastic anisotropy of crystals, Journal of Applied Physics 38 (5) (1967) 2010–2012.
106. S. I. Ranganathan, M. Ostoja-Starzewski, Universal elastic anisotropy index, Physical Review Letters 101 (5).
107. T. V. Vernitskaya, O. N. Efimov, Polypyrrole: a conducting polymer; its synthesis, properties and applications, Russian Chemical Reviews 66 (5) (1997) 443.
108. M. F. Ashby, R. F. M. Medalist, The mechanical properties of cellular solids, Metallurgical Transactions A 14 (9) (1983) 1755–1769.
109. T. L. Anderson, Fracture Mechanics: Fundamentals and Applications, 3rd Edition, CRC Press, 2005.
110. M. Kuna, Finite Elements in Fracture Mechanics: Theory - Numerics - Applications, Springer Science & Business Media, 2013.
111. A. A. Griffith, The phenomena of rupture and flow in solids, Philosophical Transactions of the Royal Society A: Mathematical, Physical and Engineering Sciences 221 (582-593) (1921) 163–198.
112. G. R. Irwin, Onset of fast crack propagation in high strength steel and aluminum alloys, Tech. rep., Naval research lab Washington DC.
113. B. Cotterell, J. K. Reddel, The essential work of plane stress ductile fracture, International Journal of Fracture 13 (3) (1977) 267–277.
114. A. Atkins, Y. Mai, Fracture strains in sheet metalforming and specific essential work of fracture, Engineering Fracture Mechanics 27 (3) (1987) 291–297.

115. R. O. Ritchie, The conflicts between strength and toughness, Nature Materials 10 (11) (2011) 817–822.
116. L. de Arcangelis, S. Redner, H. Herrmann, A random fuse model for breaking processes, Journal de Physique Lettres 46 (13) (1985) 585–590.
117. B. Kahng, G. G. Batrouni, S. Redner, L. de Arcangelis, H. J. Herrmann, Electrical breakdown in a fuse network with random, continuously distributed breaking strengths, Physical Review B 37 (13) (1988) 7625–7637.
118. P. M. Duxbury, P. L. Leath, P. D. Beale, Breakdown properties of quenched random systems: The random-fuse network, Physical Review B 36 (1) (1987) 367–380.
119. C. Koenke, R. Harte, W. Krätzig, O. Rosenstein, On adaptive remeshing techniques for crack simulation problems, Engineering Computations 15 (1) (1998) 74–88.
120. T. Belytschko, T. Black, Elastic crack growth in finite elements with minimal remeshing, International Journal for Numerical Methods in Engineering 45 (5) (1999) 601–620.
121. N. Moës, J. Dolbow, T. Belytschko, A finite element method for crack growth without remeshing, International journal for numerical methods in engineering 46 (1) (1999) 131–150.
122. D. Dugdale, Yielding of steel sheets containing slits, Journal of the Mechanics and Physics of Solids 8 (2) (1960) 100–104.
123. G. Barenblatt, The mathematical theory of equilibrium cracks in brittle fracture, in: Advances in Applied Mechanics, Elsevier, 1962, pp. 55–129.
124. I. Schmidt, N. Fleck, Ductile fracture of two-dimensional cellular structures-dedicated to Prof. Dr.-Ing. D. Gross on the occasion of his 60th birthday, International Journal of Fracture III (4) (2001) 327–342.
125. P. Onck, R. van Merkerk, J. D. Hosson, I. Schmidt, Fracture of metal foams: In-situ testing and numerical modeling, Advanced Engineering Materials 6 (6) (2004) 429–431.
126. K. Mangipudi, P. Onck, Multiscale modelling of damage and failure in two-dimensional metallic foams, Journal of the Mechanics and Physics of Solids 59 (7) (2011) 1437–1461.
127. K. Mangipudi, P. Onck, Notch sensitivity of ductile metallic foams: A computational study, Acta Materialia 59 (19) (2011) 7356–7367.
128. H. Tankasala, V. Deshpande, N. Fleck, Tensile response of elastoplastic lattices at finite strain, Journal of the Mechanics and Physics of Solids 109 (2017) 307–330.
129. C. Zhang, L. Tang, B. Yang, L. Zhang, X. Huang, D. Fang, Meso-mechanical study of collapse and fracture behaviors of closed-cell metallic foams, Computational Materials Science 79 (2013) 45–51.
130. C. González, J. LLorca, Multiscale modeling of fracture in fiber-reinforced composites, Acta Materialia 54 (16) (2006) 4171–4181.
131. L. P. Canal, C. González, J. Segurado, J. LLorca, Intraply fracture of fiber-reinforced composites: Microscopic mechanisms and modeling, Composites Science and Technology 72 (11) (2012) 1223–1232.
132. B. Bilby, L. Gardner, A. Stroh, Continuous distributions of dislocations and the theory of plasticity, in: Proceedings of the 9th international congress of applied mechanics, Vol. 8, University de Bruxelles Brussels, 1957, pp. 35–44.
133. E. Kröner, Allgemeine Kontinuumstheorie der Versetzungen und Eigenspannungen, Archive for Rational Mechanics and Analysis 4 (1959) 273–334.
134. E. Lee, D. Liu, Finite-strain elastic-plastic theory with application to plane-wave analysis, Journal of Applied Physics 38 (1) (1967) 19–27.
135. E. H. Lee, Elastoplastic deformation at finite strains, ASME Journal of Applied Mechanics 36 (1969) 1–6.
136. L. Anand, M. E. Gurtin, A theory of amorphous solids undergoing large deformations, with application to polymeric glasses, International Journal of Solids and Structures 40 (6) (2003) 1465–1487.
137. B. Gearing, L. Anand, On modeling the deformation and fracture response of glassy polymers due to shear-yielding and crazing, International Journal of Solids and Structures 41 (11) (2004) 3125 – 3150.
138. J. Torres, P. Frontini, Mechanics of polycarbonate in biaxial impact loading, International Journal of Solids and Structures 85-86 (2016) 125 – 133.
139. P. I. Kattan, G. Z. Voyiadjis, Damage Mechanics, Springer Berlin Heidelberg, Berlin, Heidelberg, 2002, pp. 1–35.

140. P. Ladeveze, J. Lemaitre, Damage effective stress in quasi-unilateral conditions, IUTAM Congress Proceedings, Lyngby (Denmark) 25.
141. J. Lemaitre, A Course on Damage Mechanics, Springer-Verlag, Berlin, 1996.
142. C. Soyarslan, H. Richter, S. Bargmann, Variants of Lemaitre's damage model and their use in formability prediction of metallic materials, Mechanics of Materials 92 (2016) 58 – 79.
143. C. Soyarslan, A. Tekkaya, U. Akyuz, Application of continuum damage mechanics in discontinuous crack formation: Forward extrusion chevron predictions, ZAMM 88 (6) (2008) 436–453.
144. C. Soyarslan, A. E. Tekkaya, Prevention of internal cracks in forward extrusion by means of counter pressure: A numerical treatise, steel research international 80 (9) (2009) 671–679.
145. B. Elsner, S. Müller, S. Bargmann, J. Weissmüller, Surface excess elasticity of gold: Ab initio coefficients and impact on the effective elastic response of nanowires, Acta Materialia 124 (2017) 468–477.
146. C. A. Volkert, E. T. Lilleodden, Size effects in the deformation of sub-micron Au columns, Philosophical Magazine 86 (33-35) (2006) 5567–5579.
147. L. Gibson, M. Ashby, Cellular Solids: Structure and Properties, Cambridge Solid State Science Series, Cambridge University Press, 1999.
148. D. Carolan, H. Chong, A. Ivankovic, A. Kinloch, A. Taylor, Co-continuous polymer systems: A numerical investigation, Computational Materials Science 98 (2015) 24–33.
149. D. E. Spahr, K. Friedrich, J. M. Schultz, R. S. Bailey, Microstructure and fracture behaviour of short and long fibre-reinforced polypropylene composites, Journal of Materials Science 25 (10) (1990) 4427–4439.
150. A. J. Kinloch, A. C. Taylor, The mechanical properties and fracture behaviour of epoxy-inorganic micro- and nano-composites, Journal of Materials Science 41 (11) (2006) 3271–3297.
151. A. Coldea, M. V. Swain, N. Thiel, Mechanical properties of polymer-infiltrated-ceramic-network materials, Dental Materials 29 (4) (2013) 419–426.
152. L. Wegner, L. Gibson, The fracture toughness behaviour of interpenetrating phase composites, International Journal of Mechanical Sciences 43 (8) (2001) 1771–1791.
153. R. Pippan, S. Wurster, D. Kiener, Fracture mechanics of micro samples: Fundamental considerations, Materials & Design 159 (2018) 252–267.
154. N. Travitzky, A. Shlayen, Microstructure and mechanical properties of Al_2O_3/Cu–O composites fabricated by pressureless infiltration technique, Materials Science and Engineering: A 244 (2) (1998) 154–160.
155. Y. Bar-Cohen, Electroactive Polymer (EAP) Actuators as Artificial Muscles: Reality, Potential, and Challenges, 2nd Edition, Vol. 136, SPIE Publications, 2004, Ch. 1, pp. 4–53.
156. S. Nemat-Nasser, J. Li, Electromechanical response of ionic polymer-metal composites, Journal of Applied Physics 87 (7) (2000) 3321–3331.
157. T. Otero, J. Sansiñena, Artificial muscles based on conducting polymers, Bioelectrochemistry and Bioenergetics 38 (2) (1995) 411–414.
158. Y. Osada, M. Hasebe, Electrically activated mechanochemical devices using polyelectrolyte gels, Chemistry Letters 14 (9) (1985) 1285–1288.
159. Q. Pei, O. Inganläs, Conjugated polymers and the bending cantilever method: Electrical muscles and smart devices, Advanced Materials 4 (4) (1992) 277–278.
160. M. Gandhi, P. Murray, G. Spinks, G. Wallace, Mechanism of electromechanical actuation in polypyrrole, Synthetic Metals 73 (3) (1995) 247–256.
161. P. Chiarelli, A. D. Santa, D. de Rossi, A. Mazzoldi, Actuation properties of electrochemically driven polypyrrole free-standing films, Journal of Intelligent Material Systems and Structures 6 (1) (1995) 32–37.
162. E. Smela, Conjugated polymer actuators for biomedical applications, Advanced Materials 15 (6) (2003) 481–494.
163. Y. Bar-Cohen, V. Cardoso, C. Ribeiro, S. Lanceros-Méndez, Electroactive polymers as actuators, in: Advanced Piezoelectric Materials, Elsevier, 2017, pp. 319–352.
164. B. Yan, Y. Wu, L. Guo, Recent advances on polypyrrole electroactuators, Polymers 9 (12) (2017) 446.
165. K. Wang, C. Stenner, J. Weissmüller, A nanoporous gold-polypyrrole hybrid nanomaterial for actuation, Sensors and Actuators B: Chemical 248 (2017) 622–629.

166. E. Detsi, P. Onck, J. T. De Hosson, Metallic muscles at work: High rate actuation in nanoporous gold/polyaniline composites, ACS Nano 7 (5) (2013) 4299–4306.
167. S. Saane, K. Mangipudi, K. Loos, J. D. Hosson, P. Onck, Multiscale modeling of charge-induced deformation of nanoporous gold structures, Journal of the Mechanics and Physics of Solids 66 (2014) 1–15.
168. D. Kramer, R. N. Viswanath, J. Weissmüller, Surface-stress induced macroscopic bending of nanoporous gold cantilevers, Nano Letters 4 (5) (2004) 793–796.
169. E. Detsi, Z. G. Chen, W. P. Vellinga, P. R. Onck, J. T. M. D. Hosson, Reversible strain by physisorption in nanoporous gold, Applied Physics Letters 99 (8) (2011) 083104.
170. B. Roschning, J. Weissmüller, Stress-charge coupling coefficient for thin-film polypyrrole actuators - Investigation of capacitive ion exchange in the oxidized state, Electrochimica Acta 318 (2019) 504–512.
171. D. Pugal, K. J. Kim, A. Aabloo, An explicit physics-based model of ionic polymer-metal composite actuators, Journal of Applied Physics 110 (8) (2011) 084904.
172. P. Nardinocchi, M. Pezzulla, L. Placidi, Thermodynamically based multiphysic modeling of ionic polymer metal composites, Journal of Intelligent Material Systems and Structures 22 (16) (2011) 1887–1897.
173. C. G. Zoski, Handbook of Electrochemistry, Elsevier Science, 2006.
174. D. T. Hallinan, N. P. Balsara, Polymer electrolytes, Annual Review of Materials Research 43 (1) (2013) 503–525.
175. B. A. Schlake, Mathematical models for particle transport: Crowded motion, Ph.D. thesis, Westfälische Wilhelms-Universität Münster (2011).
176. J. Wilmers, S. Bargmann, Functionalisation of metal–polymer-nanocomposites: Chemoelectromechanical coupling and charge carrier transport, Extreme Mechanics Letters 21 (2018) 57–64.
177. J. Foroughi, S. R. Ghorbani, G. Peleckis, G. M. Spinks, G. G. Wallace, X. Wang, S. Dou, The mechanical and the electrical properties of conducting polypyrrole fibers, Journal of Applied Physics 107 (10) (2010) 103712.
178. J. López Cascales, T. Otero, Molecular dynamic simulation of the hydration and diffusion of chloride ions from bulk water to polypyrrole matrix, The Journal of Chemical Physics 120 (4) (2004) 1951–1957.
179. H. D. B. Jenkins, K. P. Thakur, Reappraisal of thermochemical radii for complex ions, Journal of Chemical Education 56 (9) (1979) 576.
180. Y. Liu, J. Lynch, The development of chloride ion selective polypyrrole thin film on a layer-by-layer carbon nanotube working electrode, in: Nondestructive Characterization for Composite Materials, Aerospace Engineering, Civil Infrastructure, and Homeland Security 2011, SPIE, 2011.